# HIGH PERFORMANCE III-NITRIDE ULTRAVIOLET AVALANCHE PHOTODETECTORS

A Ph.D Dissertation Thesis
Presented to
The Academic Faculty

by

Hoon Jeong

In Partial Fulfillment
of the Requirements for the Degree
Doctor of Philosophy in the
School of Electrical and Computer Engineering

Georgia Institute of Technology
December 2021

**COPYRIGHT © 2021 BY HOON JEONG**

# HIGH PERFORMANCE III-NITRIDE ULTRAVIOLET AVALANCHE PHOTODETECTORS

Approved by:

Dr. Russell D. Dupuis, Advisor
School of Electrical and Computer Engineering
*Georgia Institute of Technology*

Dr. Thomas K. Gaylord
School of Electrical and Computer Engineering
*Georgia Institute of Technology*

Dr. Nepomuk A. Otte
School of Physics
*Georgia Institute of Technology*

Dr. Oliver Brand
School of Electrical and Computer Engineering
*Georgia Institute of Technology*

Dr. Ali Adibi
School of Electrical and Computer Engineering
*Georgia Institute of Technology*

Date Approved: November 4th, 2021

# ACKNOWLEDGEMENTS

I would like to express my gratitude and appreciation to all those who have helped me along the way in making this work and dissertation possible. First, I would like to thank my advisor, Dr. Russell D. Dupuis, for all his guidance and for providing me with valuable opportunity to participate in various projects and to study in the various fields of optoelectronics. I am very proud of being one of his students and I am honored to work in his Advanced Materials and Devices Group (AMDG) at Georgia Institute of Technology.

I would like to thank to my committee members, Dr. Nepomuk A. Otte, Dr. Ali Adibi, Dr. Thomas K. Gaylord, and Dr. Oliver Brand for the valuable comments and suggestions. Their insights and guidance were invaluable, and I have learned much from them. It is a great honor to have their names on my dissertation.

I am also thankful to my past and current colleagues in AMDG: Dr. Mi-Hee Ji, Dr. Theeradetch Detchprohm, Dr. Franke Mehnke, Dr. Kevin Liu, Marzieh Bakhtiary Noodeh for their help and cooperation in all my research. I am also grateful to past and current members of Dr. Shen's research group: James Wang, Dr. Chuan-Wei Tsou, Dr. Minkyu Cho, and Zhiyu Xu. I am also grateful to Eliza A Gazda in Dr. Otte's research group for her support in the single-photon detection project. I would especially like to thank to Dr. Theeradetch Detchprohm and Dr. Mi-Hee Ji for being great mentors for many years of personal, professional, and technical guidance.

Finally, I would like to thank my parents for their unconditional love and support. Especially, I am thankful to my younger brother Il Jeong, who has always been my friend. I

am grateful to my fiancée Sally Park, who has always encouraged me with patience and unconditional support.

# TABLE OF CONTENTS

**ACKNOWLEDGEMENTS** **iii**

**LIST OF TABLES** **vii**

**LIST OF FIGURES** **viii**

**LIST OF SYMBOLS WITH NAMES AND UNITS** **xv**

**LIST OF ACRONYMS AND ABBREVIATIONS** **xvi**

**CHAPTER 1. Introduction** **1**
**1.1 III-nitride material properties** **3**
**1.2 Metalorganic Chemical Vapor Deposition** **5**
**1.3 Avalanche photodiodes and single-photon detection** **7**
**1.4 Previous research** **10**
1.4.1 Photomultiplier tubes and silicon avalanche photodiodes 10
1.4.2 SiC APDs and Geiger-mode operation 11
1.4.3 III-N APDs and Geiger-mode operation 12

**CHAPTER 2. Design, growth, fabrication and characterization of deep-ultraviolet aluminum gallium nitride avalanche photodiodes** **15**
**2.1 Introduction** **15**
**2.2 Material characterization** **15**
2.2.1 X-ray diffraction 15
2.2.2 Absorbance spectra and bandgap energy 20
**2.3 Device characterization** **21**
2.3.1 Current Voltage (I-V) characteristics and gain calculation 22
2.3.2 Spectral responsivity or photoresponse measurements 23
**2.4 Design of deep UV (DUV) AlGaN *p-i-n* APDs** **26**
2.4.1 Excess noise, ionization coefficient and front/back illumination 27
2.4.2 Aluminum nitride (AlN) template vs. AlN substrate 30
2.4.3 Breakdown electric field of $Al_xGa_{1-x}N$ 31
2.4.4 Absorption coefficient and thickness of absorption/multiplication layer (i-layer)33
2.4.5 Thickness of p-type and n-type layers 34
2.4.6 Passivation layer material and thickness 35
**2.5 Growth of deep-UV AlGaN *p-i-n* APDs** **36**
2.5.1 Calibration of AlGaN layers 36
**2.6 Fabrication of deep-UV AlGaN *p-i-n* APDs** **44**
**2.7 Characterization of deep-UV AlGaN *p-i-n* APDs** **49**
**2.8 Summary** **55**

**CHAPTER 3. Low-temperature Geiger-mode measurements of gallium nitride avalanche photodiodes** **56**
**3.1 Introduction** **56**

**3.2 Sample structure** **56**
**3.3 Theory of photon counting** **59**
3.3.1 Quenching circuit 59
3.3.2 Mathematics of single-photon detection 64
3.3.3 Validity of the Δt method 69
**3.4 Geiger-mode measurement system** **70**
3.4.1 Measurement circuit system 71
3.4.2 Low-temperature control system 77
3.4.3 Ultraviolet illumination system 81
3.4.4 Software for dark count rate and photo detection efficiency calculation 84
**3.5 Results and discussion** **86**
**3.6 Summary** **93**

**CHAPTER 4. Research summary** **94**

**CHAPTER 5. Future works** **97**

# LIST OF TABLES

Table 1 Calibrated AlGaN APD structure growth parameters. ............................................42

# LIST OF FIGURES

Figure 1-1 The bandgap energies of III-nitrides, and other conventional semiconductors versus their lattice constants. (1)....................2

Figure 1-2 The unit cell of the wurtzite structure for III-nitride semiconductors. Large yellow spheres are Ga, In, Al sites, and small grey spheres are nitrogen sites. (3)................4

Figure 1-3 The schematic diagram of a MOCVD system and the process............................6

Figure 1-4 Schematic diagram of the impact-ionization process is depicted. .........................9

Figure 1-5 Three modes of operation a) photodiode mode, b) proportional mode, and c) Geiger mode...............................................10

Figure 2-1 A schematic diagram showing all the axes of rotation (46). X denotes the X-ray source and D denotes the detector. ...............................16

Figure 2-2 The incident ($\boldsymbol{ko}$) and diffracted ($\boldsymbol{kh}$) wavevector forms the scattering vector $Q$, which points to the reciprocal lattice, and lies on the surface of the Ewald sphere. The directions are depicted for different types of scans ($\boldsymbol{\omega}, \boldsymbol{2\theta}$ and $\boldsymbol{\omega}$-$\boldsymbol{2\theta}$) in reciprocal space. . 17

Figure 2-3 a) Absorbance spectra of $Al_{0.408}Ga_{0.592}N$, $Al_{0.602}Ga_{0.398}N$, and $Al_{0.74}Ga_{0.26}N$ are shown. The bandgap energy can be obtained by drawing two tangent line and calculating the intersection point. b) The bandgap energy vs AlN mole fraction $x$ is plotted. The bandgap energies of GaN and AlN were obtained by Tauc method as well.......................................21

Figure 2-4 A schematic diagram of the spectral responsivity measurement setup using a variable-wavelength light source. ...............................24

Figure 2-5 The calibreated photoresponse measurement using a DUV LED with 250nm emission wavelength.......................................25

Figure 2-6 Schematic design of the deep UV $Al_xGa_{1-x}N$ APD with $\boldsymbol{x = 0.6}$......................26

Figure 2-7 The flow of the design, and some of the aspects require feedbacks from growth or fabrication step. ....................................................................................................27

Figure 2-8 A plot of the excess noise factor versus the multiplication factor (15)...............29

Figure 2-9 a) The ionization coefficient for $Al_xGa_{1-x}N$ material. Notice that the electron ionization coefficient gets bigger than the hole ionization coefficient once $\boldsymbol{x}$ reaches 0.6. b) The ionization coefficients of the carriers for the $Al_{0.6}Ga_{0.4}N$ material is shown. Notice that the ratio of electron ($\boldsymbol{\beta}$) to hole ($\boldsymbol{\alpha}$) ionization coefficient $\boldsymbol{k = \beta/\alpha}$ is always less than 1 for all the electric field.......................................................................................................30

Figure 2-10 A plot of the breakdown electric field versus the AlN mole fraction x. The black solid line represents the equation (20), with the breakdown electric field value provided in the paper (61). The red dot represents the breakdown electric field at $\boldsymbol{x = 0.57}$, and red dashed line is an extrapolated line using equation (20) .......................................................33

Figure 2-11 The interpolated absorption coefficient of the $Al_{0.6}Ga_{0.4}N$ from Muth's article (63). The absorption wavelength is chosen slightly above the cut-off wavelength of absorption, which is 244nm. ................................................................................34

Figure 2-12 The thicknesses of 1st to 8th layer are shown....................................................35

Figure 2-13 The schematic diagram of each layer in the $Al_xGa_{1-x}N$ APD structure showing target growth temperatures and target AlN mole fractions..................................................37

Figure 2-14 The reciprocal space mapping (RSM) around the (105) reflection of the AlGaN APD structure grown on a) the Type-A AlN template, b) the Type-B AlN template, and c) the AlN bulk substrate. Notice that the peaks in the XRD RSM of the AlN bulk substrate are the narrowest. ......................................................................................................39

Figure 2-15 Electrical data on $Al_xGa_{1-x}N$:Si *n*-type films: a) Free-electron concentration, b) electron mobility, c) resistivity are plotted versus Si/III ratio, and electrical data on GaN:Mg *p*-type films: d) free-hole concentration, e) hole mobility, f) resistivity are plotted versus Mg/III ratio. From the free-electron concentration vs. Si/III graph, it is possible to interpolate the Si/III ratio for the target doping. With the Si/III ratio, it is also possible to estimate the electron mobility and the resistivity of the sample. Same technique can be applied to the free-hole concentration vs. Mg/III graph. .....................................................41

Figure 2-16 The *I-V* curves of the transmission line measurement (TLM) patterns of *p*+-GaN samples grown with various $Cp_2Mg$ flow rates. In the above graph, the sample with a $Cp_2Mg$ flow rate of $\mathbf{1.43 \times 10 - 6 mol/min}$ has the ohmic contact. ...............................42

Figure 2-17 The surface morphology measured by 5 µm x 5 µm atomic-force microscopy (AFM) scans of the Type-A, Type-B AlN templates and the AlN bulk substrate before and after the AlGaN APD growth are shown. ...............................44

Figure 2-18 Schematic diagram of the cross-sectional structure of the device processing steps used to fabricate AlGaN *p-i-n* APDs. ...............................45

Figure 2-19 Table of photographs of the etched $Al_xGa_{1-x}N$ $x = 0.6$ surfaces with the ICP coil power varying from 300W to 600W, and the platen power varying from 10W to 50W is shown. If the platen power is too low for a certain coil power, pits and hillocks are formed on the surface. ...............................46

Figure 2-20 The ADS mask file for each layer is shown with different circular mesa diameters ranging from 20 to 100µm ...............................47

Figure 2-21 Microscope image of a completed AlGaN APD structure grown on a AlN bulk substrate. The correspondence of each region with an APD device schematic diagram is shown. ...............................48

Figure 2-22 The dark current density vs. reverse bias of AlGaN APDs fabricated on different substrates. The circular diameters of the measured APD devices are 20µm. The black line is the dark current density from an APD on Type-A AlN template, the red line is from an APD on Type-B AlN template, and the yellow line is from an APD on the AlN bulk substrate. Notice that the dark current density from the APD on the AlN bulk substrate is the lowest. ...............................50

Figure 2-23 Dark and photocurrent density of the 20 µm diameter AlGaN APD fabricated on the AlN bulk substrate are shown, using 250 nm UV light from a Xe lamp and the monochromator. The optical gain is also calculated. ...............................51

Figure 2-24 Average photoresponse at 250 nm, and zero bias for the 100 µm dia. AlGaN APD devices from the Type-A, Type-B AlN templates and the AlN bulk substrate were measured. ...............................53

Figure 2-25 The temperature coefficients of the reverse-bias breakdown voltage of the AlGaN APDs from different substrates are shown with error bars. The devices have a circular dimension of 20 μm diameter. ........ 54

Figure 3-1 a) Schematic diagram of the cross-sectional structure of GaN *p-i-n* APD grown on bulk GaN substrates. b) Microscopic images of a fabricated GaN APD sample (Credit to Dr. Mi-Hee Ji.) ........ 57

Figure 3-2 The reverse bias I-V characteristics of the GaN p-i-n APD array devices with a mesa size of 75×75 μm2 under dark condition and UV illumination with a peak wavelength of $\boldsymbol{\lambda = 340nm}$ ........ 58

Figure 3-3 a) passive quenching circuit, b) active quenching circuit (77), c) gated quenching circuit ........ 60

Figure 3-4 a) The rectangular pulse signal applied to the APD, and the avalanche signal captured with a measurement unit. Notice that there is delay $\Delta t_i$ between onset of the pulse signal to the onset of the avalanche signal. b) When the pulse + DC voltage is below breakdown there is no avalanche event. c) When the pulse + DC voltage is above breakdown, some time $\boldsymbol{\Delta t}$ after rising edge (red arrow in b) avalanche event will occur. The spike at the rising and falling edge (blue arrow in b) is due to inherent capacitor in the oscilloscope. ........ 62

Figure 3-5 a) Histogram of number of avalanche events occurred for certain $\Delta t_i$. The slope can be fitted with the function proportional to exp(-2$\Delta t \cdot R$) to get the count rate $R$. b) In the real device example, the count rate is easily obtained by fitting with a semi-logarithmic scale. ........ 63

Figure 3-6 Schematic diagram of the application of Poisson distribution, which is called interval between successive events. ........ 67

Figure 3-7 Schematic diagram comparison of two methods of count rate measurement a) using a frequency counter, b) using the $\boldsymbol{\Delta t}$ method c) and the measurement results, which shows that the data are similar to each other within the error. ........ 70

Figure 3-8 Schematic diagram of a Geiger-mode measurement setup, consisting of a UV-illumination system (shaded in violet), a measurement circuit (shaded in green), and a low-

temperature control system (shaded in blue). All the equipment in the hardware systems are connected to the computer, controlled by C++ program. ....................................................71

Figure 3-9 a) Schematic circuit diagram consisting of gated quenching circuit, two op-amps (noninverting and transimpedance) and measurement unit. b) photograph of PCB board of the quenching circuit, with GaN APD connected to the PCB board with wire-bonding. c) Oscilloscope graph showing before and after the avalanche, which avalanche signal is clearly observed and thus the time delay $\Delta t$ between onset of pulse to onset of avalanche signal can be measured ..........................................................................................72

Figure 3-10 a) The oscillation added in the output node of the transimpedance amplifier is visualized in the DRS4 oscilloscope. b) the oscillation is removed by connecting a compensating capacitor $C_F$ in parallel with the feedback resistor ........................................74

Figure 3-11 a) the circuit diagram of the APD with the transimpedance amplifier. The APD is modeled into a resistance $R_d$ and capacitance $C_d$ connected in parallel. The compensating capacitor $C_F$ is connected in parallel with feedback resistor $R_F$. b) Modeling the APD and transimpedance amplifier circuit into a feedback system with feedback factor $\beta$ and an open loop gain $A$ of the op amp. The sinusoidal signal at the inverting (-) input shows that the phase difference is -180° (opposite phase) compared with the signal at the noninverting (+) input. This makes positive feedback and the input signal gets larger and larger, thus creating the oscillation. c) Simulation of a gain-frequency plot of the open loop A and the feedback factor $\beta$. The compensating capacitance $C_F$ can be obtained by looking at the plot where the zero frequency of the feedback gain $\beta$ crosses the open loop gain $A$ ...................................75

Figure 3-12 a) Schematic diagram of a three-stage thermoelectric cooler (TEC) module, aluminum cage, heatsink with circulating cooling water + ethylene glycol mixture. b) photograph of the APD attached directly on the TEC module. The APD is connected to the PCB via wire bonding..........................................................................................................77

Figure 3-13 a) A microscope image of the GaN APD surface when the surface temperature is below 0°C and exposed to an outside air. Notice there is moisture condensation on the surface of the APD. b) If the nitrogen is filled instead of the air, there is no condensation or icing even at -40°C. c) Solidworks design of the aluminum cage with the lid, nitrogen inlet and outlet, electrical ports, and the PCB board and the APD. d) A photograph image of complete aluminum cage with foam enclosing the outside surface......................................78

Figure 3-14 a) photograph of an infrared thermometer monitoring the surface of the 3-stage TEC module, and the GaN APD is attached to the surface of the TEC module. b) schematic diagram of a PID controller, which consists of a microcontroller, the IR thermometer, the

TEC module, an *n*-MOSFET, and a DC supply. The IR thermometer and the TEC module is inside the aluminum cage, filled with nitrogen gas. ............................................................ 79

Figure 3-15 Schematic diagram of a PID controller algorithm, including a proportional, an integral, and a differential term. In the real system, the differential term is not required since there is no sudden change of the temperature. ..................................................................... 80

Figure 3-16 A graph of temperature vs. time. The temperature is set to 0 to -45°C, in decreasing steps of -5°C. Notice that the precise control of the temperature of the surface of the TEC module is possible. ........................................................................................ 81

Figure 3-17 A schematic diagram of fiber-aluminum lid complex structure a) before assembly and b) after the assembly. The fiber goes through the 2$^{nd}$ OHP film, which moves freely between two fixed OHP films with rectangular holes. Then the fiber is connected to the x-y-z stage. In this configuration, the nitrogen gas is trapped inside the cage with OHP films, and the fiber position can be adjusted. ........................................................................ 83

Figure 3-18 The flow of algorithm for calculating the dark count rate and the photon detection efficiency is shown. The algorithm starts with setting the TEC module temperature, getting the pulse signal, increasing DC bias so that the total voltage is above the breakdown voltage of the GaN APD, deactivating/activating UV LED and Si photon counter (for dark count rate/photon count rate), getting the avalanche signal and calculating the time difference, and create the histogram. From the histogram the dark/photon count rate is calculated by measuring the slope, and the photon detection efficiency is obtained. ........ 86

Figure 3-19 Measured breakdown voltage as a function of temperature for the range from -45 to 20°C. The breakdown voltage is measured as the total DC + pulse voltage which gives the same probability of avalanching ($N_{avalanche}/N_{total}$). The temperature coefficient obtained is 0.0159 + 0.0034 V/K ........................................................................................... 88

Figure 3-20 The DCR as a function of excess bias at different temperature set points. ........ 89

Figure 3-21 a) The DCR as a function of reciprocal of the Boltzmann constant times the temperature at different excess bias voltages. b) The activation energy is obtained by fitting an Arrhenius equation. ........................................................................................... 91

Figure 3-22 The PDE of the GaN APD measured as a function of excess bias at different temperature set points. Notice that the error bars are so wide that other PDE curves are included in the error bars. ........................................................................................92

## LIST OF SYMBOLS WITH NAMES AND UNITS

| Quantity | Unit | Symbol |
|---|---|---|
| Length | Meter | m |
| | Angstrom | Å |
| Mass | Kilogram | Kg |
| Time | Second | s |
| | Minute | min |
| Frequency | Hertz | Hz |
| Electric current | Ampere | A |
| Voltage | Volt | V |
| Power | Watt | W |
| Energy | Electron Volt | eV |
| Thermodynamic temperature | Kelvin | K |
| | Celsius | °C |
| Amount of substance | Mole | mol |
| Pressure | Bar | bar |

# LIST OF ACRONYMS AND ABBREVIATIONS

| | |
|---|---|
| A | Open Loop Gain |
| AFM | Atomic Force Microscopy |
| AlGaN | Aluminum Gallium Nitride |
| AlN | Aluminum Nitride |
| APD | Avalanche Photodiode |
| BN | Boron Nitride |
| C | Capacitance |
| Cp2Mg | Cyclopentadienyl Magnesium |
| DCR | Dark Count Rate |
| DUV | Deep Ultraviolet |
| FWHM | Full Width Half Maximum |
| GaN | Gallium Nitride |
| HCP | Hexagonal Close-Packed |
| ICP | Inductively Coupled Plasma |
| InN | Indium Nitride |
| IR | Infrared |
| I-V | Current-Voltage |
| J-V | Current density-Voltage |
| LED | Light Emitting Diodes |
| MBE | Molecular-Beam Epitaxy |
| MOCVD | Metal-Organic Chemical Vapor Deposition |
| OHP film | Overhead Projector Film |
| Op Amp | Operational Amplifiers |
| PCB | Printed Circuit Board |
| PDE | Photon Detection Efficiency |
| PECVD | Plasma-Enhanced Chemical Vapor Deposition |
| PID | Proportional-Integral-Derivative |
| PMT | Photomultiplier Tubes |
| QKD | Quantum-Key Distribution |
| R | Resistance |
| RF | Radio Frequency |
| RIE | Reactive Ion Etching |
| RSM | Reciprocal Space Mapping |
| RTA | Rapid Thermal Annealing |
| SAM | Separate Absorption and Multiplication |
| Si | Silicon |
| SiC | Silicon Carbide |
| TEAl | Triethylaluminum |
| TEC | Thermoelectric Cooler |

| | |
|---|---|
| TEGa | Triethylgallium |
| TLM | Transmission Line Measurement |
| TMAl | Trimethylaluminum |
| TMGa | Trimethylgallium |
| TMIn | Trimethylindium |
| UHV | Ultra-High Vacuum |
| UV | Ultraviolet |
| VIS | Visible |
| XRD | X-ray Diffraction |
| $\beta$ | Feedback Factor |

# CHAPTER 1. INTRODUCTION

Gallium nitride (GaN), aluminum nitride (AlN), indium nitride (InN), boron nitride (BN) and their ternaries along with the quaternary AlInGaN, are called the III-nitride compound semiconductors, and are considered as the one of the most important semiconductor materials next to silicon. While III-N binary compound semiconductor materials have fixed value of direct bandgap energy (at a given temperature), III-N ternary and quaternary compound semiconductor materials can have a wide range of bandgap energies by adjusting the percentage of the group III elements. Thus, the III-N materials have bandgap energy ranging from as small as 0.7 eV (InN) to as large as 6.4 eV (BN). This energy range covers the spectral range from wavelengths in the infrared (IR, 1772 nm) to the ultraviolet (UV, 200 nm) (Figure 1-1). Such a wide range of spectrum coverage can be useful for optoelectronic applications such as light-emitting diodes (LEDs), lasers, photodetectors, and avalanche photodiodes (APDs). In addition to having a wide bandgap, many of the III-N materials also have a high breakdown electric field, a high electron drift velocity, and a high thermal conductivity, compared with other conventional semiconductor materials such as silicon, indium phosphide, and gallium arsenide. These properties make the III-nitride semiconductor materials favorable for electronic applications in extreme environments.

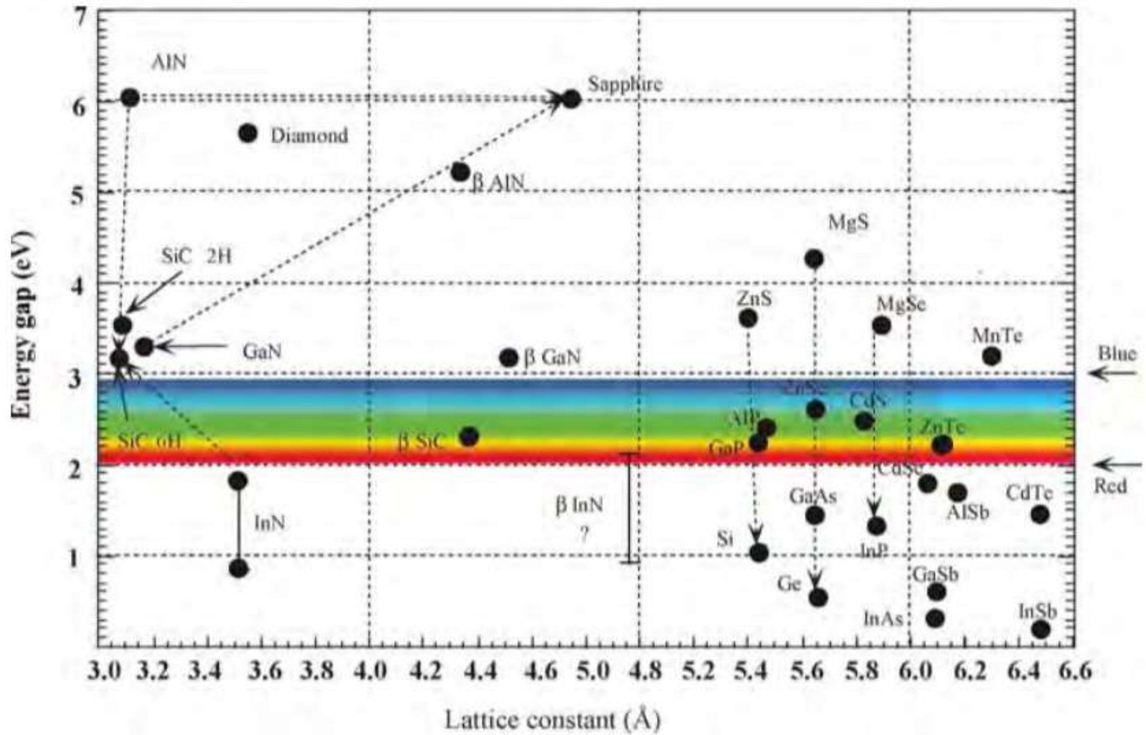


**Figure 1-1 The bandgap energies of III-nitrides, and other conventional semiconductors versus their lattice constants. [1]**

However, compared with mature conventional semiconductor technology such as silicon, the growth and fabrication of the III-nitride devices is challenging. The advantageous properties of these wide bandgap semiconductors have a trade-off with the electrical conductivity. Moreover, as the semiconductor bandgap energy increases, the obtainment of a low-resistance ohmic contact between the semiconductor and the metal becomes more difficult. Most important of all, if the structure consists of layers of III-nitride materials having much different lattice constants (i.e., a heterojunction), then there is a lattice mismatch at the heterojunction interface, which could induce undesirable stress, defects, and dislocations.

The objective of the proposed research is to develop III-nitride UV avalanche photodiodes capable of Geiger-mode operation at room temperature and above. The following

section is an introduction to the III-nitride material properties and the MOCVD growth system. Then, the development of photomultiplier tubes, silicon avalanche photodiodes, silicon carbide avalanche photodiodes and gallium nitride avalanche photodiode will be discussed, along with the Geiger-mode approach employed for these materials. Preliminary experiments done so far and the experimental results will be presented, and in the last section, the future work that needs to be done will be proposed.

## 1.1 III-nitride material properties

The wurtzite ((Zn,Fe)S) , zinc-blende (ZnS), and rock-salt (NaCl) crystal structures are the three main crystallographic forms of the III-nitride materials [1]. The zinc-blende structure can be stabilized by growing on the (001) crystal planes of a cubic crystal structure such as Si, MgO, and GaAs, thus it is metastable for heteroepitaxial thin films. There are many similarities between the wurtzite and zincblende structures. For both structures, the group III element is surrounded by four atoms of the group V elements, at the edges of the tetrahedron. However, the main difference between the wurtzite and zincblende structures is the stacking sequence of the crystal planes. The wurtzite structure has a stacking sequence of ABAB along [1] direction, and zinc-blende has stacking sequence of ABCABC. The rock-salt structure form of the III-Ns is only stable at very high pressures. Thus, among these three crystalline forms, the wurtzite structure is the most thermodynamically stable III-N material at room temperature and atmospheric pressure [2].

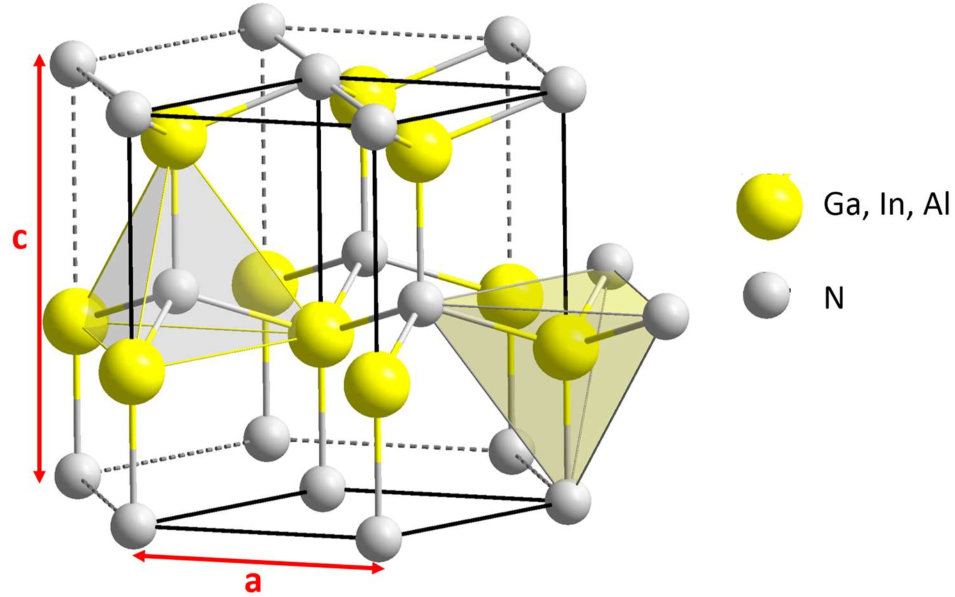


**Figure 1-2 The unit cell of the wurtzite structure for III-nitride semiconductors. Large yellow spheres are Ga, In, Al sites, and small grey spheres are nitrogen sites. [3]**

The hexagonal wurtzite structure of the III-nitride materials consists of two interpenetrating hexagonal close-packed (HCP) sublattices, which contain six atoms of each type. As shown in 2, there are two main lattice constants in the wurtzite structure, *a* and *c*. These lattice constants are perpendicular to each other, and the ideal wurtzite structure has *c/a* = 1.333. However, in the III-nitride materials system, *c/a* ratio is always lower than the ideal value due to the large electronegativity difference between Group V and Group III atoms. This large difference in electronegativity creates a distortion of the hexagonal unit cell and induces a dipole moment along the *c*-axis. This is called spontaneous polarization.

The wide and direct bandgap energy are the most important properties of the wurtzite III-nitride materials. By carefully engineering the mole percentage of each element in the III-N ternary and quaternary systems, the bandgap energy can be manipulated. For ternary

combinations, such as $Al_xGa_{1-x}N$ and $In_xGa_{1-x}N$, Vegard's law [4] can be used to determine bandgap from the mole percentage.

$$E_{g,A_x B_{1-x}N}(x) = x \cdot E_{g,A} + (1-x) \cdot E_{g,B} + bx(1-x) \quad (1)$$

where $E_{g,A_x B_{1-x}N}(x)$ is the bandgap energy of the ternary compound, $E_{g,A}$ and $E_{g,B}$ are the bandgap energies of the AN and BN compounds, respectively, $x$ is the percentage of the alloy system, and $b$ is the bandgap bowing parameter which is determined experimentally.

## 1.2 Metalorganic Chemical Vapor Deposition

There are two main growth methods for III-nitride semiconductor epitaxial materials. One is molecular-beam epitaxy (MBE) [5, 6] and the other is metalorganic chemical vapor deposition (MOCVD) [7, 8]. In the MBE process, the substrate is heated in ultra-high vacuum (UHV) around $10^{-9}$ Torr, and growth is done by directing elemental beams onto the substrate surface without using any carrier gases. Due to the UHV condition, the crystal grown by the MBE can achieve high purity, and MBE is able to grow some thermodynamically forbidden materials [9]. However, this requirement for expensive UHV equipment and high operating costs hinders MBE from being used on a large scale commercially, making it inappropriate for low-cost mass production.

The other growth method commonly used for III-N epitaxial growth is the MOCVD process. In MOCVD, several gas-phase materials are transported into the chamber and pyrolyzed in a hydrogen or nitrogen ambient. This pyrolysis creates reactant gases that reacts with each other and form a thin epitaxial layer on the substrate (see Figure 1-3). In the typical MOCVD process for III-N epitaxy, trimethylgallium (TMGa), triethylgallium (TEGa),

trimethylaluminum (TMAl) and trimethylindium (TMIn) are the major Group III metalorganic precursors transported to the chamber, and ammonia ($NH_3$) is the precursor for nitrogen. Silane gas ($SiH_4$) and cyclopentadienyl magnesium ($Cp_2Mg$) are the precursors for the *n*-type and *p*-type doping, respectively. The overall chemical reaction between the metalorganic reactant gas and nitrogen to form the III-nitride material is expressed by the equation below [10],

$$R_3M(g) + NH_3 \rightarrow MN(s) + 3RH(g) \tag{2}$$

where *R* is the organic group of either methyl or ethyl, M is the Group III metal, N is nitrogen, and H is hydrogen. The overall process occurring in MOCVD can be categorized into four major processes: gas input, pyrolysis, diffusion (through a boundary layer), and surface reactions. Several types of surface reactions may occur, which include adsorption, desorption, and the diffusion of adatoms.

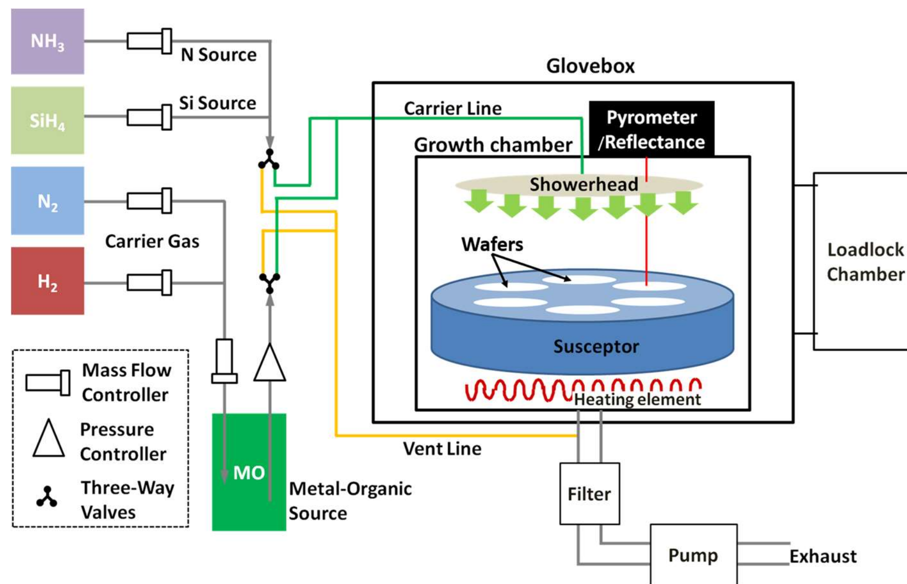


**Figure 1-3 The schematic diagram of a MOCVD system and the process.**

## 1.3 Avalanche photodiodes and single-photon detection

The UV light is the part of the electromagnetic spectrum where the wavelength ranges broadly from 10nm (near X-ray) to 400nm (near violet of the visible light). The UV light can be divided into three sub-bands according to how the photons interact with the earth's ozone layer in the atmosphere. The first sub-band is UVA, which has a wavelength range from 315nm to 400nm, and is not absorbed by the ozone layer thus most of it reaches the ground. The second sub-band UVB has a wavelength range from 280nm to 315nm, and it is mostly absorbed by the ozone layer. The last sub-band is the UVC with wavelength range from 100nm to 280nm, which is fully absorbed by the ozone layer. Since the UVC radiation does not reach the ground on earth, all the earth-based photosensors detecting this UV sub-band can be utilized without being disturbed by ambient radiation. The photodetectors which detect only UVC region are called solar-blind photodetectors.

Due to the work of pioneers such as Max Planck, Albert Einstein, Niels Bohr, Erwin Schrodinger, and Werner Heisenberg, and the advent of quantum mechanics, light which was considered a wave before was found to also exhibit a particle nature. The particle or quanta of light, or the corresponding electromagnetic wave, is called a photon. It is a massless Boson, without electrical charge, and has energy equivalent to the electromagnetic wave frequency multiplied by the Planck's constant. The energy of a single photon is insignificantly small compared with the intensity of the everyday light sources we observe. It is usually much lower than the minimum detectable level of typical optical sensor system.

To detect such a small energy, scientists and engineers have developed the technique called the photon counting [11-14]. With this technique, special optical sensor systems such as photomultiplier tubes or APDs with a suitable circuit system can count single photons. This photon-counting operation mode of the photodetector is called the Geiger mode. In this way, the minimum detectable level that those optical sensor systems inherently have can be avoided.

An APD is a semiconductor photodiode detector which exploits an avalanche breakdown effect called the impact-ionization process (Figure 1-4) [15]. In the impact-ionization process, a large reverse bias is applied across the APD, which increases the electric field in the multiplication region (typically, the *i*-layer, or depletion layer). Upon illumination of the device with light having a photon energy equivalent to, or larger than, the bandgap energy of the absorbing region of the APD device, an electron-hole pair can be created. The high electric field can accelerate the free carriers (electrons and holes) to the saturation drift velocity and the carriers can gain enough energy to overcome the ionization energy of the covalent bond. When the accelerated by the electric field to a high drift velocity, the carrier can collide with a covalent bond in the crystal lattice, and another electron-hole pair can be created. The free carriers from the secondary electron-hole pair can accelerate and collide with another covalent bond in the crystal lattice and the third electron-hole pair can be created, etc. It is a regenerative process, and the overall photocurrent is amplified. In theory, the impact ionization process creates a measurable photocurrent with a single photon.

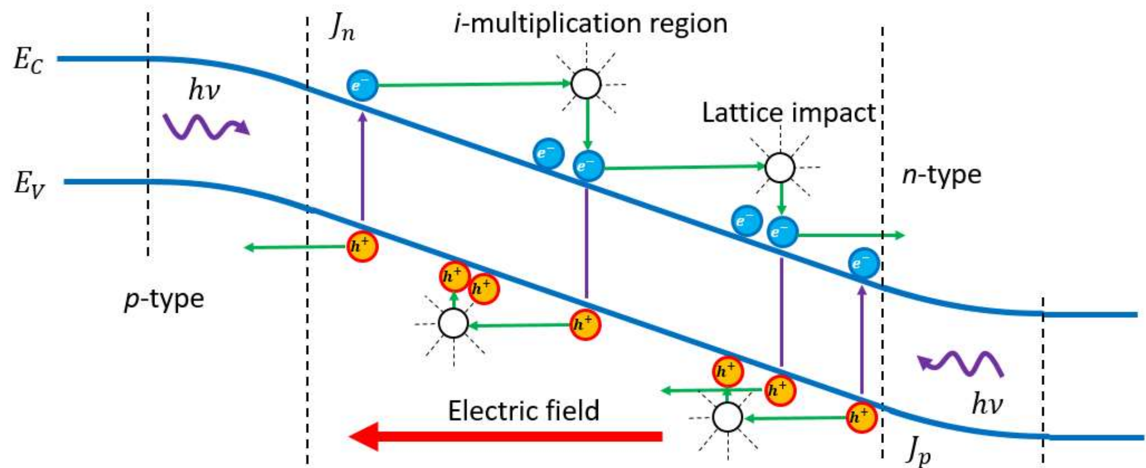


**Figure 1-4 Schematic diagram of the impact-ionization process is depicted.**

There are three modes of photodiode operation: 1) photodiode mode, 2) proportional (linear) mode, and 3) Geiger mode (Figure 1-5) [16]. First let's assume that the impact-ionization coefficient of an electron, $\alpha$, is greater than that of the hole, $\beta$. In the photodiode mode, the applied voltage is small, as well as is the electric field. Most of the photogenerated electrons and holes are swept across the depletion layer, and the overall current is not amplified. In the proportional mode, the applied voltage (and thus the electric field) is increased, the probability of the impact ionization by electrons is high but that of holes is low, only the electrons will participate in the impact ionization process, and holes are swept across the depletion layer. The current is maximum when the last electron arrives at the $n$-layer and the current flows until last hole arrives at the $p$-layer. In Geiger-mode operation, the reverse bias voltage (and the electric field) is sufficiently high, so that the probability of the impact ionization by holes is comparable with that of electrons. This is regenerative avalanche process, with a higher multiplication factor.

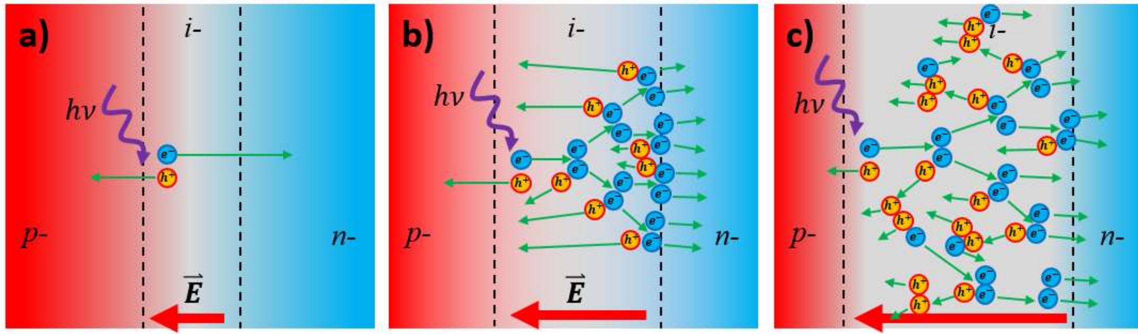


**Figure 1-5 Three modes of operation a) photodiode mode, b) proportional mode, and c) Geiger mode.**

## 1.4 Previous research

### *1.4.1 Photomultiplier tubes and silicon avalanche photodiodes*

Combining a UV photodetector with the Geiger-mode photon counting technique has found numerous applications. These applications include quantum-key distribution (QKD) [17], optical time-domain reflectometry [18], positron emission tomography [19], biomedical research [20], and ultraviolet communication [21]. To enable these applications, bulky and extremely sensitive photodetectors called photomultiplier tubes (PMTs) were used to detect photons in early periods [22]. The PMTs can have high gain, low noise, and high frequency response, but they are bulky, relatively fragile and require high voltage operation of 1 to 2 kV [23]. Moreover, if the PMTs were to operate as UV detectors, bulky and expensive optical filters must be installed to block the visible spectrum.

Alternatively, solid-state photodetectors such as silicon (Si) APDs have been designed to detect UV photons and have been operated in Geiger mode [24]. Compared with the PMTs,

Si APDs have the advantage of exploiting mature Si CMOS processing, enabling the Si APDs to be fabricated into large-area arrays composed of smaller devices. This is important for many applications. Thanks to the mature Si device technology, UV-enhanced Si APDs are commercially available [25]. According to Hamamatsu Photonics, the photon counting modules they currently provide can have a spectral response range down to a wavelength of 320nm, dark count rate of 7 cps, and peak photon detection efficiency of 70% at a wavelength of 450nm [25]. However, like the PMTs, Si APDs designed to operate in the UV need optical filters since silicon has an indirect bandgap of 1.1 eV. To overcome this problem, wide-bandgap compound semiconductor materials such as silicon carbide (SiC) and the III-nitrides have been studied. In principle, these materials have inherent visible blindness, which made them suitable for the fabrication of UV photodetectors.

### *1.4.2 SiC APDs and Geiger-mode operation*

SiC is a semiconductor material containing silicon and carbon, with 250 crystalline forms [26]. Among those forms, 4H-SiC has an indirect bandgap of 3.2 eV [26], which makes it suitable for UV photodetectors. The first demonstrated 4H-SiC APDs achieved a dark current density of 1mA/cm$^2$, a breakdown voltage of 93V, and a maximum spectral responsivity of 106 A/W at a wavelength of 270 nm with a reverse-bias breakdown voltage of -90V [27, 28]. In 2009, a group from the University of Virginia reported large-area recessed-window 4H-SiC *p-i-n* APDs [29]. They achieved a dark current density of 0.6 nA/cm$^2$, a multiplication gain of $10^5$ with breakdown voltage of -142.5V, and maximum spectral responsivity of 110 mA/W at wavelength of 280nm. They also reported dark count probability of $8 \times 10^{-4}$ at a 10kHz pulse frequency, and a photon detection efficiency of 30% at 280nm. In 2017, a group from Nanjing University demonstrated 4H-SiC APDs with a dark

current density of 56 pA/cm$^2$, a multiplication gain of $10^6$ with breakdown voltage of -173.3V, a maximum spectral responsivity of 120 mA/W at a wavelength of 280nm, a dark count rate per unit area of 9Hz/μm$^2$, and a photon detection efficiency of 35% at 280nm [30]. In 2020, the same group at Nanjing University reported a 4H-SiC APD with a dark current density of 56 pA/cm$^2$, a breakdown voltage of 178.4V, a dark count probability of $6.6 \times 10^{-3}$ at a 50kHz pulse frequency, and a photon detection efficiency of 19.8% at 280nm [31]. However, the SiC bandgap cannot be tuned easily, thus SiC APDs also require external UV filters for operating in the solar-blind regime.

### *1.4.3 III-N APDs and Geiger-mode operation*

III-nitride-based UV photodetectors can be categorized into four major types; photoconductors, Schottky-barrier photodetectors, metal-semiconductor-metal photodetectors, and *p-i-n* photodetectors. Among those various photodetectors, p-i-n photodetectors are the most common type of the photodetectors, and have lower dark current density, higher spectral responsivity, higher gain, making them favorable for APD [32, 33]. A research group from APA Optics Inc., have observed avalanche process in *p-i-n* GaN based photodiodes [34], which has dark current density as low as 6μA up to -40V reverse bias, breakdown voltage around -45V and the maximum avalanche gain more than 3. The first III-nitride UV Geiger-mode operating GaN APD was demonstrated by a group at MIT Lincoln Laboratory, [35]. They reported that dark count rate was 400kHz, and an SPDE of 13% measured at 325nm. In the following year, the Lincoln Laboratory group reported the Geiger mode operation of GaN APDs in linear gain mode [36].

In recent publication of GaN APDs, the group from the Northwestern University had achieved a dark current density of 22.2 nA/cm$^2$, a multiplication gain of $5.12 \times 10^4$ with breakdown voltage of -120V, a maximum spectral responsivity of 120 mA/W at wavelength of 364nm, a dark count probability of 0.57 and a photon detection efficiency of 30.5% at a wavelength of 340nm using back-illuminated GaN APDs [37]. In 2018, our lab at Georgia Institute of Technology was able to demonstrate GaN based separate absorption and multiplication (SAM) UV APDs [38]. The structure of the APD employed was *p-i-p-i-n* instead of *p-i-n*, which separates photon absorption region and multiplication region of photon-generated charge carrier. We showed dark current density of 0.1nA/cm$^2$ with a breakdown voltage of 73V, a maximum gain of $5 \times 10^6$, and a maximum spectral responsivity of 320mA/W at wavelength of 376nm at -70V reverse bias. In 2020, The group from Stanford University reported a GaN *n-i-p* inverted APD with a dark current density of 38 μA/cm$^2$ a breakdown voltage of -278V, a maximum gain of $10^5$, and a maximum spectral responsivity of 60A/W at a wavelength of 350nm [39].

The group from the Bilkent University, Turkey has demonstrated the first solar-blind III-nitride APD, with a dark current density of 53pA/cm$^2$ at 5V reverse bias, avalanche breakdown after -72V with an avalanche gain of 25, a spectral responsivity around 110 mA/W at wavelength of 254 nm with a reverse bias of 25V [40]. Since then, the group from Nanjing University published back-illuminated AlGaN SAM APD with and $Al_xGa_{1-x}N$ $x = 45\%$ absorption layer with a dark current density of 0.716 μA/cm$^2$, an avalanche breakdown after -101V with an avalanche gain $5.5 \times 10^4$, and a spectral responsivity of 212 mA/W at wavelength of 275 nm [41]. In 2020, the same group from Nanjing University reported an AlGaN SAM APD with an $Al_xGa_{1-x}N$ $x = 40\%$ absorption layer having a dark current density

of 70.7 nA/cm$^2$, an avalanche breakdown of -86V with an avalanche gain of $10^5$, and a spectral responsivity of 40 mA/W at wavelength of 280 nm [42].

So far, most of the demonstrations of solar-blind AlGaN APDs have been focused on $Al_xGa_{1-x}N$ absorption regions with an AlN mole fraction of $x$~0.4. In 2018, Fraunhofer Institute published the first $Al_{0.65}Ga_{0.35}N$ *p-i-n* APD with a dark current density of 1.27 nA/cm$^2$, an avalanche gain of 5500 at ~-80V, and a spectral responsivity of 58 mA/W at a wavelength of 246 nm [43]. In 2020, Adroit Materials reported $Al_{0.65}Ga_{0.35}N$ APDs grown on a bulk AlN substrate with a dark current density of 0.4 nA/cm$^2$, an breakdown of -340V with an gain of $10^5$, and a spectral responsivity of 90 mA/W at wavelength of 255 nm [44]. Recently, in 2021, Northwestern University reported an $Al_xGa_{1-x}N$ APD with $x > 0.5$, with a dark current density of 1.6 μA/cm2, a gain of 50,000, and an external quantum efficiency of 14% (28.79mA/W) at wavelength of 255nm [45].

# CHAPTER 2. DESIGN, GROWTH, FABRICATION AND CHARACTERIZATION OF DEEP-ULTRAVIOLET ALUMINUM GALLIUM NITRIDE AVALANCHE PHOTODIODES

## 2.1 Introduction

In this project, DUV *p-i-n* APD structures with $Al_{0.6}Ga_{0.4}N$ absorbing regions were designed, grown by MOCVD on a AlN bulk substrate and AlN/sapphire templates with various crystalline quality, fabricated into devices with circular mesas of different detection areas, and the devices were characterized. The devices show distinctive avalanche breakdown *J-V* behaviors, with breakdown voltages around -140V, and a low-leakage current density of $<10^{-8}$ A/cm$^2$. Also, the temperature coefficients of the breakdown voltage were measured to be negative, and the performance of the APDs grown on different AlN substrates was analyzed.

## 2.2 Material characterization

### *2.2.1 X-ray diffraction*

To characterize crystalline materials, X-ray diffraction (XRD) is commonly used. The XRD is convenient and non-destructive characterization method, and is possible to understand structural properties, including alloy composition, crystalline defects, multilayer thicknesses, and strain and relaxation of films [46, 47]. The principle of the XRD is based on Bragg's law, and it is written as

$$2d_{hkl}\sin\theta_B = n\lambda \tag{3}$$

Where $d_{hkl}$ is a spacing between planes in an atomic lattice, $\theta_B$ is the Bragg's angle, $n$ is an order of the diffraction ($\pm 1, \pm 2, \pm 3 \ldots$), and $\lambda$ is wavelength of the X-ray. Copper (Cu) $k\alpha$ radiation is mainly used in the XRD system, and it has wavelength of 1.5406Å. The lattice spacing $d_{hkl}$ is different for each material, but we are interested in hexagonal lattice system. The lattice spacing of the hexagonal lattice system is

$$\frac{1}{d_{hkl}^2} = \frac{4}{3}\frac{h^2 + hk + k^2}{a^2} + \frac{l^2}{c^2} \tag{4}$$

where $a$ and $c$ are lattice constants of the hexagonal lattice system, and $h, k$ and $l$ are the Miller indices of the plane of interest.

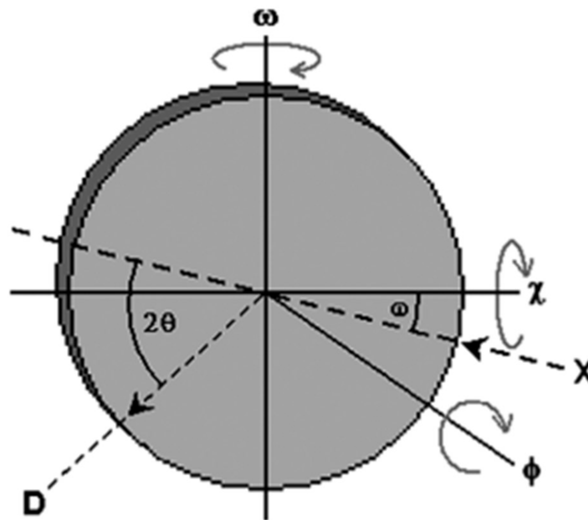


**Figure 2-1 A schematic diagram showing all the axes of rotation [46]. X denotes the X-ray source and D denotes the detector.**

In the X-ray diffraction, the axes of rotation should be defined [46]. Let's assume the X-ray is incident on the sample surface with an incident angle $\omega$. The angle between a detector and an imaginary line of the incident X-ray in the crystal is called $2\theta$. The other angles are $\psi$, which is a sample tilt angle, and $\phi$ which is the in-plane sample rotation angle.

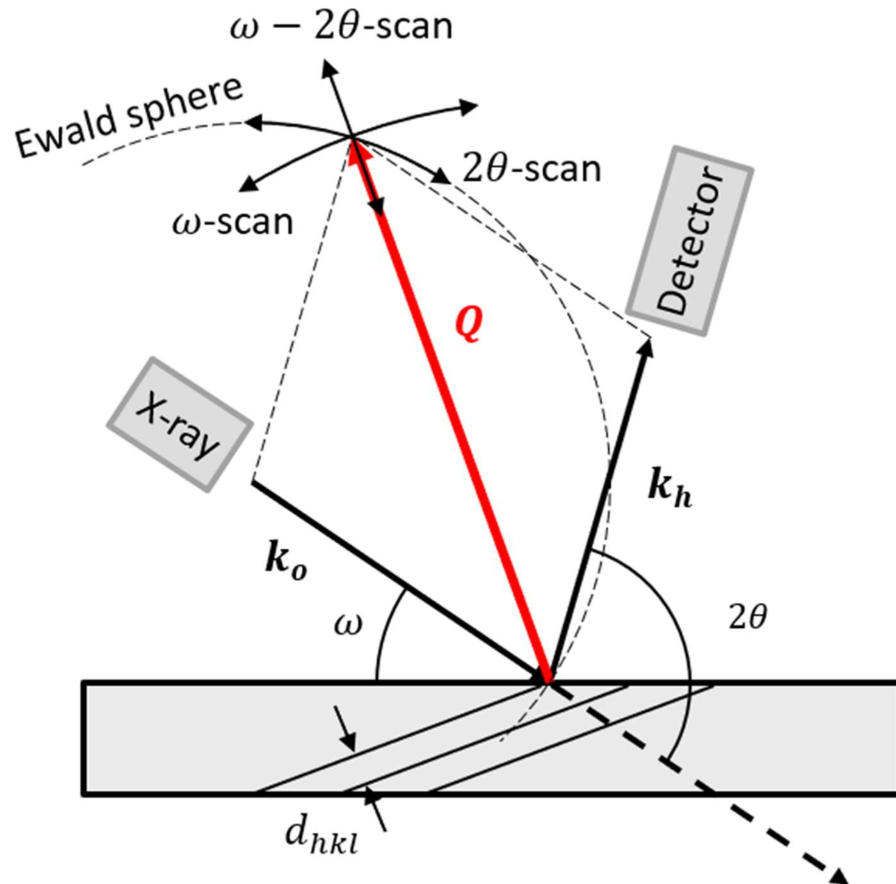


**Figure 2-2 The incident ($k_o$) and diffracted ($k_h$) wavevector forms the scattering vector $Q$, which points to the reciprocal lattice, and lies on the surface of the Ewald sphere. The directions are depicted for different types of scans ($\omega$, $2\theta$ and $\omega$-$2\theta$) in reciprocal space.**

With the rotation axes defined, the diffraction can be explained in reciprocal space. By defining the incident ($\boldsymbol{k_o}$) and diffracted ($\boldsymbol{k_h}$) wavevector ($k = 2\pi/\lambda$), it is possible to define a scattering vector $\boldsymbol{Q}$ where $\boldsymbol{Q} = \boldsymbol{k_h} - \boldsymbol{k_o}$ (Figure 2-2). The scattering vector points to a

reciprocal lattice in the reciprocal space and lies on the surface of a sphere of radius $|2\pi/\lambda|$ called the Ewald sphere.

There are several scan types available in the X-ray diffraction. Mainly, $\omega$ and $2\theta$ angle rotation is used. In the $\omega$-scan, the detector position is fixed, and the sample is rotated about the $\omega$ axis. In the reciprocal space, the scattering vector $\boldsymbol{Q}$ follows an arc centered on the origin. The scattering vector length remains same, and its direction varies. In the $2\theta$ scan, the sample and the source position is fixed, and the detector is rotated. In the reciprocal space, the scattering vector $\boldsymbol{Q}$ follows an arc along the circumference of the Ewald sphere. The length of the scattering vector as well as the direction varies. In the $\omega$-$2\theta$ scan, when the sample rotates an angle of $\omega$, the detector rotates an angle of $2\theta$. Their angular ratio is $\omega: 2\theta = 1: 2$, and the length of the scattering vector varies while the direction is fixed.

There is another commonly used type of scanning called reciprocal space mapping (RSM). This is done by taking a series of $\omega$-$2\theta$ scans at different $\omega$ angles and combining them together to form a map. To plot the reciprocal space map, the angles are converted into the reciprocal lattice $q_x$ and $q_y$ by using below equations.

$$q_x = \frac{2\pi}{\lambda}[cos(2\theta - \omega) - cos\,\omega] \tag{5}$$

$$q_z = \frac{2\pi}{\lambda}[sin(2\theta - \omega) + sin\,\omega] \tag{6}$$

From the reciprocal lattice $q_x$ and $q_y$ it is also possible to determine the lattice constants $a$ and $c$ of a certain semiconductor layer. For the case of aluminum gallium nitride (AlGaN) material, the relationships between $(q_x, q_y)$ and $(a, c)$ are

$$a = \frac{4\pi\sqrt{h^2 + hk + k^2}}{q_x\sqrt{3}} \quad (7)$$

$$c = \frac{2\pi l}{q_z} \quad (8)$$

With the obtained lattice constants $a$ and $c$, AlN mole fraction and strain can also be obtained using following equations.

$$\epsilon_{zz} = \frac{c - c_0(x)}{c_0(x)} \quad (9)$$

$$\epsilon_{xx} = \frac{a - a_0(x)}{a_0(x)} \quad (10)$$

$$c_0(x) = xc_{AlN} + (1 - x)c_{GaN} \quad (11)$$

$$a_0(x) = xa_{AlN} + (1 - x)a_{GaN} \quad (12)$$

$$\epsilon_{zz} = -\frac{2C_{13}(x)}{C_{33}(x)}\epsilon_{xx} \quad (13)$$

$$R(x) = \frac{a(L) - a(S)}{a_0(L) - a_0(S)} \quad (14)$$

$\epsilon_{zz}$ is the strain in out-of-plane direction, $\epsilon_{xx}$ is the strain in in-plane direction, $C_{13}(x)$ and $C_{33}(x)$ are the components of the elastic stiffness tensor of the AlGaN material, $a_0$ and $c_0$ are the lattice constants of the relaxed AlGaN material, and $a$ and $c$ are the lattice constants obtained from the RSM. $R(x)$ is the in-plane relaxation calculated by dividing the difference of the measured lattice constant $a$ with the difference of the calculated lattice constant $a$. The

$L$ and $S$ denotes layer and substrate respectively. Inserting all the equations from (9) to (12) into the equation (13), the equation (13) becomes a cubic equation of $x$. Solving for $x$ analytically using a program such as MATLAB, the AlN mole fraction can be obtained. Also using the equation (14), we obtain the in-plane relaxation.

For the AlGaN heteroepitaxial layers, an asymmetric (105) reflection ($hkl$) is normally used to determine the lattice constants $a$ and $c$, the AlN mole fraction and the strain. The (105) reflection has broader reciprocal space compared with (101) ~ (104) reflection due to high index [46].

### *2.2.2 Absorbance spectra and bandgap energy*

The bandgap energy is one of the important measurement parameters in the field of semiconductors. The bandgap energy of a semiconductor is the energy required for an electron to be excited from the valence band to the lowest-energy conduction band. There are various methods to determine the bandgap energy of the material, and one of the methods is by using absorbance spectrum measurements and the Tauc method [48]. To use the Tauc method, it is assumed that the absorbance α can be expressed by the below expression,

$$(\alpha \cdot h\nu)^{1/\gamma} = B(h\nu - E_g) \tag{15}$$

where $h$ is the Planck constant, ν is the frequency of the photon, $E_g$ is the bandgap energy, and $B$ is a constant. The factor $\gamma$ is equal to ½ for a direct- and 2 for indirect-bandgap transitions. To apply equation (15) for AlGaN materials (they are all direct bandgap), the

absorbance spectrum is measured, and the data are multiplied with the energy of the photon ($h\nu$), squared, then plotted vs. photon energy. The approximate bandgap energy can be obtained by drawing two tangent lines to the data plots and calculating the $x$-intersection (Figure 2-3a). The absorbance spectra of the AlGaN material samples were measured with a Shimadzu UV-VIS 2401 PC spectrophotometer.

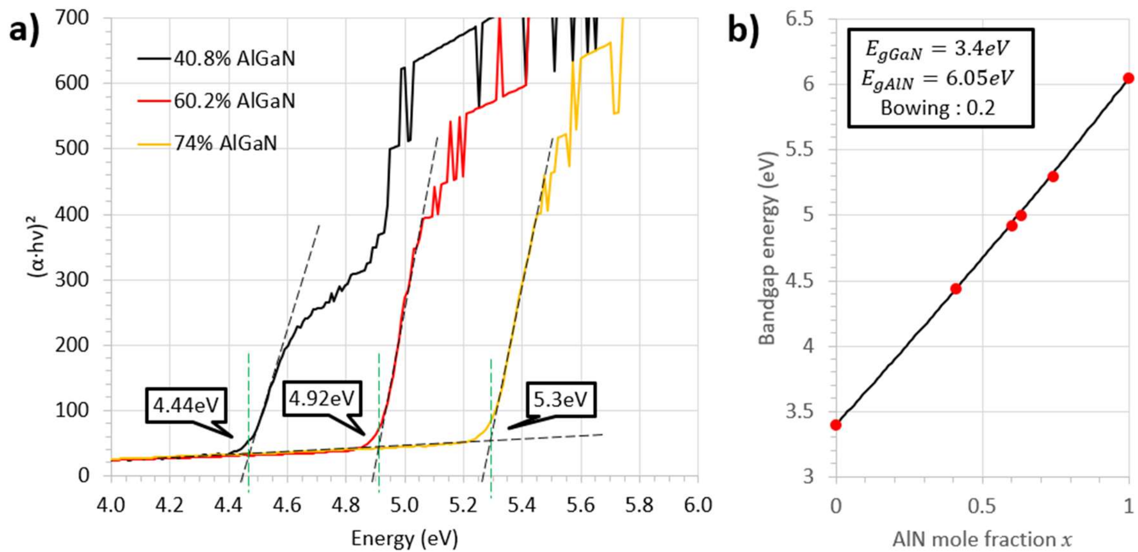


**Figure 2-3 a) Absorbance spectra of $Al_{0.408}Ga_{0.592}N$, $Al_{0.602}Ga_{0.398}N$, and $Al_{0.74}Ga_{0.26}N$ are shown. The bandgap energy can be obtained by drawing two tangent line and calculating the intersection point. b) The bandgap energy vs AlN mole fraction $x$ is plotted. The bandgap energies of GaN and AlN were obtained by Tauc method as well.**

## 2.3 Device characterization

The device characterization consists of three parts; 1) measurement of the voltage-current ($I$-$V$) or voltage-current density ($J$-$V$) characteristics, 2) spectral responsivity using a

variable-wavelength light source, and (3) photoresponse using a single-wavelength light source.

### *2.3.1 Current Voltage (I-V) characteristics and gain calculation*

To measure the *I-V* characteristics of the GaN *p-i-n* APD, the diode anode and cathode are connected to a Keithley 4200 Semiconductor Characterization System. Then a reverse bias voltage is applied to the device, and the voltage is swept from zero to -200V. To get the current density, the I-V characteristic is divided by the mesa area of the device. If the APD device is measured without the light source, then the *I-V* characteristic is called the dark-current *I-V* characteristic, and if measured with the light source on, it is called the photocurrent *I-V* characteristic. To measure the photocurrent, the light source setup must be installed. The light source setup consists of a UV lamp (Newport Apex Illuminator housing with an ozone-free 150W Oriel Xenon Lamp), a Newport Cornerstone 260 Monochromator system, and a UV-grade optical fiber that directs the light from the monochromator to the photosensitive area of the APD device. Additionally, a shutter is needed to completely block the light during the dark-current measurement.

By comparing the photocurrent with the dark-current, the avalanche gain can be calculated. The avalanche gain is evaluated as;

$$G = \frac{I_{ph} - I_{dark}}{I_{ph(unity)} - I_{dark(unity)}} \tag{16}$$

where $I_{ph}$ is the photo-current, $I_{dark}$ is the dark-current, $I_{ph(unity)}$ is the unity photo-current, and $I_{dark(unity)}$ is unity dark-current. The unity dark/photo-current is defined as the average of the dark/photo-current from zero-bias until a certain reverse bias where the current is similar with the zero-bias current.

### *2.3.2 Spectral responsivity or photoresponse measurements*

Spectral responsivity ($R$) is a term for evaluating detector efficiency vs. wavelength, which is basically electrical current output per optical power input. It is usually expressed in units of amperes per watt (A/W) and is typically defined as the ratio of the photocurrent ($I_{ph}$) to the input optical power ($W_{ph}$) at a specific wavelength of the light that detector detects. The term spectral responsivity is interchangeably used with quantum efficiency ($\eta$), which has definition of ratio of the number of the photocurrent carriers created due to the input light to the number of the photons impinging on the device. The relationship between the spectral responsivity and the quantum efficiency is described in the equation (17),

$$R = \frac{I_{ph}}{W_{ph}}[A/W] = \eta\frac{q}{h\nu} = \eta\frac{q\lambda}{1240} \tag{17}$$

where $I_{ph}$ is the measured photocurrent of the APD device, $W_{ph}$ is the incident optical power illuminating the APD device, $q$ is an electrical charge, $h$ is the Planck's constant, $\nu$ is the photon frequency, and $\lambda$ is the wavelength of the light in nm. Consideration should be made for the wavelength dependence of the reflectivity of the surface of the APD device.

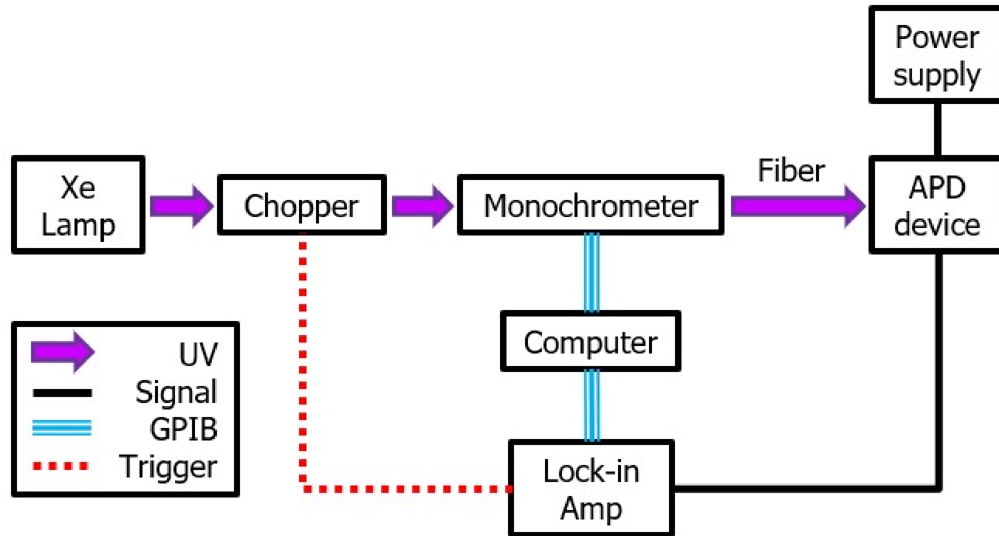


**Figure 2-4 A schematic diagram of the spectral responsivity measurement setup using a variable-wavelength light source.**

Figure 2-4 is a schematic diagram of the spectral responsivity measurement setup used in this study [49-51]. The light source is the Newport Apex Illuminator with an ozone-free 150W Oriel xenon lamp, providing the UV light in the spectral range from 200nm to 400nm. The Newport Cornerstone 260 Monochromator system selects a single wavelength of the input optical signal. An optical chopper is inserted between the lamp and the monochrometer to modulate the illuminating light at a 100 Hz frequency. Then the selected single wavelength of the optical signal at the output of the monochrometer is coupled using ½ inch diameter UV focus lens through the multimode UV fiber having a 100 μm diameter. The other end of the UV fiber is directed to the APD photosensitive surface and positioned as close as possible. The cathode of the device is connected to the power supply (a Keithley 4200 Semiconductor Characterization System) to apply reverse bias, and the anode of the device is connected to a Stanford Research System 830 lock-in amplifier to collect the photocurrent data. The

monochrometer and the lock-in amplifier are controlled by the computer with HP VEE software program through a GPIB interface.

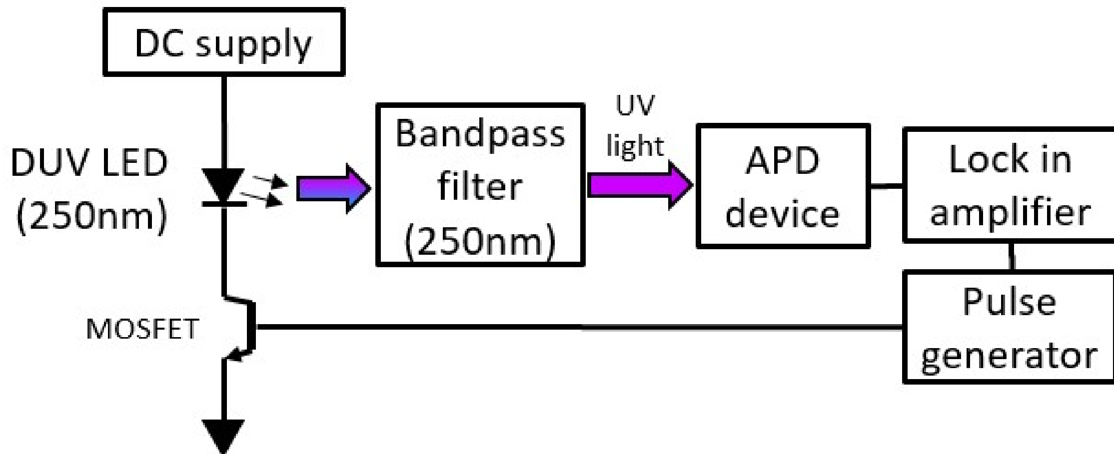


**Figure 2-5 The calibreated photoresponse measurement using a DUV LED with 250nm emission wavelength.**

For the calibrated photoresponse measurements, a DUV LED with 250 nm emission wavelength and a ½-inch diameter bandpass filter centered at 250 nm (FWHM of 10nm) were used for illuminating the AlGaN DUV APD (Figure 6a). The bandpass filter was required to filter unwanted visible light emission at ~480 nm that is emitted from the DUV LED. A MOSFET was connected in series with the DUV LED, which is modulated with a rectangular pulse train of 125 Hz frequency. Then the cathode of the APD device was connected to the power supply to apply a reverse bias, and the anode of the device was connected to a Stanford Research System 830 lock-in amplifier to collect the photocurrent data. A synchronous 125

Hz rectangular pulse train was also sent to the lock in amplifier as well. A calibrated UV Si photodiode was used to measure the input optical power from the DUV LED.

## 2.4 Design of deep UV (DUV) AlGaN *p-i-n* APDs

The objective in the design is to build an $Al_xGa_{1-x}N$ APD structure with a peak absorption wavelength around 240~260nm (which corresponds to an AlN mole fraction, $x$, of 0.6), with low leakage current and distinctive avalanche breakdown. Since it is a prototype design, we start with a standard *p-i-n* structure. Above an *i*-$Al_{0.6}Ga_{0.4}N$ absorption layer, a *p*-$Al_{0.6}Ga_{0.4}N$ layer grades in Al alloy composition to a *p*-GaN layer. Below the *i*-$Al_{0.6}Ga_{0.4}N$ layer, an *n*-$Al_{0.6}Ga_{0.4}N$ layer grades to an *i*-$Al_{0.8}Ga_{0.2}N$/AlN layer (Figure 2-6).

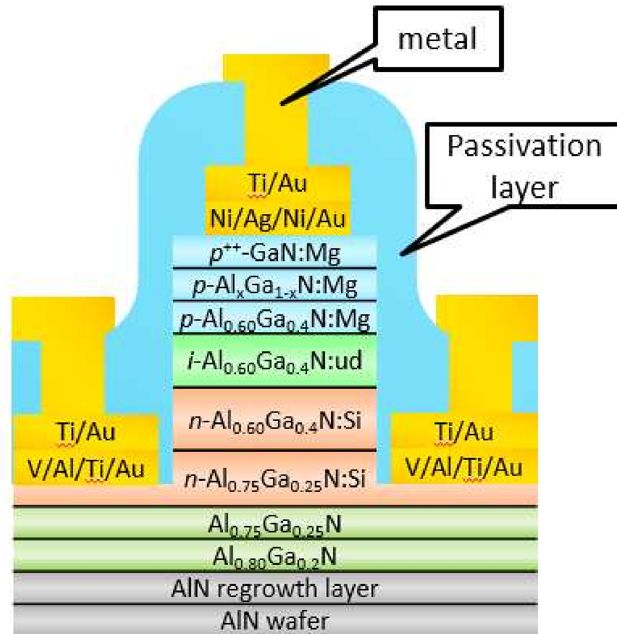


**Figure 2-6 Schematic design of the deep UV $Al_xGa_{1-x}N$ APD with $x = 0.6$.**

When designing for the DUV AlGaN *p-i-n* APD, there are number of aspects to consider. Some aspects must require feedbacks from growth or fabrication steps. We will discuss these aspects one by one.

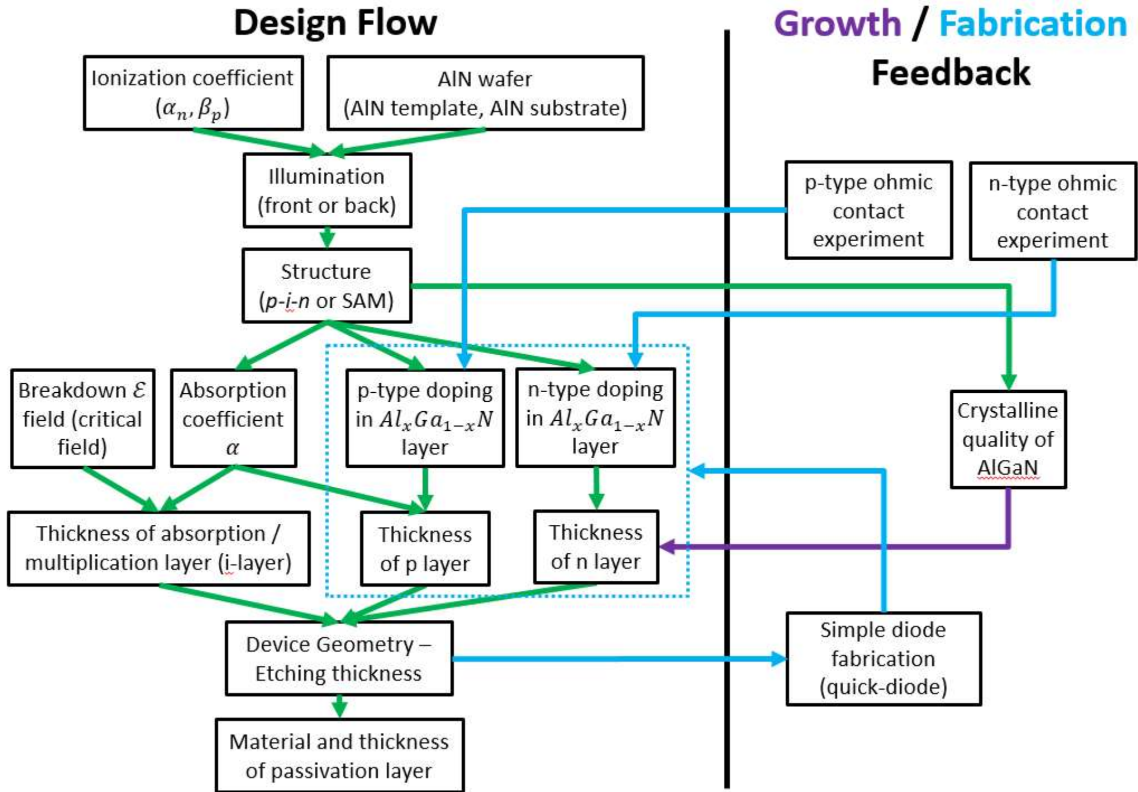


**Figure 2-7 The flow of the design, and some of the aspects require feedbacks from growth or fabrication step.**

### *2.4.1 Excess noise, ionization coefficient and front/back illumination*

The avalanche process generates excess noise ($F_i(M)$) or amplification noise due to statistical nature of the avalanche process. The excess noise can be expressed in two ways depending on which carrier is injected into the multiplication region [15, 52].

$$F = \frac{\beta}{\alpha}\langle M \rangle + \left(1 - \frac{\beta}{\alpha}\right)\left(2 - \frac{1}{\langle M \rangle}\right) \tag{18}$$

$$F = \frac{\alpha}{\beta}\langle M \rangle + \left(1 - \frac{\alpha}{\beta}\right)\left(2 - \frac{1}{\langle M \rangle}\right) \tag{19}$$

The $M$ is the multiplication factor (avalanche gain). The equation (18) is the excess noise from an electron injection, and the equation (19) is the excess noise from a hole injection. $\beta$ is the hole ionization coefficient, and $\alpha$ is the electron ionization coefficient. The ionization coefficient is an average number of electron-hole pairs created by either an electron or a hole per unit of distance in centimeters while the electron or the hole is moving in the high electric field. The ratio $k = \beta/\alpha$ is used for the electron injection ratio, and $1/k = \alpha/\beta$ is used for the hole injection ratio. The excess noise factor increases as the multiplication factor increases but decreases as the ratio $k$ or $1/k$ decreases. Thus, to achieve low noise, 1) the impact ionization coefficient of the carriers must differ sufficiently, and 2) the avalanche process should be initiated by the carrier having the higher ionization coefficient.

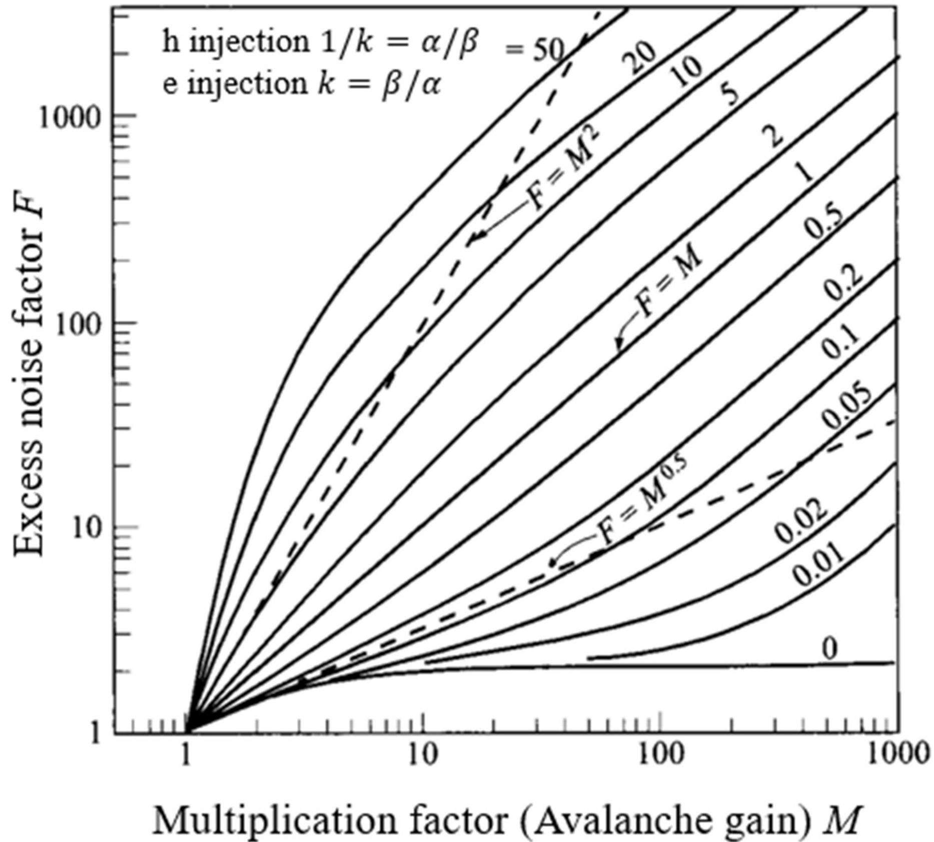


**Figure 2-8 A plot of the excess noise factor versus the multiplication factor [15] The ratio $k = \beta/\alpha$ is used for the electron injection ratio, and $1/k = \alpha/\beta$ is used for the hole injection ratio. The excess noise factor increases as the multiplication factor increases but decreases as the ratio $k$ or $1/k$ decreases.**

For the GaN material, the hole ionization coefficient ($4\sim5 \times 10^4/cm$ at $3MV/cm$) is larger than the electron ionization coefficient ($0.2\sim1 \times 10^4/cm$ at $3MV/cm$) [53-55], and these coefficients depends on the electric field. The hole-initiated multiplication process can be achieved by illuminating from the back, for the *p-i-n* diode with the *p*-side on the top. The illumination from the *n*-side (back side) is preferred for the GaN *p-i-n* APD. However, for the AlGaN material, the ratio of hole to electron ionization coefficient $k = \beta/\alpha$ varies from larger than 1 (below $x = 0.5$) to much smaller than 1 (above $x = 0.6$) (Figure 2-9). Thus the

electron-initiated multiplication process is preferred, and the illumination from the *p*-side is more preferred at least from this point of view.

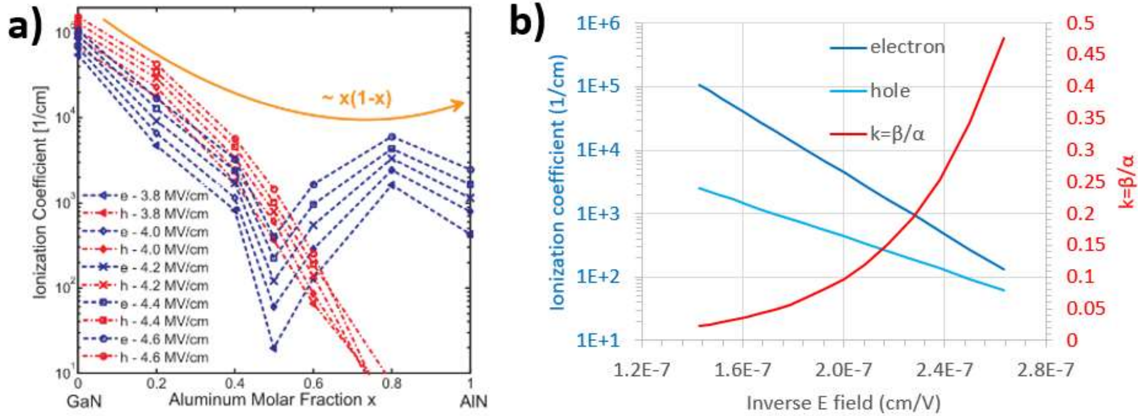


**Figure 2-9 a) The ionization coefficient for $Al_xGa_{1-x}N$ material. Notice that the electron ionization coefficient gets bigger than the hole ionization coefficient once $x$ reaches 0.6. b) The ionization coefficients of the carriers for the $Al_{0.6}Ga_{0.4}N$ material is shown. Notice that the ratio of electron ($\beta$) to hole ($\alpha$) ionization coefficient $k = \beta/\alpha$ is always less than 1 for all the electric field.**

### *2.4.2 Aluminum nitride (AlN) template vs. AlN substrate*

Before growing the full AlGaN APD structure, two types of aluminium nitride (AlN) on sapphire templates were prepared: 1) MOCVD grown AlN (thickness = 2.5 µm) on (0001) sapphire ($T_{substrate}$ ~430 µm) via a conventional high-temperature growth technique [56], and 2) MOCVD grown AlN (thickness = 0.97 µm) on high-temperature sputtered and annealed AlN (thickness ~1.1 µm) deposited on (0001) sapphire [57]. These two types of AlN templates consist of heteroepitaxial AlN layers few µm thick grown on 2-in diameter c-plane oriented sapphire wafers. (For the rest of the thesis, we refer these AlN/sapphire template as "Type-A" and "Type-B" AlN templates, respectively) Besides these AlN templates, a commercially

available 1-inch diameter *c*-plane oriented AlN bulk substrate ($T_{substrate}$ ~550 μm) was also employed.

The growth process of the Type-A AlN template is based on the three-step growth method: 1) 1$^{st}$ buffer AlN layer, 2) annealing at high temperature and 2$^{nd}$ buffer AlN layer, 3) main AlN layer [56]. On the other hand, the growth process of Type-B AlN template is based on the four-step growth method, and requires different equipment at each step: 1) RF sputtering of ~170 nm thick AlN on the sapphire wafer, 2) annealing at a temperature of 1700ºC for 3 hours in a nitrogen ambient, 3) cleaning at 1300ºC for 10 min, then 4) ~970 nm thick AlN growth at 1300ºC [57].

The Type-A AlN templates typically have XRD FWHM of (002) and (102) ω-scans of ~340 and ~570 arcsec, respectively. This corresponds to an estimated dislocation density of ~$10^9$ cm$^{-3}$ [58]. The Type-B AlN template used here has (002) and (102) FWHMs of ~76 and ~248 arcsec, respectively, and dislocation density of ~$2\times10^8$ cm$^{-3}$ as evaluated by plan-view transmission electron microscope [57], which has better quality in terms of dislocation density than that of the Type-A AlN template. The AlN bulk substrate exhibits (002) and (102) FWHMs of ~25 and ~53 arcsec, and has much lower dislocation density (< $10^{-3}$ cm$^{-3}$) [59] compared to these AlN templates. However, the AlN bulk substrate sufferer from strong defect-related optical absorption losses with a cut-off wavelength around 265nm due to a complex of Al vacancies and O on N site impurities [60]. Due to this absorption in the AlN bulk substrate, we designed a front-illuminated AlGaN APD structure.

### 2.4.3 Breakdown electric field of $Al_xGa_{1-x}N$

The empirical expression for the breakdown electric field ($E_{br}$) as a function of the bandgap energy ($E_g$) can be written as [61],

$$E_{br} \propto E_g^{2.5} \tag{20}$$

With the breakdown electric field of the GaN about 3.3*MV/cm* and the AlN about 11.7*MV/cm* [61], it is possible to plot the breakdown electric field versus the AlN mole fraction $x$ (Figure 2-10). The research group from NIT corporation in Japan calculated the breakdown electric field from the breakdown voltage ($V_{br}$) and the thickness of the *i*-AlGaN layer ($W$) [62], using below equation.

$$V_{br} = E_{br}W - \frac{qN_D W^2}{2\epsilon} \tag{21}$$

In the above equation, $N_D$ is residual carrier concentration in the *i*-AlGaN layer, $\epsilon$ is the dielectric constant of the *i*-AlGaN layer. If the breakdown voltage is high, the 2nd term can be ignored (at $N_D = 5 \times 10^{17}/cm^3$, $\frac{qN_D W^2}{2\epsilon} \sim 1V$). Then the equation (21) simplifies to $V_{br} \cong E_{br}W$. They reported the breakdown electric field of $8.1 MV/cm$ for $Al_{0.57}Ga_{0.43}N$ material.

From these two references, we estimated the breakdown electric field of $E_{br} = 7.3 \sim 8.4\ MV/cm$ ( $7.89 MV/cm$ average) for the $Al_{0.6}Ga_{0.4}N$ material. Since our I-V measurement power source (Keithley 4200 SCS) has a voltage limit up to 200V, the maximum thickness of the *i*-layer in an $Al_{0.6}Ga_{0.4}n$-based APD possible for us to analyze is $\frac{V_{br}}{E_{br}} \cong 250nm$.

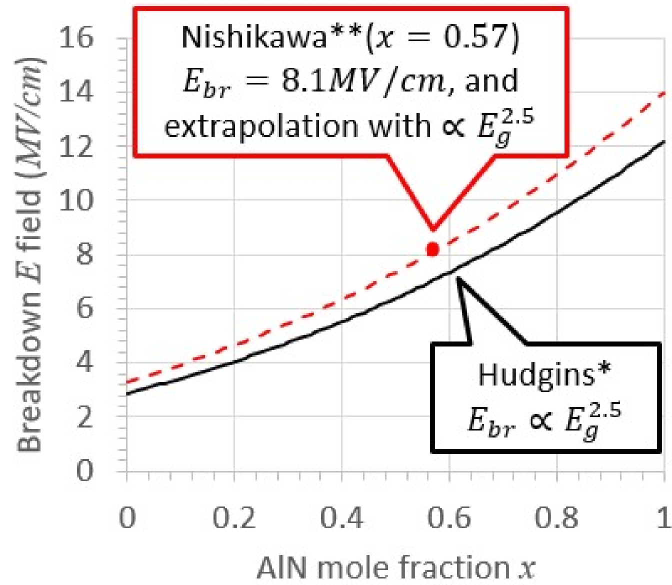


**Figure 2-10 A plot of the breakdown electric field versus the AlN mole fraction x. The black solid line represents the equation (20), with the breakdown electric field value provided in the paper [61]. The red dot represents the breakdown electric field at $x = 0.57$, and red dashed line is an extrapolated line using equation (20)**

### *2.4.4 Absorption coefficient and thickness of absorption/multiplication layer (i-layer)*

Absorption coefficients of $Al_xGa_{1-x}N$ can be found in Muth's article [63], and an absorption coefficient of $Al_{0.6}Ga_{0.4}N$ can be obtained by interpolating the data from the article (Figure 2-11). Then the absorption wavelength is chosen slightly above the cut-off wavelength of absorption, which is 244nm and the absorption coefficient is $\alpha \sim 12.5 \times 10^4/cm$.

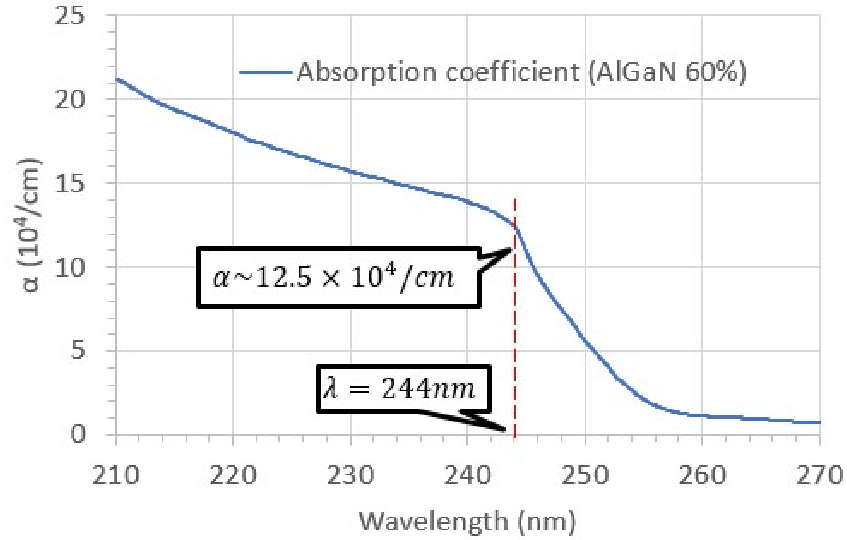


**Figure 2-11 The interpolated absorption coefficient of the $Al_{0.6}Ga_{0.4}N$ from Muth's article [63]. The absorption wavelength is chosen slightly above the cut-off wavelength of absorption, which is 244nm.**

To obtain the highest sensitivity, the absorption layer should be sufficiently thick. Most often, in Si APD, the thickness of the absorption region is designed as $\sim 2/\alpha$ [64], where $\alpha$ is the absorption coefficient. This is derived from the Beer-Lambert law, which the reduction of a photon flux is $e^2$-fold. For the $Al_{0.6}Ga_{0.4}N$, the equivalent absorption layer thickness is $\frac{2}{\alpha} = 160n$.

### 2.4.5 *Thickness of p-type and n-type layers*

For all the *p*-type layers in *p*-on-*n* APDs, the thickness should be as thin as possible to reduce optical absorption due to the acceptor states. A thinner *p*-type layer will also be beneficial for reducing the probability of creating defect sites. For the *p*-contact layer ($p^{++}$-GaN:Mg), the maximum thickness is 20nm, and above this thickness will degrade the quality

of the contact layer for the *p*-type Ohmic contact. The *p*-$Al_xGa_{1-x}N$ graded layer is required for smooth transition from the $Al_{0.6}Ga_{0.4}N$ to the GaN to reduce hetero-interface strain and the possibility of cracking. Also, the thickness of this graded layer is set to 20nm. The *p*-$Al_{0.6}Ga_{0.4}N$ layer thickness is set to 50nm.

The total thickness of an *n*-layer should be at least 750nm thick for better conductivity, and ease of fabrication. The *n*-layer is split into a 250nm thick *n*-$Al_{0.6}Ga_{0.4}N$:Si layer and a 500nm thick *n*-$Al_{0.75}Ga_{0.25}N$:Si layer. The *n*-$Al_{0.75}Ga_{0.25}N$:Si layer is intentionally inserted to gradually change from an $Al_{0.8}Ga_{0.2}N$ layer to an *n*-$Al_{0.6}Ga_{0.4}N$ layer. A 200nm thick $Al_{0.75}Ga_{0.25}N$ layer is inserted for smooth transition from the $Al_{0.8}Ga_{0.2}N$ layer to the *n*-$Al_{0.75}Ga_{0.25}N$ layer as well.

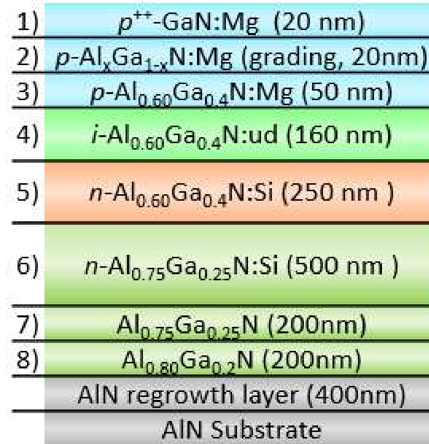


**Figure 2-12 The thicknesses of 1st to 8th layer are shown.**

### *2.4.6 Passivation layer material and thickness*

The refractive index of a passivation layer should be $n_{passive} = \sqrt{n_0 n_s}$ [64], where $n_0$ is the refractive index of an air, and $n_s$ is the refractive index of the semiconductor surface (In our design, it is the GaN). The refractive index of the GaN material is not defined in the literature for the wavelength around 240 ~250nm, but it is assumed to be greater than 2.5 [63]. Assuming $n_s = 2.5$, the refractive index of the passivation layer should be $n_{passive} \sim 1.58$. The good starting material is a PECVD deposited silicon oxide, which has the refractive index of 1.529 at 244nm.

The minimum breakdown electric field of the PECVD deposited silicon oxide is $8MV/cm$ [65]. The passivation layer should be thick enough not to cause a dielectric breakdown. We assume that the PECVD deposited silicon oxide must withstand 200V (maximum voltage for I-V measurement equipment), which corresponds to the minimum thickness of 250nm. However, for an actual APD device fabrication, the PECVD deposited silicon oxide thickness should be around the etched depth of the AlGaN APD structure, i.e., from the top surface down to the *n*-$Al_{0.75}Ga_{0.25}N$:Si layer. The etched thickness is 500nm, thus the PECVD oxide thickness should be 500nm for a conformal deposition.

## 2.5 Growth of deep-UV AlGaN *p-i-n* APDs

### *2.5.1 Calibration of AlGaN layers*

To begin calibration of the MOCVD growth conditions for AlGaN layers, we started with a standard recipe that had been established in earlier work. The standard recipe has a total flow rate of 8000 sccm, and a growth pressure of 100 mbar. The ammonia flow rate is

set to 3000 sccm, which gives a high V/III ratio of more than 1,000 (total Group III molar flow rate of $20 \sim 70 \mu mol/min$). Increasing the ammonia partial pressure can lower the unintentional carbon impurity incorporation during the growth [66]. However, too high of an ammonia flow rate causes increased pre-reaction rate with the TMAl molecules, so to compensate, the gap (or spacing) between the reactor chamber showerhead and the SiC-coated graphite susceptor is reduced from 9mm to 6mm (the minimum value for this reactor) [67].

| | Layer | Temp. (°C) | AlN mole fraction |
|---|---|---|---|
| 1) | $p^{++}$-GaN:Mg | 1010 | 0 |
| 2) | $p$-$Al_xGa_{1-x}N$:Mg | | Grading |
| 3) | $p$-$Al_{0.60}Ga_{0.4}N$:Mg | | 0.6 |
| 4) | $i$-$Al_{0.60}Ga_{0.4}N$:ud | 1060 | 0.6 |
| 5) | $n$-$Al_{0.60}Ga_{0.4}N$:Si | | |
| 6) | $n$-$Al_{0.75}Ga_{0.25}N$:Si | | 0.75 |
| 7) | $Al_{0.75}Ga_{0.25}N$ | | |
| 8) | $Al_{0.80}Ga_{0.2}N$ | 1245 | 0.8 |
| | AlN regrowth layer | | |
| | AlN Substrate | | |

**Figure 2-13 The schematic diagram of each layer in the $Al_xGa_{1-x}N$ APD structure showing target growth temperatures and target AlN mole fractions**

The growth temperature set points are different for each layer. For the $Al_{0.8}Ga_{0.2}N$ layer, the growth temperature was set to 1245°C, which is higher than the standard recipe. The crystalline quality is better when the AlGaN layer was grown in high temperature [68]. For the $Al_{0.75}Ga_{0.25}N$ layer and the $Al_{0.6}Ga_{0.4}N$ layer, the growth temperature was set to 1060°C. For the $p$-AlGaN layers, the growth temperature was set to 1010°C.

The overall growth rate was set to fixed value of 0.2nm/s. The main idea of keeping the growth rate at a fixed value is to help ease the doping calibration experiments. Let's assume that the optimization of one layer with a specific composition and doping calibration is complete, and we are trying to growth another layer with different composition. It is possible to obtain the growth condition with different composition by changing TMAl flow rate. However, when the $Al_xGa_{1-x}N$ composition deviates, the growth is often accompanied by change of the growth rate which is also affects the doping concentrations and free-carrier concentrations. Thus, keeping the growth rate constant will save time in completing the doping calibrations.

The grow rate is proportional to the total Group III precursor flow rates (TMAl+TMGa combined) [68]. Thus we have to find the certain total Group III flow rate conditions that gives a growth rate of 0.2nm/s. Then we change the TMAl molar flow rate, while keeping the total Group III molar flow rate constant. (the $Al_xGa_{1-x}N$ mole fraction $x$ is proportional to the Al/(Al+Ga) molar flow ratio [69]) This way, we can find the target AlN mole fraction $x$. The AlN mole fraction $x$ of each layer was measured using the XRD RSM (Figure 2-14).

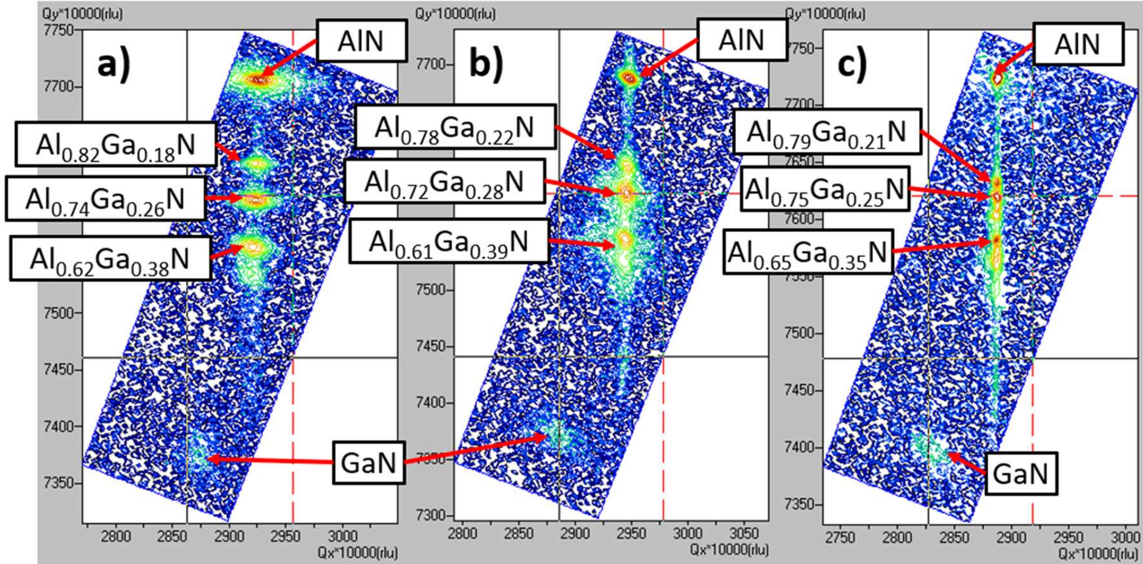


**Figure 2-14 The reciprocal space mapping (RSM) around the (105) reflection of the AlGaN APD structure grown on a) the Type-A AlN template, b) the Type-B AlN template, and c) the AlN bulk substrate. Notice that the peaks in the XRD RSM of the AlN bulk substrate are the narrowest.**

Once the TMAl and the TMGa growth conditions for the $Al_{0.75}Ga_{0.25}N$ layer and the $Al_{0.6}Ga_{0.4}N$ layer are found, silane was included in the growth process to provide the *n*-type doping using Si donor atoms. Silane (200ppm in $H_2$) flow rate conditions are usually expressed in the silicon to total Group III ratio (Si/III). Several *n*-$Al_{0.75}Ga_{0.25}N$ and *n*-$Al_{0.6}Ga_{0.4}N$ samples grown with various silane flow rates were prepared for electrical characterization by breaking the wafers into ~1cm x 1cm squares. Next, four ohmic contact metal regions with 2mm diameter were deposited by evaporation on the *n*-type sample surfaces and Hall-effect measurements were performed at 300K. From the Hall-effect measurements, the free-electron concentration, electron mobility, and resistivity data of each sample at 300K were collected, and plotted (Figure 2-15a,b,c). The target doping was set to $n{\sim}5 \times 10^{18}/cm^3$ after the feedback from the prior device fabrication process development

studies. By interpolating the graph of the free-electron concentration vs. Si/III ratio, the optimized Si/III ratio can be obtained for the target doping concentration.

To obtain the *p*-type doping growth conditions for GaN films, the TMGa flow rate was optimized to obtain the best GaN growth conditions first, then several samples grown with various $Cp_2Mg$ flow rates were prepared and processed as described for the *n*-type layers (but with a different evaporated metal stack). The Hall-effect measurements were performed at 300K, and the free-hole concentration, hole mobility, and resistivity data of the Mg-doped GaN samples were collected and plotted (Figure 2-15d,e,f). The target doping was set to maximum effective doping available for *p*-type GaN, which is a free-hole concentration of $p{\sim}7 \times 10^{17}/cm^3$. Since it is assumed that the optimized doping is similar for all *p*-$Al_xGa_{1-x}N$ layers if the growth rate is same, the optimized $Cp_2Mg$ flow rate condition found in the *p*-GaN growth studies can be applied for the *p*-$Al_xGa_{1-x}N$ growth.

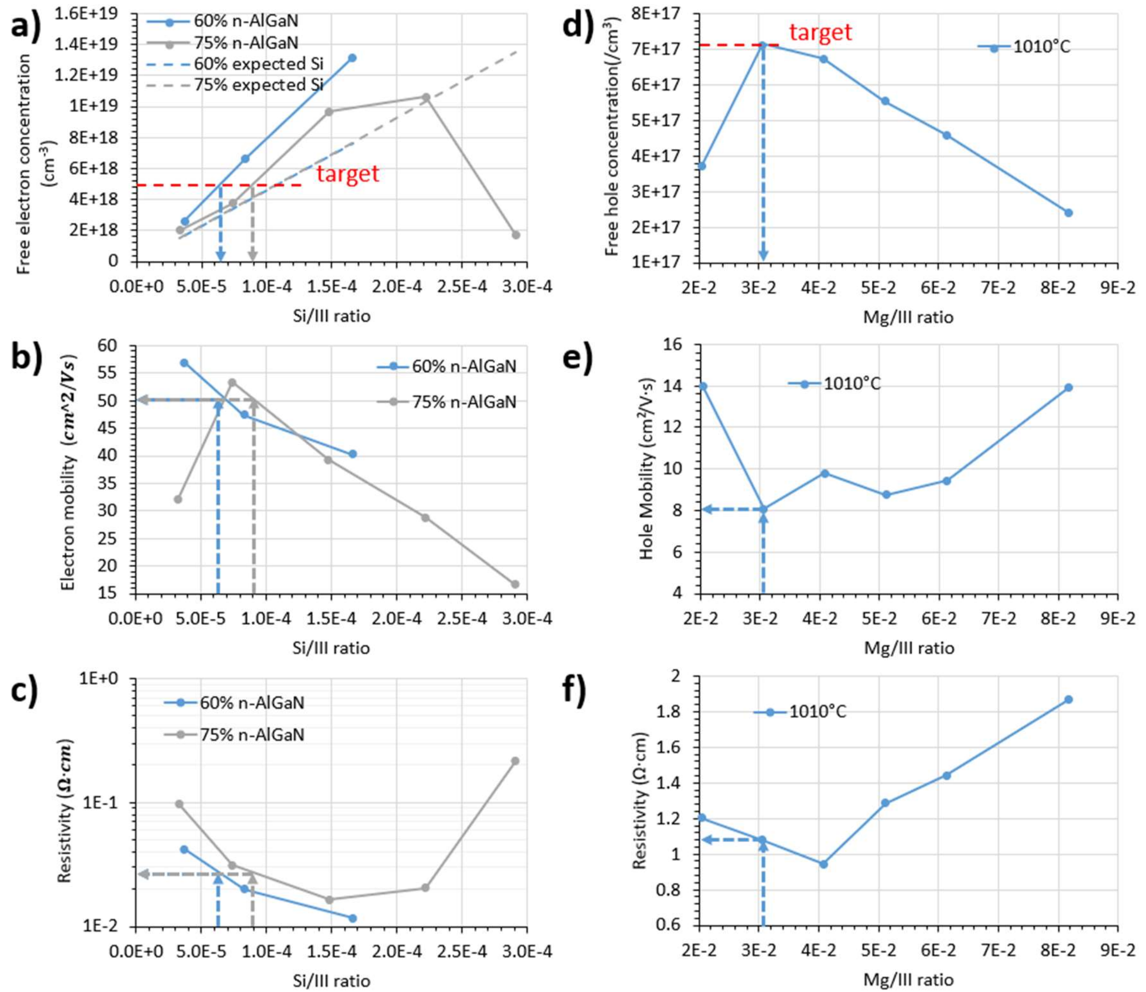


**Figure 2-15 Electrical data on $Al_xGa_{1-x}N$:Si *n*-type films: a) Free-electron concentration, b) electron mobility, c) resistivity are plotted versus Si/III ratio, and electrical data on GaN:Mg *p*-type films: d) free-hole concentration, e) hole mobility, f) resistivity are plotted versus Mg/III ratio. From the free-electron concentration vs. Si/III graph, it is possible to interpolate the Si/III ratio for the target doping. With the Si/III ratio, it is also possible to estimate the electron mobility and the resistivity of the sample. Same technique can be applied to the free-hole concentration vs. Mg/III graph.**

Lastly, the growth conditions for the $p^+$-GaN contact layer were calibrated. To optimize the *p*-side contact layer growth conditions, feedback from the electrical materials characterization process was required. Three heavily-Mg-doped GaN *p*-type samples were

grown with various $Cp_2Mg$ flow rates, then *p*-type contact metals (Ni/Ag/Ni/Au) were deposited by e-beam evaporation, and annealed under a compressed-dry-air ambient at 475°C. Then the *I-V* curves of transmission line measurement (TLM) patterns were measured, and the *I-V* curves were inspected to see whether the *p*-type contact exhibited Ohmic behavior without any Schottky barrier component (Figure 2-16).

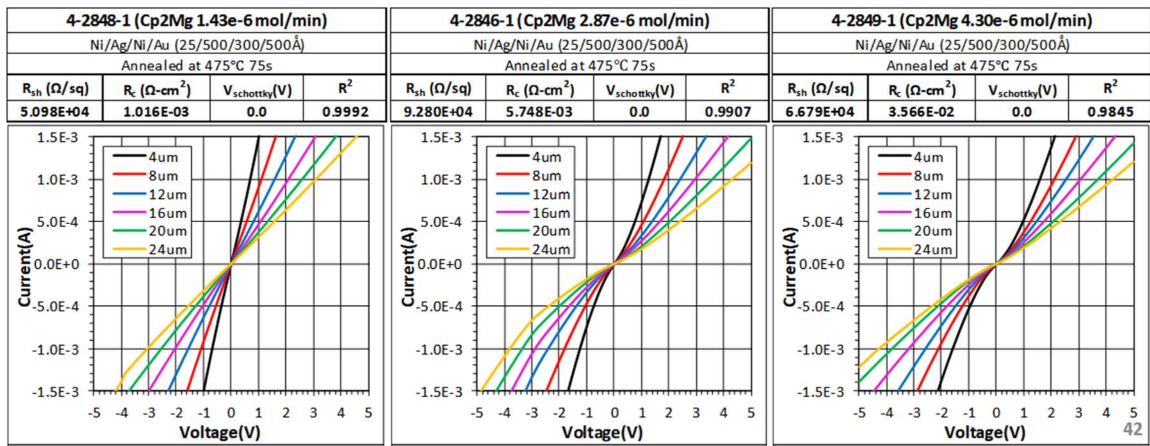


**Figure 2-16 The *I-V* curves of the transmission line measurement (TLM) patterns of *p*+-GaN samples grown with various $Cp_2Mg$ flow rates. In the above graph, the sample with a $Cp_2Mg$ flow rate of $1.43 \times 10^{-6} mol/min$ has the ohmic contact.**

Table 1 is a summary of the calibrated AlGaN APD structure growth parameters for each of the layers.

**Table 1 Calibrated AlGaN APD structure growth parameters.**

| Layer | Tg (°C) | Pressure (mbar) | TMAl (mol/min) | TMGa (mol/min) | $NH_3$ (mol/min) | $SiH_4$ (mol/min) | Si/III |
|---|---|---|---|---|---|---|---|
| $Al_{0.8}Ga_{0.2}N$ | 1245 | 100 | 2.98e-5 | 4.74e-5 | 1.34e-1 | | |

| | | | | | | | |
|---|---|---|---|---|---|---|---|
| $Al_{0.75}Ga_{0.25}N$ | 1060 | 100 | 2.06e-5 | 8.28e-6 | 1.34e-1 | | |
| *n*-$Al_{0.75}Ga_{0.25}N$ | 1060 | 100 | 2.06e-5 | 8.28e-6 | 1.34e-1 | 2.49e-9 | 8.60e-5 |
| *n*-$Al_{0.6}Ga_{0.4}N$ | 1060 | 100 | 1.59e-5 | 1.08e-5 | 1.34e-1 | 2.49e-9 | 9.34e-5 |
| *i*- $Al_{0.6}Ga_{0.4}N$ | 1060 | 100 | 1.59e-5 | 1.08e-5 | 1.34e-1 | | |
| *p*- $Al_{0.6}Ga_{0.4}N$ | 1010 | 100 | 1.67e-5 | 1.21e-5 | 1.34e-1 | | |
| *p*-grading | 1010 | 100 | 1.67e-5<br>↓<br>2.69e-6 | 1.21e-5<br>↓<br>2.40e-5 | 1.34e-1 | | |
| *p*-GaN | 1010 | 100 | 0 | 2.40e-5 | 1.34e-1 | | |

| Layer | $Cp_2Mg$ (mol /min) | Mg/III | V/III | Target *x* | Target $R_g$ (nm/s) | Target thickness (nm) | Target doping concentration (/cm$^3$) |
|---|---|---|---|---|---|---|---|
| $Al_{0.8}Ga_{0.2}N$ | | | 1,735 | 0.8 | 0.2 | 200 | |
| $Al_{0.75}Ga_{0.25}N$ | | | 4,632 | 0.75 | 0.2 | 200 | |
| *n*-$Al_{0.75}Ga_{0.25}N$ | | | 4,632 | 0.75 | 0.2 | 500 | *n* ~ 5e18 |
| *n*-$Al_{0.6}Ga_{0.4}N$ | | | 5,029 | 0.6 | 0.2 | 250 | *n* ~ 5e18 |
| *i*- $Al_{0.6}Ga_{0.4}N$ | | | 5,029 | 0.6 | 0.2 | 160 | |
| *p*- $Al_{0.6}Ga_{0.4}N$ | 7.17e-7 | 2.49e-2 | 4,658 | 0.6 | 0.2 | 50 | |
| *p*-grading | 7.17e-7 | 2.49e-2<br>↓<br>2.69e-2 | 4,658<br>↓<br>5,023 | 0.6<br>↓<br>0.1 | 0.2 | 20 | *p* ~ 7e17 |
| *p*-GaN | 1.43e-6 | 5.98e-2 | 5,587 | 0 | 0.2 | 20 | |

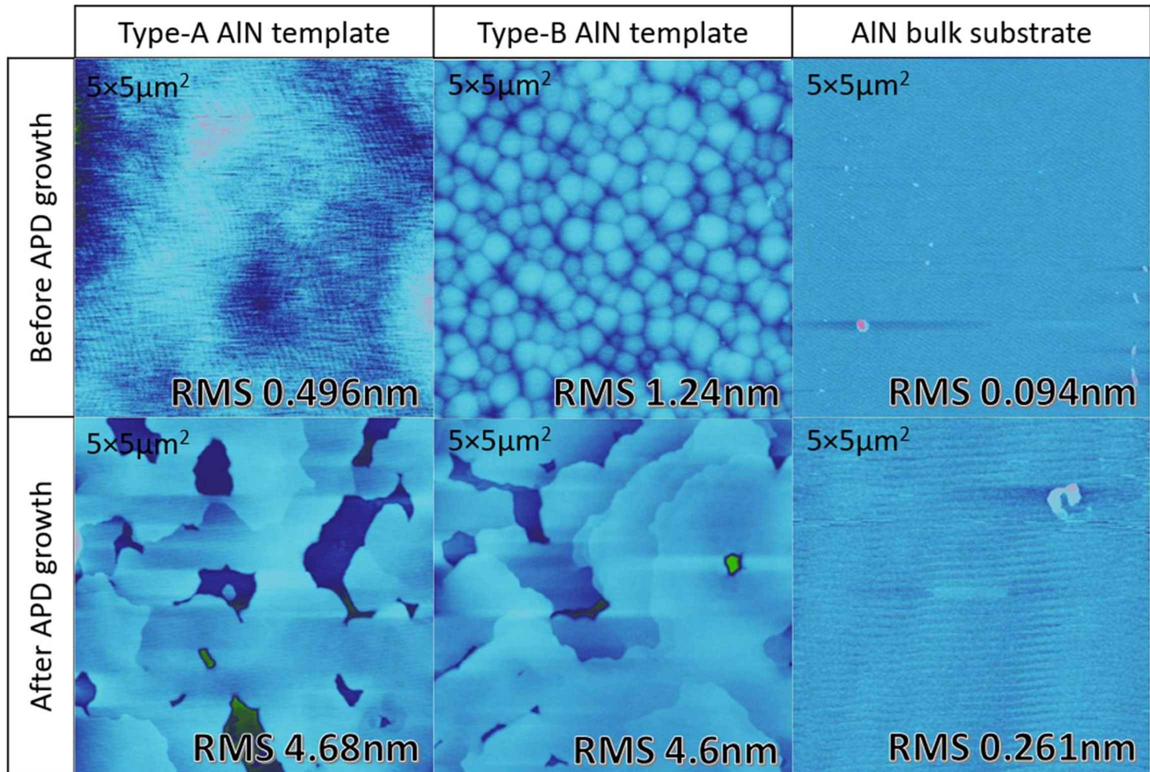


**Figure 2-17 The surface morphology measured by 5 µm x 5 µm atomic-force microscopy (AFM) scans of the Type-A, Type-B AlN templates and the AlN bulk substrate before and after the AlGaN APD growth are shown.**

## 2.6 Fabrication of deep-UV AlGaN *p-i-n* APDs

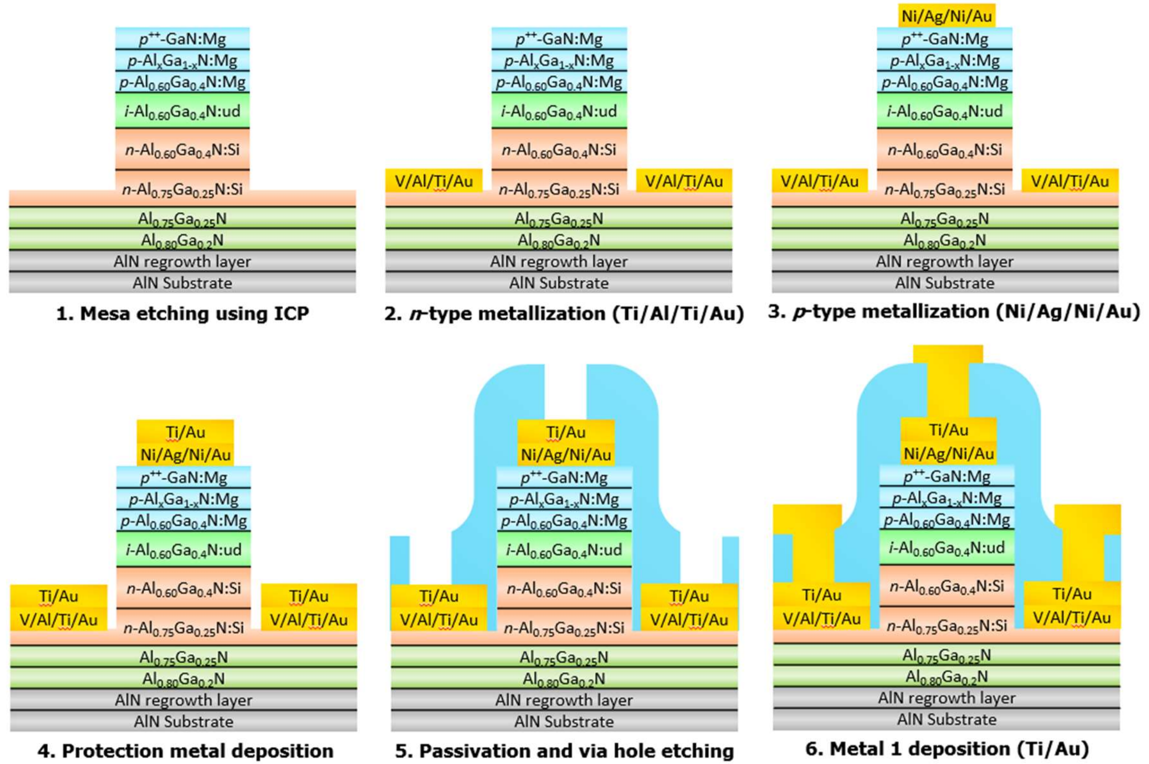


**Figure 2-18 Schematic diagram of the cross-sectional structure of the device processing steps used to fabricate AlGaN *p-i-n* APDs.**

The fabrication process front-illuminated AlGaN *p-i-n* APDs started with the e-beam evaporator deposition and lithographic patterning of a Ni metal mask to define the device areas. Reactive Ion Etching–Inductively Coupled Plasma (RIE-ICP) etching of the as-grown AlGaN heteroepitaxial structure was performed to reveal the $n$-Al$_{0.75}$Ga$_{0.25}$N layer surface. The Ni mask material was chosen owing to its superior selectivity of more than 1:100 in the ICP etching process. The RF coil and platen powers were calibrated to have good quality mesa structures without unwanted surface damage and formation of pits and hillocks. The platen power determines velocity of the etching ions, and it is the most crucial factor for optimizing the quality of the AlGaN surface due avoid excessive ion bombardment. The coil

power determines the density of the etching plasma. For the optimization studies, the RF coil power was varied from 300 to 600W, and the platen power was varied from 10W to 50W. At certain coil power, there is optimized platen power for achieving a good-quality surface (Figure 2-19). If the coil power is high enough, the acceptable platen power can be low. Since it is desired to have low ion bombardment, it is recommended to have coil power as high as possible (600W) and a low platen power (30W) so that the pits and hillocks are minimized.

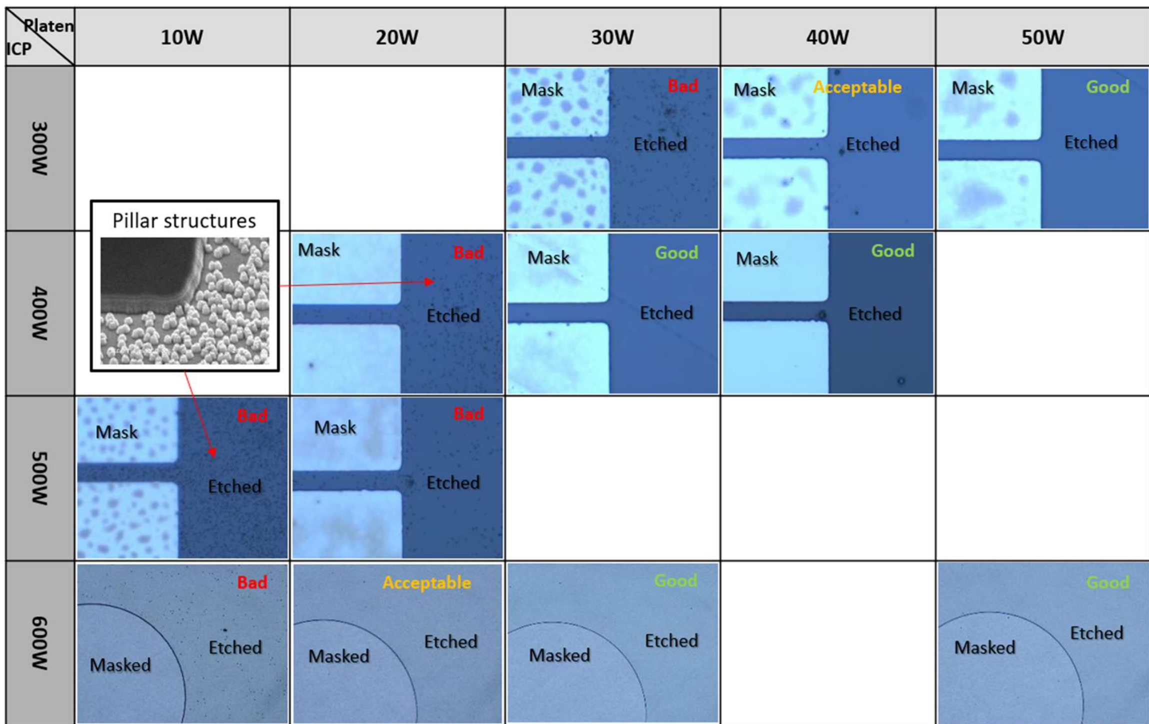


**Figure 2-19 Table of photographs of the etched $Al_xGa_{1-x}N$ $x$ = 0.6 surfaces with the ICP coil power varying from 300W to 600W, and the platen power varying from 10W to 50W is shown. If the platen power is too low for a certain coil power, pits and hillocks are formed on the surface.**

The gases used in the RIE-ICP etching were $BCl_3$, $Cl_2$, and He, and the flow rates were 5/45/32.5 sccm, respectively. Without $BCl_3$, a native oxide of the AlGaN will remain during

the etching, and this will result in making the AlGaN surface rough [70]. The $BCl_3$ and total chlorine-based gas flow rate ratio ($BCl_3/(BCl_3+Cl_2)$) was chosen as 10% to give the highest etch rate [71]. Helium gas was chosen as the carrier gas instead of argon to reduce the ion-bombardment damage owing to He having a smaller atomic mass [72]. The overall etch rate was 2nm/s.

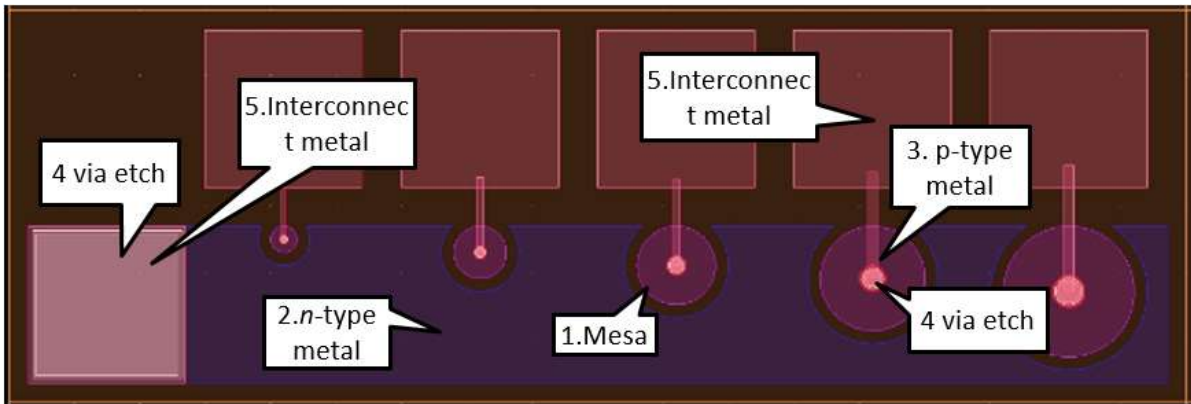


**Figure 2-20 The ADS mask file for each layer is shown with different circular mesa diameters ranging from 20 to 100µm**

After ICP mesa etching, the Ni mask was removed with nitric acid and the samples were spin-coated with a lift-off photoresist (positive S1813 photoresist) and patterned with Heidelberg MLA150 mask-less aligner (Figure 2-20). Vanadium based *n*-type metal stacks (V/Al/Ti/Au) [73] were deposited on the *n*-type surface by an electron-beam evaporator. The thicknesses of the *n*-type Ohmic contact metal stack layers were 300/500/300/500 Å, and the deposition rate was 2 Å/s for all metals, a low enough rate so that the e-beam deposition did not to heat up the APD samples. The *n*-type contact annealing process was performed at 700ºC in a nitrogen ambient. Nickel-based *p*-type metal stacks (Ni/Ag/Ni/Au) were deposited, with thickness of 25/500/300/500 Å. The *p*-type metal stacks were annealed at 475 ºC in a compressed dry air ambient.

Next, a Plasma Enhanced Chemical Vapor Deposition (PECVD) $SiO_2$ passivation layer was deposited conformally on the wafer surface. The main purpose of this passivation layer is to prevent the premature device breakdown under high reverse bias, and to reduce the leakage current [74]. Then via holes for the *n*-type and the *p*-type metals were created by additional photolithography and RIE etching. Finally, thick Ti/Au metal pads were deposited by e-beam evaporation to connect to the *n*-type and the *p*-type metal regions for wire-bonding (Figure 2-21).

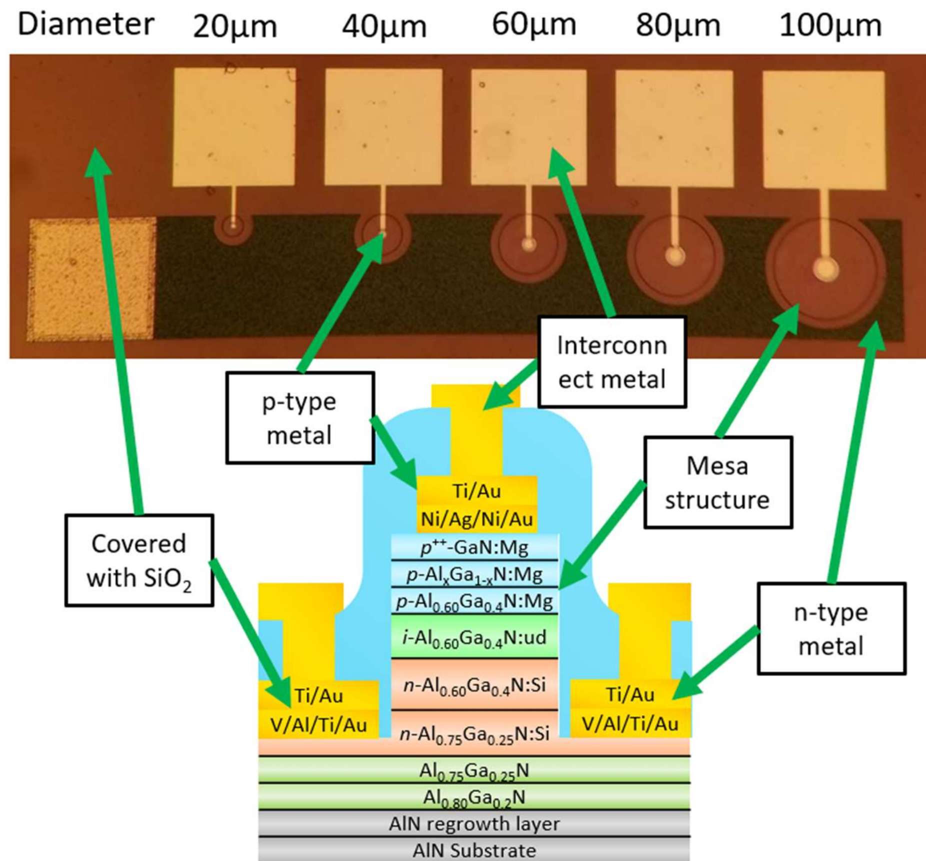


**Figure 2-21 Microscope image of a completed AlGaN APD structure grown on a AlN bulk substrate. The correspondence of each region with an APD device schematic diagram is shown.**

## 2.7 Characterization of deep-UV AlGaN *p-i-n* APDs

The dark current densities of the AlGaN DUV APDs from different substrates were characterized (Figure 2-22). Every measured APD device in this study had a fixed circular dimension of 20 μm in diameter. The dark current density of the AlGaN APDs grown on the AlN bulk substrate had the lowest leakage current compared to that of the devices grown on the AlN/sapphire templates. The AlGaN APDs grown on bulk AlN substrates had a dark current density below ~ $1 \times 10^{-8}$ A/cm$^2$ up to a reverse bias of -40 V, and reverse-bias breakdown voltage around -140 V. By comparing the dark current densities of AlGaN DUV APDs from grown on different AlN templates (Type-A, Type-B), the APD devices on the Type-B AlN template have a lower leakage current than the APD devices on the Type-A AlN template. The APD devices grown on the Type-B template had leakage current densities of ~ $1 \times 10^{-5}$ A/cm$^2$ at a reverse bias of -40V, and the devices grown on the Type-A template had leakage current density of ~ $5 \times 10^{-5}$ A/cm$^2$ which is higher than the APD devices grown on the Type-B templates. In the previous section, it was discussed that the AlN bulk substrate has the lowest dislocation density, and the Type-A AlN template has the highest dislocation density. Since the leakage current density is strongly related to the dislocation density of the device, it is obvious that the substrate with lower dislocation density will produce the APD device with lower leakage current density.

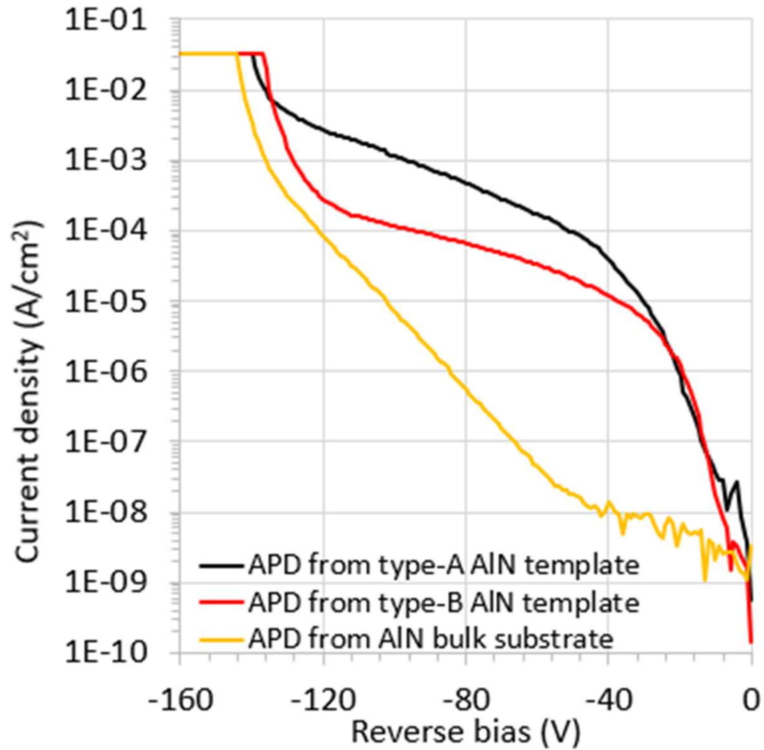


**Figure 2-22 The dark current density vs. reverse bias of AlGaN APDs fabricated on different substrates. The circular diameters of the measured APD devices are 20μm. The black line is the dark current density from an APD on Type-A AlN template, the red line is from an APD on Type-B AlN template, and the yellow line is from an APD on the AlN bulk substrate. Notice that the dark current density from the APD on the AlN bulk substrate is the lowest.**

The UV photocurrent response of the AlGaN APD devices fabricated on the AlN bulk substrate was measured, and the gain was calculated (Figure 2-23). For these measurements, the device was illuminated with 250 nm UV light from a Xe lamp source coupled to a monochromator for wavelength selection. The APD device had a circular dimension of 20 μm in diameter. The measured photocurrent density was around $4 \times 10^{-7}$ A/cm$^2$ up to the reverse bias of -30 V. Then the photocurrent density increases gradually as the reverse bias increases from -30 V to -140 V. Similar to the dark current density, there is an abrupt increase in the photocurrent density around the reverse bias of -140 V, which shows the breakdown behavior.

The maximum calculated gain of the AlGaN APD device from the AlN bulk substrate is $1.63\times10^{4}$ at the reverse bias of -145 V.

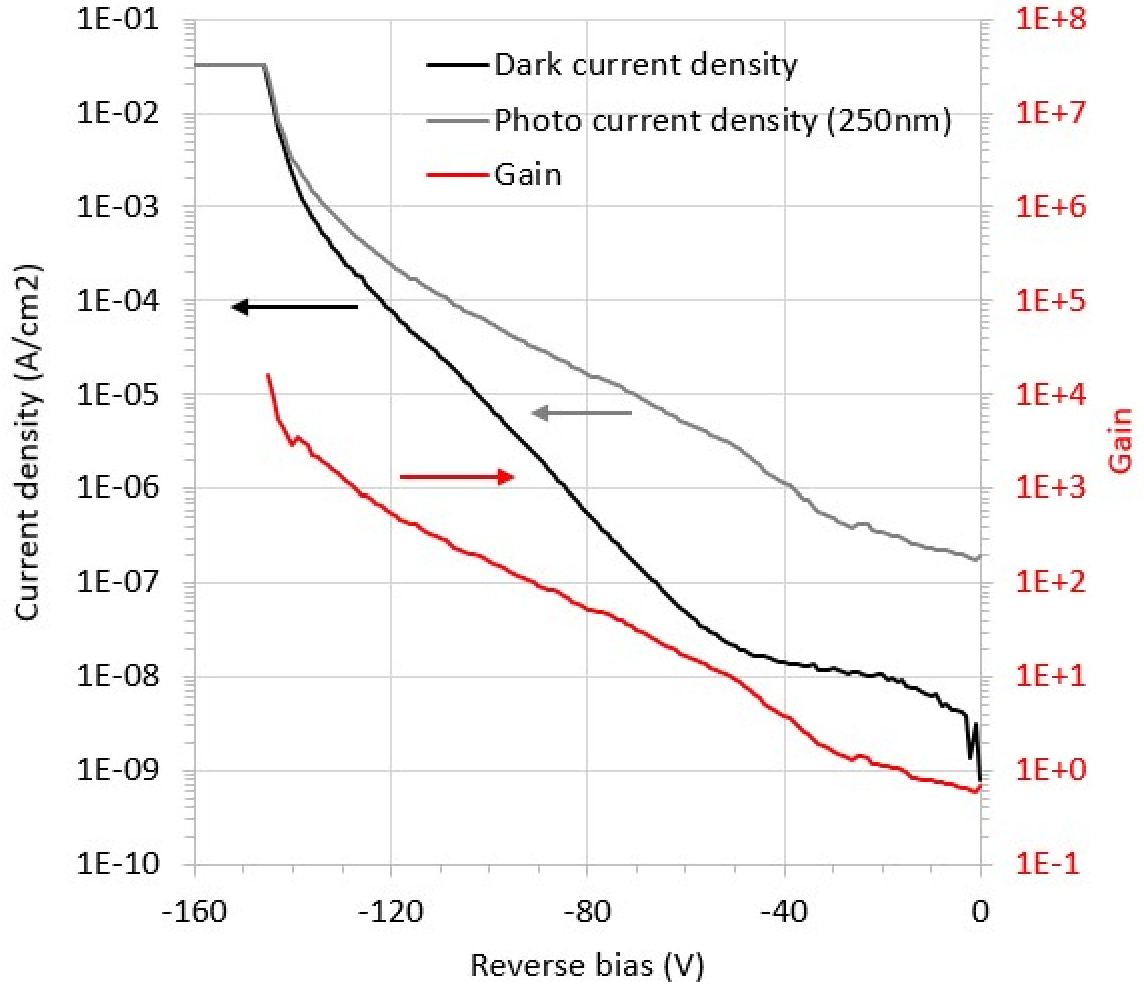


**Figure 2-23 Dark and photocurrent density of the 20 µm diameter AlGaN APD fabricated on the AlN bulk substrate are shown, using 250 nm UV light from a Xe lamp and the monochromator. The optical gain is also calculated.**

The calibrated photoresponse of the AlGaN APDs fabricated from different substrates were measured. At zero bias, the average photoresponse measured at the wavelength of 250 nm are 58.86 ± 2.77 mA/W for the AlGaN APDs on the Type-A AlN template, 59.87 ± 2.06 mA/W for the AlGaN APDs on the Type-B AlN template, and 71.45 ± 2.87 mA/W for the AlGaN APDs on the AlN bulk substrate. In this experiment, the APD device dimensions are circular with a diameter of 100 μm.

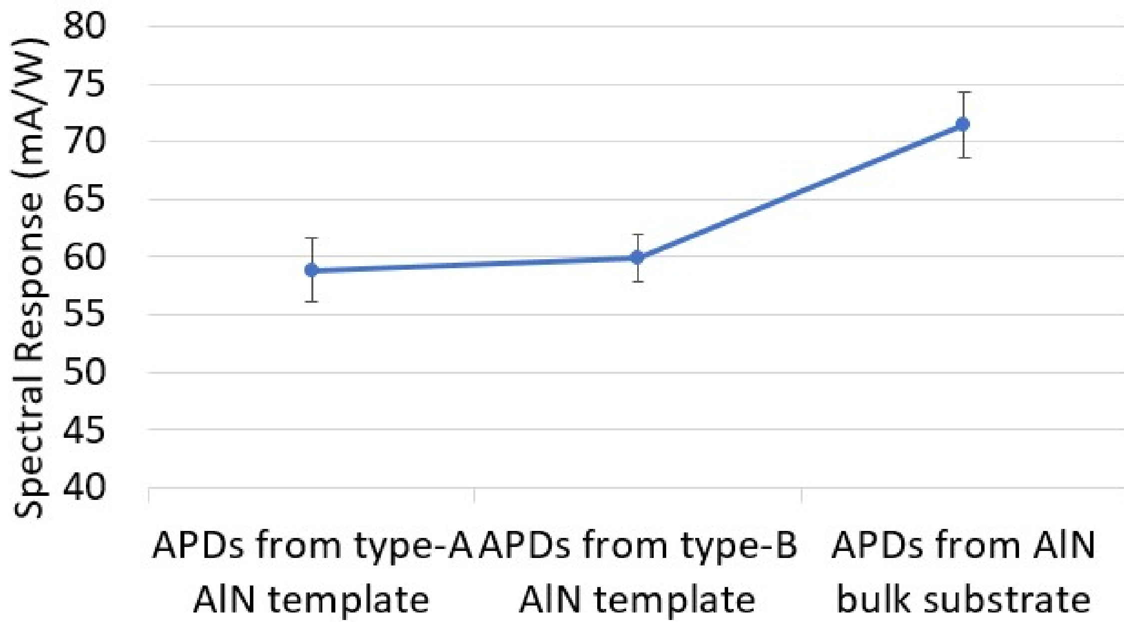


**Figure 2-24 Average photoresponse at 250 nm, and zero bias for the 100 µm dia. AlGaN APD devices from the Type-A, Type-B AlN templates and the AlN bulk substrate were measured.**

To understand whether the breakdown behavior is attributed to an avalanching or a tunneling mechanism (or possibly both), the temperature coefficients of the breakdown voltage of the AlGaN APDs with different substrates were measured. If the temperature coefficient of breakdown voltage is positive, then the avalanching contributes and controls the breakdown, whereas if the coefficient is negative, then the tunneling contributes and controls the breakdown [75]. The temperature coefficient is determined by measuring the breakdown voltages at five different temperature set points, from 25°C to 45°C by steps of 5°C and calculating the slope. Average coefficients and errors were calculated and plotted (Figure 2-25) from five different AlGaN DUV APDs at five different locations within each substrate measured. The devices have the circular dimension of 20 µm in diameter. The APDs on the AlN bulk substrate have the largest average temperature coefficient of breakdown

voltage which is -0.086 ± 0.009 V/K. The average coefficient of the APDs on Type-B AlN template is -0.093 ± 0.014 V/K which is slightly smaller than that of the APDs on the AlN bulk substrate. The average coefficient of the APDs on Type-A AlN template is -0.12 ± 0.024 V/K, and the values are the smallest and most spread out. From the above analysis, the dislocation density of a substrate (either AlN bulk substrate or AlN template) should be substantially minimized in order to reduce the dark current contribution from the tunneling breakdown, and to increase the contribution from the avalanche breakdown mechanisms.

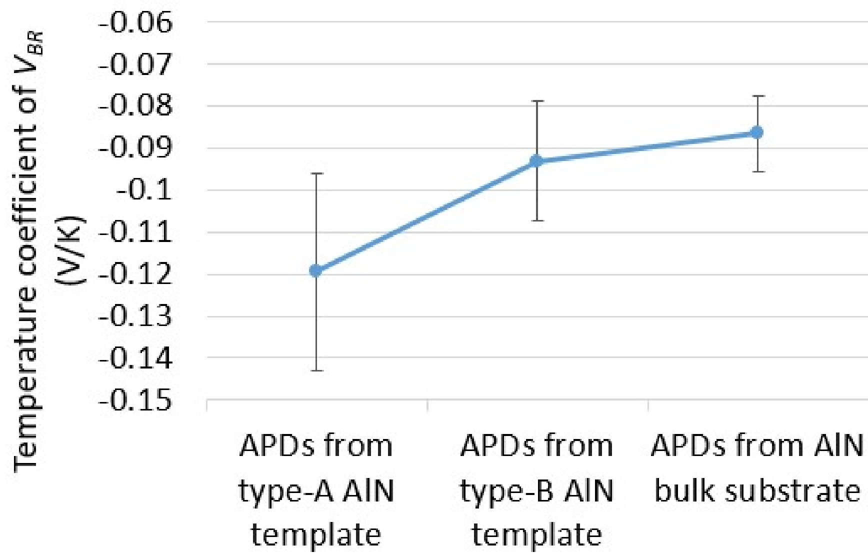


**Figure 2-25 The temperature coefficients of the reverse-bias breakdown voltage of the AlGaN APDs from different substrates are shown with error bars. The devices have a circular dimension of 20 μm diameter.**

## 2.8 Summary

In this project, we have demonstrated a top-illuminated $Al_{0.6}Ga_{0.4}N$ DUV *p-i-n* APD structure grown on the AlN bulk substrate and two types of AlN/sapphire templates. The APD structure was designed to minimize strain from each layer by introducing step-grading transition layers. The dark current showed a distinctive breakdown behavior which the slope of the *I-V* curve increases abruptly around the reverse bias of ~-140V. The AlGaN APD fabricated on the AlN bulk substrate has the lowest leakage current density around $1\times10^{-8}$ A/cm$^2$. From the same device, the maximum (current-limited) optical gain of $1.63\times10^4$ was achieved at a wavelength of 250 nm and the reverse bias of ~-145V. At zero bias, the average photoresponse was 71.45 ± 2.87 mA/W at the wavelength of 250 nm for the APD from the AlN bulk substrate. Although the temperature coefficients of breakdown voltage were calculated to be negative for all three substrates, it was observed that the coefficients were increasing in absolute magnitude as the dislocation density of substrate was reduced. This effect could be due to a trade-off between avalanche and tunneling photocurrent contributions.

# CHAPTER 3. LOW-TEMPERATURE GEIGER-MODE MEASUREMENTS OF GALLIUM NITRIDE AVALANCHE PHOTODIODES

## 3.1 Introduction

In this project, the principle of single-photon detection using APDs is studied, and a low-temperature Geiger-mode measurement system was designed and built by integrating a device driver circuit, a UV-illumination system, and a device temperature-control system operating below room-temperature. The GaN *p-i-n* APD devices were previously grown and fabricated at Georgia Tech by Dr. Mi-Hee Ji. We measured breakdown voltage, dark count rate and photon detection efficiency of the GaN APD devices over a temperature range from -40 to 20 $^{o}$C. From the dark count rate vs. temperature results, we analyzed the dark count mechanisms of the GaN APDs.

## 3.2 Sample structure

The structure of the GaN *p-i-n* APDs used is described in Figure 3-1. [76] (Credit to Dr. Ji.) The substrate is a c-plane Hitachi Cable free-standing (FS) GaN or an Ammono bulk GaN wafer. The epitaxial growth starts with a 0.6 μm layer of unintentionally doped GaN buffer layer, followed by a 2.3 μm thick Si-doped GaN *n*-layer with a free-electron concentration of $4\times10^{18}$ cm$^{-3}$. An unintentionally doped GaN *i*-layer of 280nm thickness is grown on top of the *n*-layer, with a background Si doping of $2\times10^{16}$ cm$^{-3}$. The *p*-layer consists of two separate

layers: the first is a 100 nm-thick Mg-doped GaN and the second is a 15 nm-thick highly Mg-doped GaN cap layer. The Mg-doped *p*-layer has a free-hole concentration of ~$1\times10^{18}$ cm$^{-3}$, as measured by Hall-effect studies and highly Mg-doped *p*-layer has a Mg atomic concentration of ~$1\times10^{20}$ cm$^{-3}$ as measured by secondary ion mass spectrometry (SIMS).

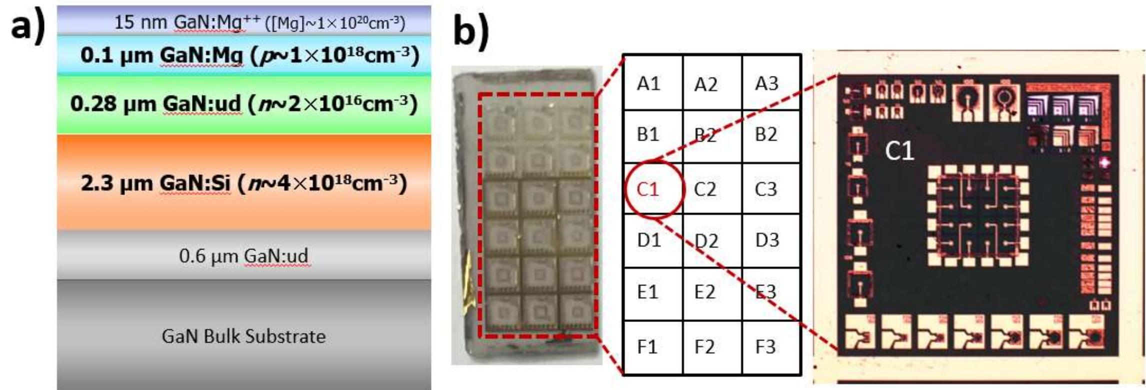


**Figure 3-1 a) Schematic diagram of the cross-sectional structure of GaN *p-i-n* APD grown on bulk GaN substrates. b) Microscopic images of a fabricated GaN APD sample (Credit to Dr. Mi-Hee Ji.)**

The first step of the device fabrication process is mesa etching. The etching process is done in a Plasma-Therm inductively coupled plasma (ICP) etching system, and the etching gas is BCl/$Cl_2$/Ar mixture. The ICP process etches down to the *n*-type epitaxial layer of the device structure. The second processing step is to deposit the *n*-type metal contact in the region of the exposed ICP-etched surface of the sample. The *n*-type metal ohmic contact structure is an e-beam evaporated Ti/Al/Ti/Au stack. Once the *n*-type metal is deposited and patterned, the sample is annealed with a rapid thermal annealing (RTA) system to create the ohmic contact (nitrogen ambient, 700 °C, 1 min). In similar way, the *p*-type metal is deposited in a photolithographically defined region on the top surface of the sample after the *n*-type metal deposition and annealing. The structure of the metal contact for the *p*-type ohmic

contact is e-beam evaporated Ni/Ag/Ni/Au, and another RTA process was performed to form the *p*-type ohmic contact (compressed dry air, 500 °C, 1 min). The whole surface of the sample is passivated with a silicon oxide layer by using plasma-enhanced chemical vapor deposition (PECVD), and reactive-ion etching (RIE) or ICP etching is performed to open these via holes for $p$-type and $n$-type contact metal. The last step is to deposit thick metal pads for probing and wire-bonding. The fabricated device has dark current density of $6 \times 10^{-7} A/cm^2$ at $V_R = 48V$, breakdown voltage of $-96 \pm 0.5V$, multiplication gain higher than $5 \times 10^4$, and spectral responsivity is $5{,}485 mA/W$ at $\lambda = 378nm$ at $V_{BR} = -95$.

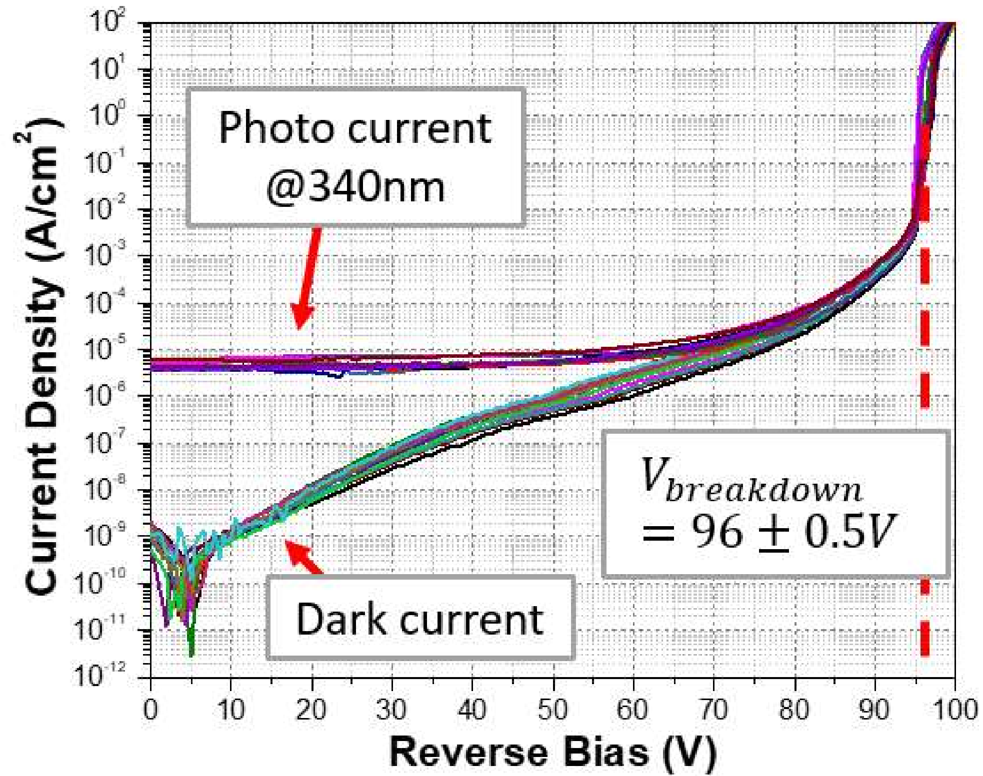


**Figure 3-2 The reverse bias I-V characteristics of the GaN p-i-n APD array devices with a mesa size of 75×75 μm2 under dark condition and UV illumination with a peak wavelength of $\lambda = 340nm$**

## 3.3 Theory of photon counting

In a single-photon-detection measurement, one measures number of photons counted per unit of time in units of counts/s. Besides the photon count rate, there are two important parameters. One is the dark-count rate (DCR), which is number of counts without incident light. It is measured in units of counts/s and is treated just like noise. The other parameter is photon detection efficiency (PDE), which is number of photons received (i.e., detected) per number of photons illuminated.

### *3.3.1 Quenching circuit*

In the single-photon detection process, a large reverse bias is applied to the APD. When the large reverse bias is greater than the breakdown voltage of the APD and when one photon is incident on the APD and it is absorbed, an avalanche current flows through the APD with a certain probability. The avalanche current keeps flowing as long as there is a large electric field above the breakdown field.  In order to detect another single photon, the avalanche current should stop flowing, by reducing the reverse bias. Once the avalanche current stops flowing, or quenches, the reverse bias is applied to the APD is increased again, ready for detecting another photon [77]. To enable above operation, special type of circuit is needed, and is typically referred as quenching circuit.

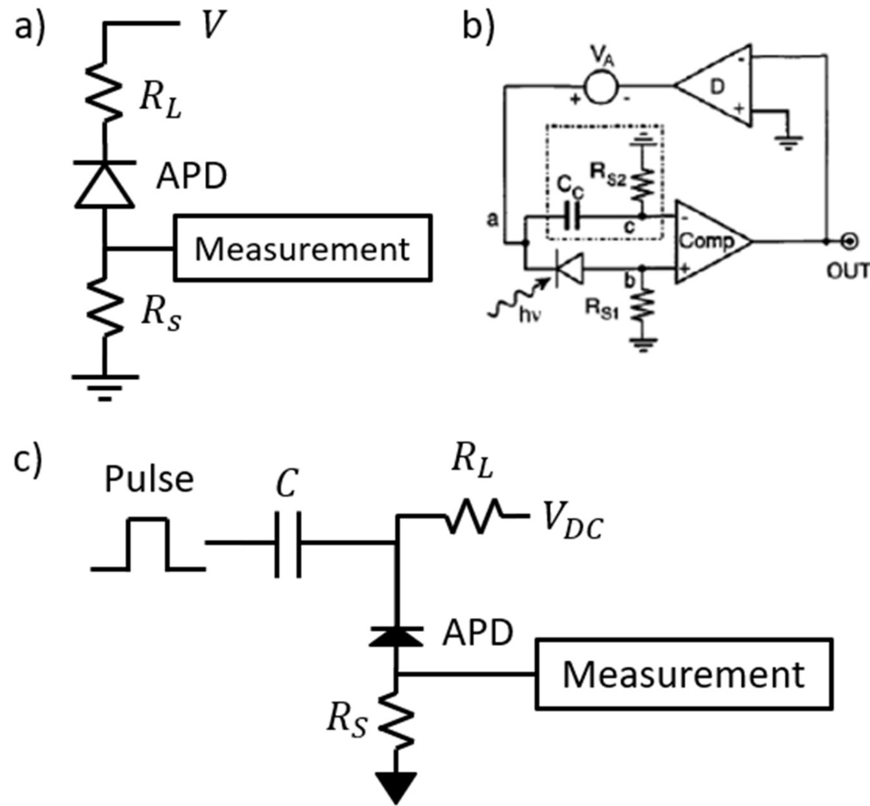


**Figure 3-3 a) passive quenching circuit, b) active quenching circuit [77], c) gated quenching circuit**

There are several configurations of quenching circuits. A passive quenching circuit (Figure 3-3a) is the simplest quenching circuit and consists of the APD with high ballast load resistor connected in series [78-80]. When the total applied reverse bias voltage to the APD with the resistor is below breakdown, the current is insignificantly small and there is an insignificant voltage drop across the resistor. However, when the total applied voltage is above the breakdown voltage, and a photon is absorbed, a large avalanche current flows, but the voltage drop across the ballast resistor is also large, so the current is quenched. The passive quenching circuit has the simplest configuration but it limits maximum possible count rate by

$RC$ time constant, where $R$ is a quenching resistor and $C$ is combined capacitance of an APD and other parasitic capacitances.

The other configuration of the quenching circuit is an active quenching circuit [81-83] (Figure 3-3b). In this configuration, active elements such as operational amplifiers (op-amps) are used, which sense the rise of the avalanche current and immediately quenches the current [84]. Compared to the passive quenching circuit, the quenching time is well defined, but it requires a somewhat complex circuit. There is another type of configuration called mixed passive-active quenching [81, 85-87]. Since the quenching and the restoring do not have to be both active, this configuration simplifies the circuit by replacing either part with passive element.

The last configuration is called the gated quenching circuit (Figure 3-3c), and this configuration operates an APD under the control of a rectangular voltage pulse [77, 82, 88, 89]. This configuration is the most widely used configuration, which has a simple circuit and well-defined quenching time. In this configuration, a pulse generator is connected in series with a capacitor, and a DC power supply is connected in series with a load resistor. The pulse generator + capacitor and the DC power supply + resistor are connected to the APD in parallel, and the APD is connected to a measurement unit such as an oscilloscope. The total applied voltage is equal to sum of the pulse signal and the DC bias. The gated circuit operation configuration has two major advantages. First, they are suited for a pulse with a short duration, with the advantage that the short duty cycle sufficiently suppresses trapping effects. Second, the avalanche triggering occurs without the interference of the previous photon-generated pulse. These advantages make this configuration the most practical in most Geiger-mode APD applications.

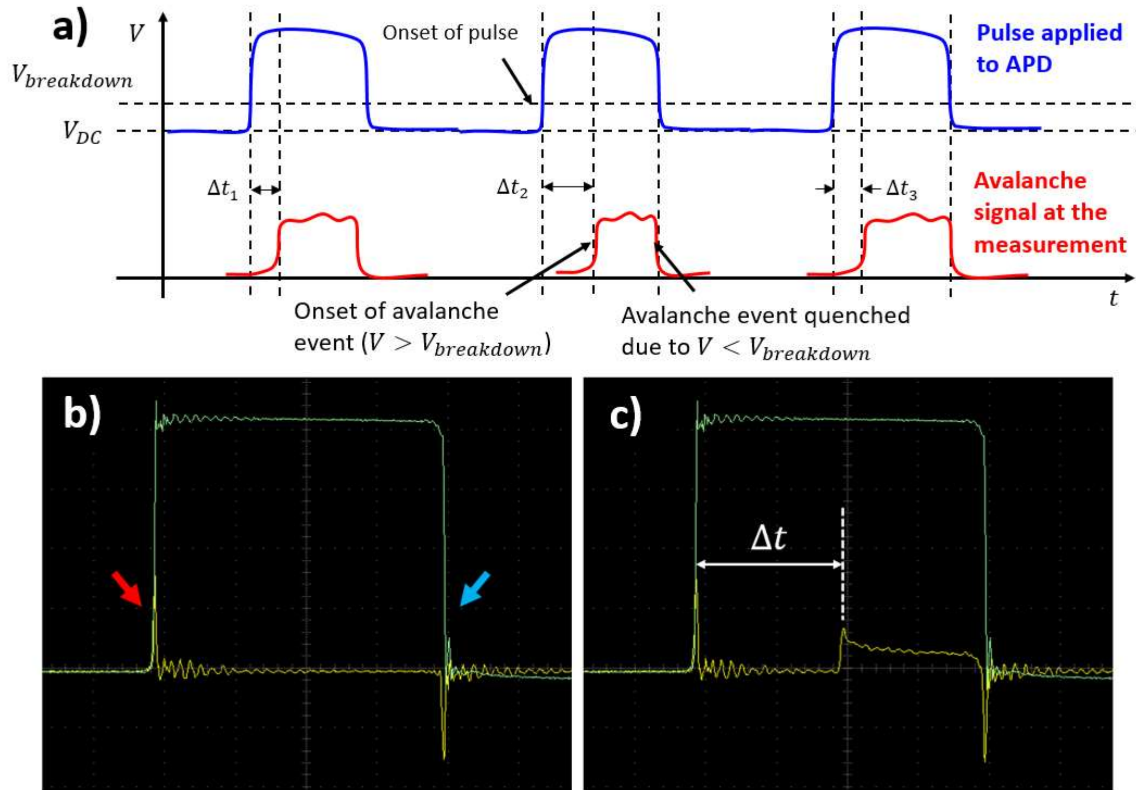


**Figure 3-4 a) The rectangular pulse signal applied to the APD, and the avalanche signal captured with a measurement unit. Notice that there is delay *Δt_i* between onset of the pulse signal to the onset of the avalanche signal. b) When the pulse + DC voltage is below breakdown there is no avalanche event. c) When the pulse + DC voltage is above breakdown, some time $\Delta t$ after rising edge (red arrow in b) avalanche event will occur. The spike at the rising and falling edge (blue arrow in b) is due to inherent capacitor in the oscilloscope.**

In the operation of the gated quenching circuit, the (negative bias) rectangular pulse + DC voltage bias (negative bias) is applied. The magnitude of the DC voltage should be slightly below the breakdown voltage of the APD, and the rectangular pulse is added so that the APD is biased above breakdown during the pulse period. When the pulse voltage is zero, the APD

is quenched. When the pulse voltage is not zero, and if there is light incident on the surface of the APD, then the rectangular pulse triggers the operation of the APD into avalanche breakdown, but it takes some time within the pulse to trigger an avalanche current. The avalanche current keeps its level until the falling edge of the input pulse and the GaN APD avalanche breakdown is quenched (Figure 3-4). Then, there must be a time interval ($\Delta t$) between the rising edge of the pulse signal and onset of an avalanche event, and this time interval is random for each pulse.

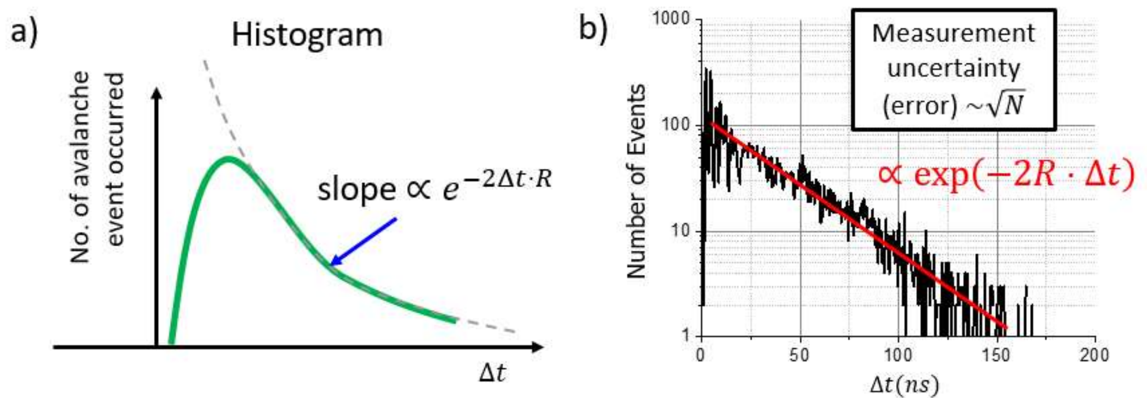


**Figure 3-5 a) Histogram of number of avalanche events occurred for certain $\Delta t_i$. The slope can be fitted with the function proportional to exp(-2$\Delta t \cdot R$) to get the count rate *R*. b) In the real device example, the count rate is easily obtained by fitting with a semi-logarithmic scale.**

Using the oscilloscope, 10,000 pulse events are recorded, thus 10,000 time-intervals ($\Delta t$). When collecting the data, the threshold level of triggering the avalanche event must be higher than the RMS noise (in this case ~20 mV). The digital oscilloscope sends this data to a computer, and the computer processes this randomly distributed data into one histogram, a

graph of number (occurrence) of certain $\Delta t$ vs. $\Delta t$. (Figure 3-5a) The histogram of $\Delta t$ follows a Poisson distribution which decays exponentially in $\Delta t$, and it is possible to fit the semilogarithmic plot of the data with a function proportional to exp ($-2R\cdot\Delta t$). From this function fitting, one can obtain the generalized count rate $R$. If the count rate is calculated from the histogram without any light when measured, the count rate is the dark-count rate, and if count rate is calculated from the histogram with the light when measured, the count rate is the total dark + photon count rate.

### *3.3.2 Mathematics of single-photon detection*

To understand why Poisson statistics are used in the photon counting, first the measurement is defined by counting the number of successful events (the avalanche events) resulting from given number of trials (number of the bias pulses applied). Each trial is a binary process in that either success or no success, with a success probability of $p$. For our case, when the junction is charged (i.e., when the reverse breakdown voltage is applied), there is the probability $p$ of avalanching by an incident photon. This process can be statistically modeled, which is called binomial distribution and written as [90]

$$P(x) = \frac{n!}{(n-x)!\,x!} p^x (1-p)^{n-x}, \tag{22}$$

where $x$ is the number of successful events from $n$ number of trials, $p$ is the success probability. The average number of successes $\lambda$ is defined as mean value of $x$, and following relationship is possible.

$$\bar{x} = \lambda = pn, \tag{23}$$

When the probability of the success $p$ (physical property) is small, if $n$ is chosen to be a large number (i.e., a large set of experimental data is used), we can write the binomial distribution in terms of the average number of successes, $\lambda$, and the binomial distribution converges to the Poisson distribution [91].

$$\lambda = pn \rightarrow p = \frac{\lambda}{n} \tag{24}$$

$$\lim_{n\rightarrow\infty} P(x) = \lim_{n\rightarrow\infty} \frac{n!}{(n-x)!\,x!}\left(\frac{\lambda}{n}\right)^{x}\left(1-\frac{\lambda}{n}\right)^{n-x} = \frac{\lambda^{x}}{x!}e^{-\lambda} = \frac{(pn)^{x}}{x!}e^{-pn} \tag{25}$$

Thus the Poisson distribution is a direct mathematical simplification of the binomial distribution under the conditions that the number of trials, $n$, is large, and the success probability, $p$, is small and constant.

The Poisson distribution is used to model a series of random and independent events with known average rate (number of events per period of time). Then the average number of avalanche successes, $\lambda$, is defined as the multiplication of an average number of successes per unit time, $r$, times a time interval, $t$.

$$\lambda = pn = rt \tag{26}$$

The probability distribution with the average success (avalanche) rate $r$ for the $x$ number of successful events (avalanche events) is obtained.

$$P(x) = \frac{(rt)^x}{x!} e^{-rt} \tag{27}$$

The above relation shows the probability with the avalanche occurring $x$ events, or how many photons detected within certain time interval $t$.

The Poisson distribution can be applied to certain situations. The probability of having at least one avalanche event within a time interval, i.e., the sum of all the probabilities with $x > 0$, is expressed by the relationship below.

$$P(x > 0) = \sum_{x=1}^{\infty} P(x, t) = e^{-rt} \left[ \frac{(rt)^1}{1!} + \frac{(rt)^2}{2!} + \cdots \right] = 1 - e^{-rt} \tag{28}$$

Consider the case where no light is incident on the APD. The probability $P(x > 0)$ is treated as a dark-count probability $P_d$, $r$ as a DCR, $t$ as a time interval, or a pulse width $\tau$.

Also, the probability $P(x > 0)$ can be simply written as number of avalanches over the total number of measured events. This is called the short-pulse method and requires a nanoscale pulse width for accurate measurement. (As a rule of thumb, the pulse width should be 10% of $1/DCR$).

$$P_d = \frac{N_{avalanche}}{N_{total}} = 1 - e^{-DCR \cdot \tau} \tag{29}$$

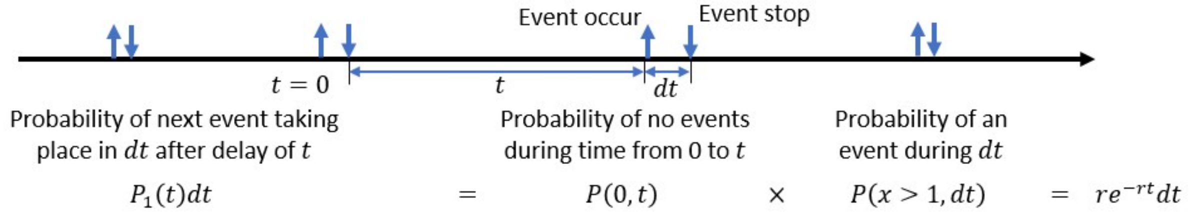


**Figure 3-6 Schematic diagram of the application of Poisson distribution, which is called interval between successive events.**

Instead of calculating all the probabilities of having at least one successful avalanche, we fully evaluated the situation for gated-mode operation. To begin with, if we assume a probability distribution that the avalanche event takes place within a differential time $dt$ after the time interval of length $t$ (Figure 3-6), then the probability is

$$P_1(t)dt = P(x = 0, t) \times P(x > 1, dt) \tag{30}$$

Since $P(x = 0, t)$ is the probability of no events during the time from 0 to *t* (Figure 3-6), it should be

$$P(x = 0, t) = e^{-rt} \frac{(rt)^0}{0!} = e^{-rt} \tag{31}$$

The $P(x > 1, dt)$ is the probability of having at least one event during *dt*,

$$P(x > 1, dt) = \sum_{x=1}^{\infty} P(x, dt) = e^{-rdt}(e^{rdt} - 1) = 1 - e^{-rdt} \cong rdt \tag{32}$$

where the Taylor approximation is used. Putting together the equation (31) and (32) into the equation (30) we get

$$P_1(t) = re^{-rt} \tag{33}$$

From the above relation, the rate can be obtained by calculating the average interval length $\bar{t}$

$$\bar{t} = \frac{\int tI_1 dt}{\int I_1 dt} = \frac{\int tre^{-rt} dt}{1} = \frac{1}{r} \tag{34}$$

and the rate can be obtained from the average interval length.

$$r = \frac{1}{\bar{t}} \tag{35}$$

This situation is called interval between successive events. [90]

However, in reality, it is impossible to acknowledge where the avalanche event ends even though the avalanche events are stopped after the pulse period. Thus the starting point is always random in time. In this case, the probability is weighted by the factor proportional to their length $\frac{t}{\bar{t}} = rt$ [90].

$$P_s(t) = rtP_1(t) = r^2 te^{-rt} \tag{36}$$

Then the average time interval ( $\overline{t_s}$) is doubled from previous value ( $\bar{t}$).

$$\overline{t_s} = \frac{\int tP_s dt}{\int P_s dt} = \frac{1}{r_s} = 2\bar{t} = \frac{2}{r} \tag{37}$$

The effective average avalanche rate $r_S$ is half of the rate obtained from the interval between successive events case ($r$). It also can be calculated from fitting the probability distribution with the function proportional to $\exp(-2r_s \cdot \Delta t)$ [90], and this is called the $\Delta t$ method. If the avalanche rate was measured without the light, it is called dark-count rate (DCR) and with the light, it is called photon-count rate.

Besides the avalanche rate, or count rate $r$, another important feature in photon counting is photon detection efficiency (PDE). To measure the PDE, a reference photon counter is required. In this research, a commercial Si photon counter (Hamamatsu SPPC C11202) was used. Then from the single stable light source, both the GaN APD and the Si photon counter were illuminated using a beam splitter or a bifurcated fiber. Once the intensity ratio between the light illuminating on the GaN APD and the Si photon counter was obtained, the PDE of the GaN APD was calculated as

$$PDE_{GaN} \cdot \frac{A_{GaN}}{r_{GaN}} = PDE_{Si} \cdot \frac{A_{Si}}{r_{Si}} \tag{38}$$

The $PDE_{si}$ is the PDE of the Si photon counter at certain wavelength, $A_i$ is photoactive area of the GaN APD or the Si photon counter, and $r_i$ is photon count rate from the GaN APD or the Si photon counter.

### *3.3.3 Validity of the Δt method*

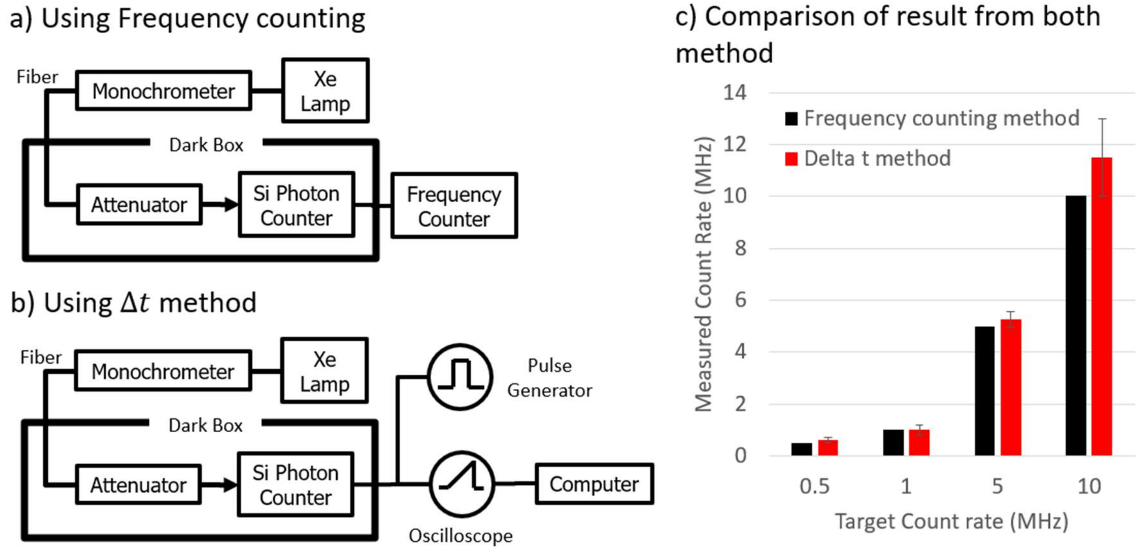


**Figure 3-7 Schematic diagram comparison of two methods of count rate measurement a) using a frequency counter, b) using the $\Delta t$ method c) and the measurement results, which shows that the data are similar to each other within the error.**

To verify the validity of the $\Delta t$ method, two sets of experiments were performed with the Si photon counter. (Figure 3-7) In one experiment, the Si photon counter is connected to a frequency counter for measuring the photon count rate. Since the Si photon counter emits number of rectangular pulse signals proportional to the number of photons detected, only a frequency counter is needed to measure the count rate. In the second experiment the Si photon counter and pulse generator are connected to an oscilloscope to measure the time differences between the onset of the bias pulse and the onset of the avalanche signal, and the photon count rate is measured from fitting the function to the histogram. For both experiments, the light source is a Xe lamp, and the monochrometer is inserted to select a certain wavelength. The results from both measurements match within their uncertainties.

### 3.4 Geiger-mode measurement system

The complete experimental setup for Geiger-mode measurement is the integration of three hardware systems and a software program for controlling the hardware equipment.

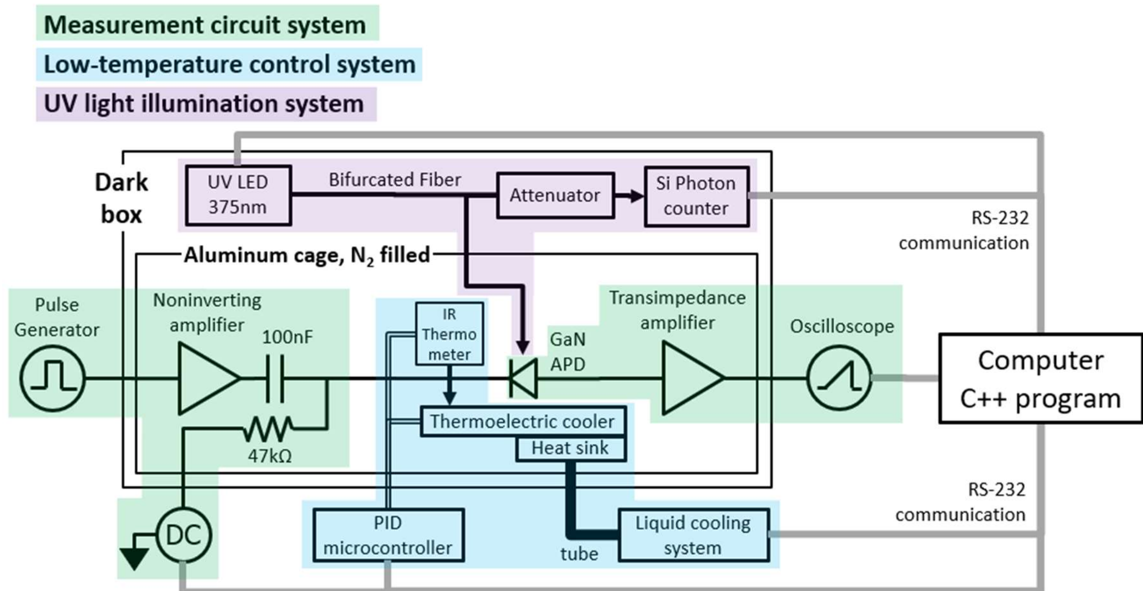


**Figure 3-8 Schematic diagram of a Geiger-mode measurement setup, consisting of a UV-illumination system (shaded in violet), a measurement circuit (shaded in green), and a low-temperature control system (shaded in blue). All the equipment in the hardware systems are connected to the computer, controlled by C++ program.**

### *3.4.1 Measurement circuit system*

The circuit system development started with a simple gated quenching circuit, and active elements such as op-amps are inserted before and after the APD. The 1st stage op-amp is a buffer amplifier with gain of 2, which isolates a pulse generator (Agilent 33522A Wavefunction generator), and the 2nd stage op-amp is a transimpedance amplifier. The op-amps are inserted in order to isolate the APD signal from the signal reflectance [92], and

keeping the avalanche signal as clean as possible. After the transimpedance amplifier, the oscilloscope (PSI DRS4) measures the time-dependent current of the APD.

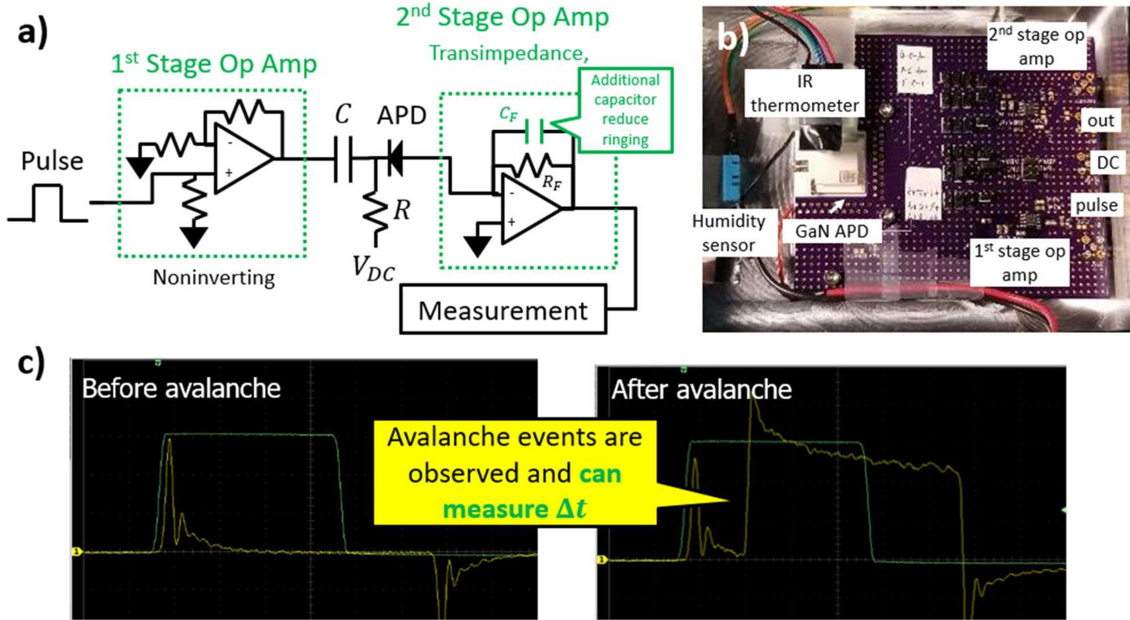


**Figure 3-9 a) Schematic circuit diagram consisting of gated quenching circuit, two op-amps (noninverting and transimpedance) and measurement unit. b) photograph of PCB board of the quenching circuit, with GaN APD connected to the PCB board with wire-bonding. c) Oscilloscope graph showing before and after the avalanche, which avalanche signal is clearly observed and thus the time delay *Δt* between onset of pulse to onset of avalanche signal can be measured**

There are certain requirements on the values of passive elements ($R$ and $C$ in Figure 3-9a) in the gated quenching circuit [77]. To minimize an attenuation of a pulse amplitude due to the capacitor in the gated quenching circuit and the inherent device capacitance $C_d$ in the APD by voltage division, the requirement on the capacitor is

$$C \gg 100C_d \tag{39}$$

The device capacitance $C_d$ can be estimated by comparing the actual signal with the fitting function proportional to $\exp(-t/RC_d)$. To minimize a pulse decay within 1%, there is another requirement on the rectangular pulse duration $T$, the resistor $R$, and a duty cycle $w$.

$$T \leq \frac{RC}{100} \tag{40}$$

$$w \leq 0.01 \tag{41}$$

Keeping the requirements above, the passive circuit elements are optimized empirically by changing $R$ and $C$ to obtain the best baseline profile. The chosen value of the resistance $R$ is 47 kΩ, the value of the capacitance $C$ is 100 nF, the pulse duration $T$ is 200 ns, and the duty cycle $w$ is 0.0002.

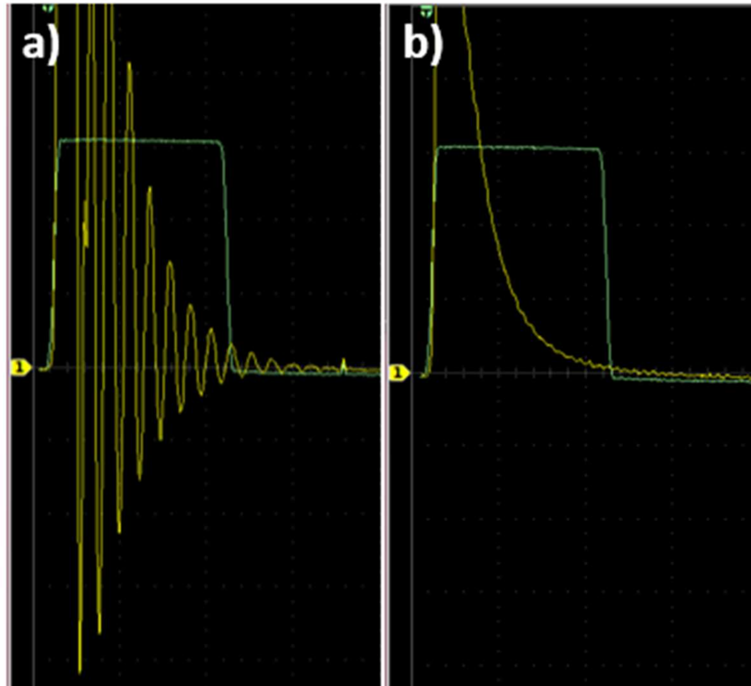


**Figure 3-10 a) The oscillation added in the output node of the transimpedance amplifier is visualized in the DRS4 oscilloscope. b) the oscillation is removed by connecting a compensating capacitor $C_F$ in parallel with the feedback resistor**

When the transimpedance amplifier is utilized with a feedback resistor $R_F$ and the APD alone, there is an oscillation added at the output node of the transimpedance amplifier. This is called the gain-peaking problem, and this oscillation is due to the inherent capacitance inside the APD that creates an additional pole in the transimpedance amplifier feedback system. This two-pole system (one from the inherent capacitance of the APD and one from the op-amp) will create a non-zero gain signal at the frequency where the loop gain's phase shift is 180° (opposite phase). When the non-zero gain signal with an opposite phase is subtracted from the inverting input (-) of the op amp, the signal will enhance, which creates

the oscillation. This problem can be easily solved by adding a compensating capacitance, $C_F$, in parallel with the feedback resistor [93].

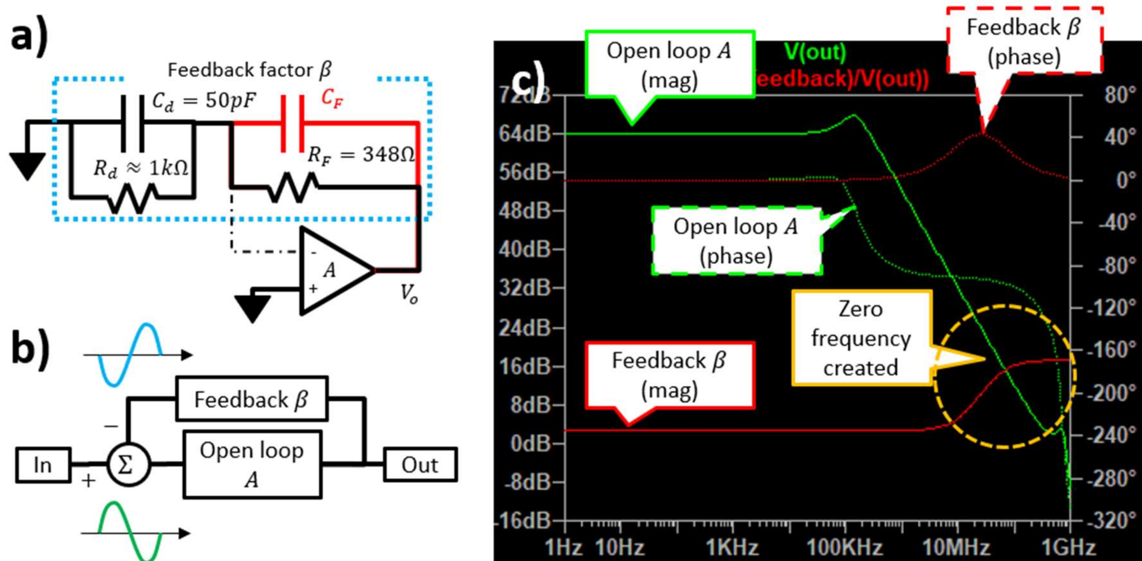


**Figure 3-11 a) the circuit diagram of the APD with the transimpedance amplifier. The APD is modeled into a resistance $R_d$ and capacitance $C_d$ connected in parallel. The compensating capacitor $C_F$ is connected in parallel with feedback resistor $R_F$. b) Modeling the APD and transimpedance amplifier circuit into a feedback system with feedback factor $\beta$ and an open loop gain $A$ of the op amp. The sinusoidal signal at the inverting (-) input shows that the phase difference is -180° (opposite phase) compared with the signal at the noninverting (+) input. This makes positive feedback and the input signal gets larger and larger, thus creating the oscillation. c) Simulation of a gain-frequency plot of the open loop A and the feedback factor $\beta$. The compensating capacitance $C_F$ can be obtained by looking at the plot where the zero frequency of the feedback gain $\beta$ crosses the open loop gain $A$**

To find the value of the compensating capacitance, the APD and the transimpedance amplifier circuit system (Figure 3-11a) is modeled into a feedback system with a feedback factor $\beta$, with an open loop gain $A$ of the op-amp (Figure 3-11b). The feedback factor $\beta$ can be expressed in terms of $R_d$, $C_d$ (the APD resistance and capacitance respectively), $C_F$, $R_F$, and the frequency $\omega = 2\pi f$.

$$\beta = \frac{R_d}{R_F + R_d} \frac{j\omega R_F C_F + 1}{j\omega R_F || R_d (C_d + C_F) + 1} \tag{42}$$

Then the open-loop gain *A* of the op-amp (usually depends on the frequency) and the feedback factor $\beta$ is plotted together in a gain-frequency plot (Figure 3-11c). The rule of thumb of finding the value of the compensating capacitance is to create a zero frequency $f_z$ in the feedback factor $\beta$ where it crosses the open loop curve *A* (denoted in the orange dotted circle in Figure 3-11c). The zero frequency $f_z$ can be obtained by setting the numerator of the feedback factor $\beta$ to zero, and is related with the compensating capacitance by

$$f_z = \frac{1}{2\pi R_F C_F}. \tag{43}$$

When the feedback factor $\beta$ crosses the open loop gain *A* curve, it will automatically move a loop-gain curve $A\beta$ away from the 0 dB line (unity gain) before the phase reaches -135°. Then the whole circuit is stable, and the oscillation is removed.

Instead of finding the zero frequency $f_z$ that crosses the open loop curve *A,* an equation is already available for finding the compensating capacitance $C_F$ [93].

$$C_F = \sqrt{\frac{C_d + C_M + C_D}{2\pi R_F f_{CR}}} \tag{44}$$

The $f_{CR}$, $C_M$, and $C_D$ are an amplifier crossover frequency, a common-mode capacitance of the op-amp, and a differential capacitance of the op-amp respectively, and are usually found in a datasheet of the op-amp ($f_{CR}$ = 410MHz). From the above equation, the calculated value of the compensating capacitance is 7.5 pF.

### *3.4.2 Low-temperature control system*

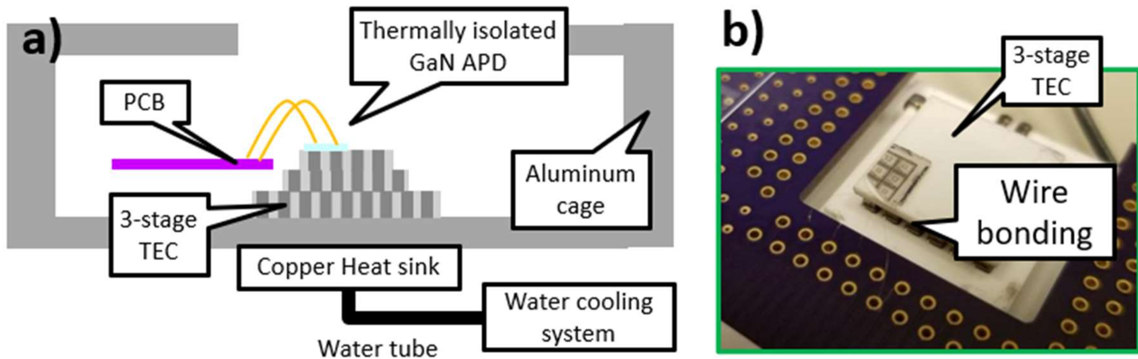


**Figure 3-12 a) Schematic diagram of a three-stage thermoelectric cooler (TEC) module, aluminum cage, heatsink with circulating cooling water + ethylene glycol mixture. b) photograph of the APD attached directly on the TEC module. The APD is connected to the PCB via wire bonding.**

To achieve low temperature operation of the APD, a three-stage thermoelectric cooler (TEC) module is utilized. The APD is directly attached on the surface of the TEC module, and the bottom of the TEC module is attached to an aluminum cage. The APD is electrically connected to a printed circuit board (PCB) via wire bonding, but thermally isolated except by an ambient gas. The aluminum cage is circulated with a cooling water + ethylene glycol mixture (1:1.5). With this TEC setup, the minimum temperature it can reach is -45°C. (however, the minimum temperature used with this setup is -40°C, since the temperature is not stable at -45°C.)

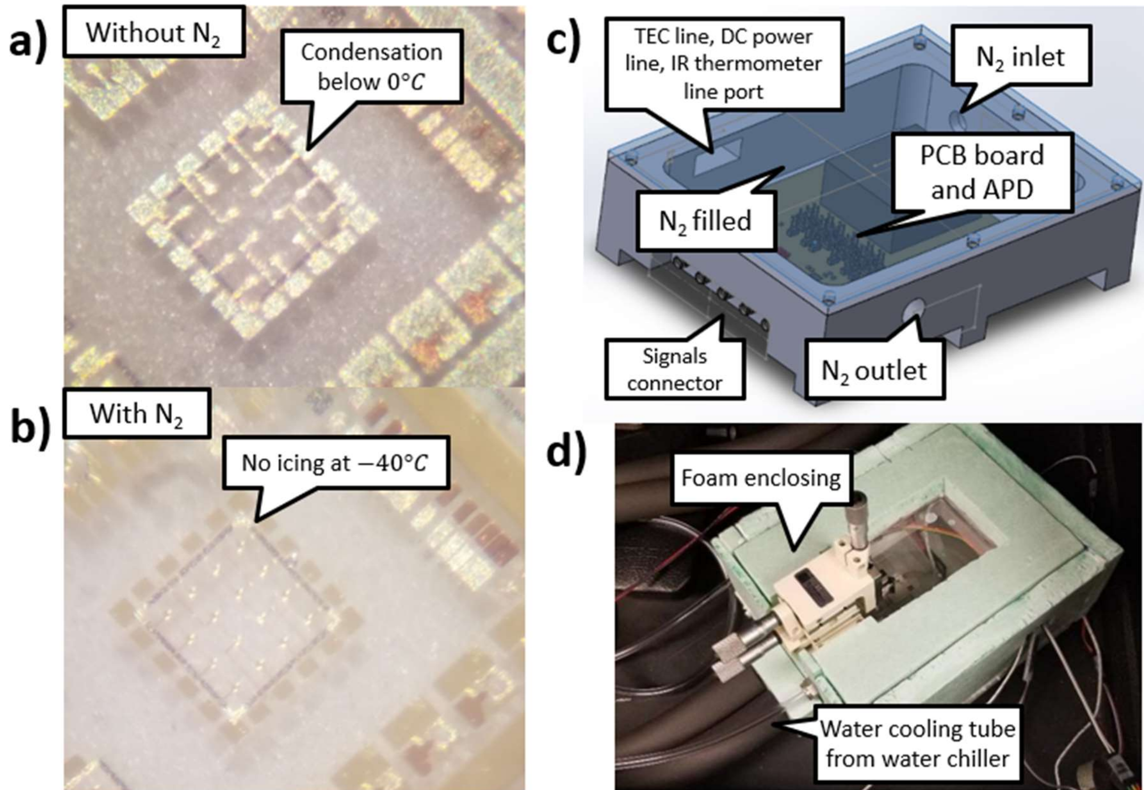


**Figure 3-13 a) A microscope image of the GaN APD surface when the surface temperature is below 0°C and exposed to an outside air. Notice there is moisture condensation on the surface of the APD. b) If the nitrogen is filled instead of the air, there is no condensation or icing even at -40°C. c) Solidworks design of the aluminum cage with the lid, nitrogen inlet and outlet, electrical ports, and the PCB board and the APD. d) A photograph image of complete aluminum cage with foam enclosing the outside surface.**

If the APD is exposed to an outside air when the temperature of the APD goes down below the dew point of the ambient air, moisture condensates, and water precipitates on the device surface (Figure 3-13a). To avoid this, the relative humidity of the test chamber is lowered by filling the aluminum cage with nitrogen gas. For example, the aluminum cage is cooled down to 0 °C which cools down the ambient gas inside to 0 °C. At the relative humidity of 2%, the dew point reaches down to -43°C. This means that the TEC module surface has to be below -43°C in order for the moisture to condensate.

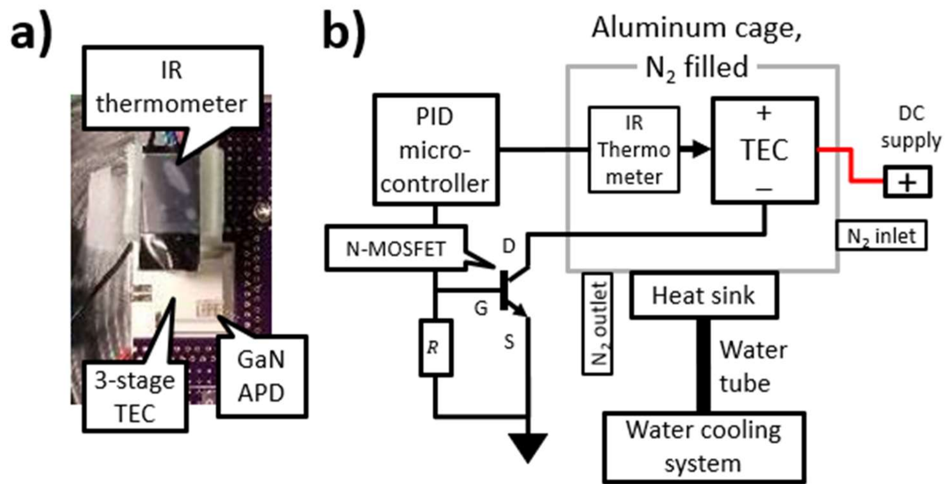


**Figure 3-14 a) photograph of an infrared thermometer monitoring the surface of the 3-stage TEC module, and the GaN APD is attached to the surface of the TEC module. b) schematic diagram of a PID controller, which consists of a microcontroller, the IR thermometer, the TEC module, an *n*-MOSFET, and a DC supply. The IR thermometer and the TEC module is inside the aluminum cage, filled with nitrogen gas.**

A proportional–integral–derivative (PID) controller is used to control the temperature. In the temperature control system, an infrared (IR) thermometer is installed above the three-stage TEC module, monitoring the temperature of the surface of the TEC (Figure 3-14a). (The assumption is that the temperature is uniform across the whole surface, including the GaN APD.) A microcontroller (Arduino UNO) is connected to the IR thermometer, reading the temperature (Figure 3-14b). The microcontroller controls an *n*-MOSFET switch, which turns on and off the TEC module. The TEC module is connected to a DC supply with constant voltage. The microcontroller controls the *n*-MOSFET with a pulse-width modulation.

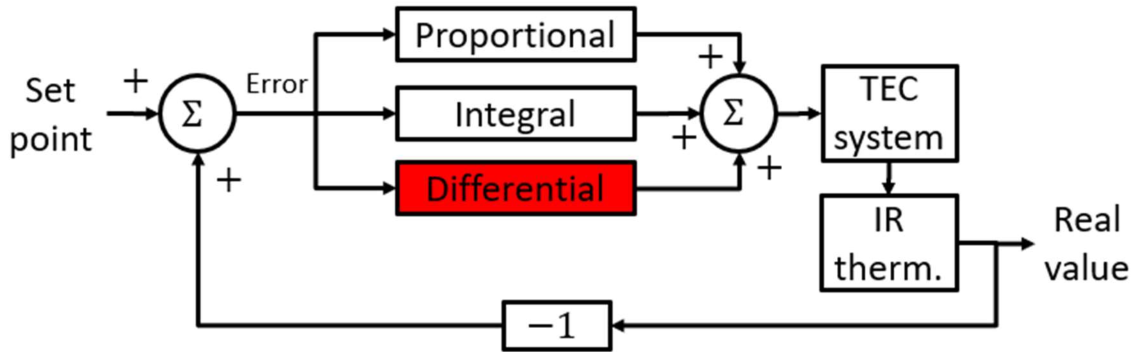


**Figure 3-15 Schematic diagram of a PID controller algorithm, including a proportional, an integral, and a differential term. In the real system, the differential term is not required since there is no sudden change of the temperature.**

A simple PID controller program is uploaded to the microcontroller (Figure 3-15). In the PID controller program, an error value $E(n)$ is calculated by subtracting a measured real value from a desired set point, and is sent to a proportional, an integral and a differential term simultaneously [94]. In the proportional term, the error value is multiplied with a constant ($P(n) = K_p \times E(n)$). In the integral term, the error value is multiplied with another constant, and subtracted from a previous integral term ($I(n) = K_i \times E(n) + I(n-1)$). The integral term is required for rejecting a constant bias disturbance (offset). In the differential term, the error value is subtracted from the previous error value, divided by a time interval $\Delta T$, and multiplied with another constant ($D(n) = K_d \times (E(n) - E(n-1))/\Delta T$). The differential term is required for giving a sharp response to a sudden change of signal. However, since the temperature of the TEC module responds slowly to an input, this term is not needed. The sum of all the terms is translated to the pulse width, which turns on and off the *n*-MOSFET switch of the TEC

module. Then the IR thermometer measures the temperature of the surface of the TEC module and the signal is fed back. To find the constant $K_p$ and $K_i$, both terms are set to zero at first. Then the constant $K_p$ is increased until the rise time of the temperature does not change. Finally, the constant $K_i$ is increased until the offset from the set point is corrected. The PID controller enables a precise control of the temperature of the surface of the TEC module, within an error of ±0.5°C (Figure 3-16)

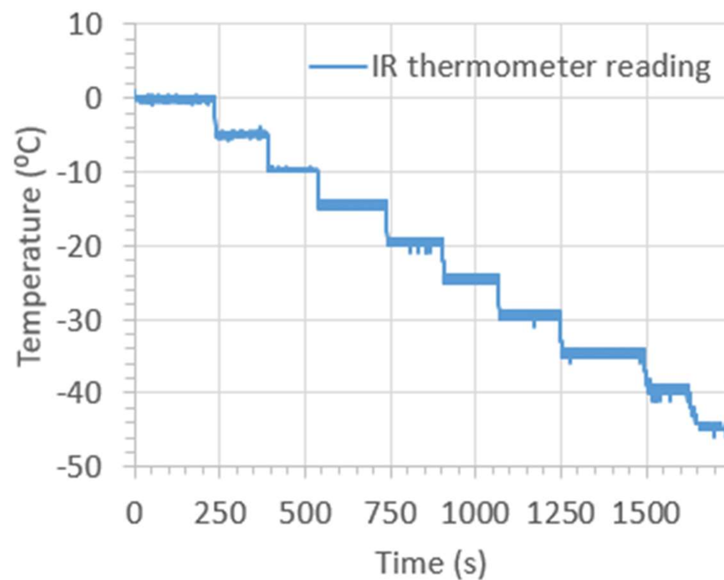


**Figure 3-16 A graph of temperature vs. time. The temperature is set to 0 to -45°C, in decreasing steps of -5°C. Notice that the precise control of the temperature of the surface of the TEC module is possible.**

### *3.4.3 Ultraviolet illumination system*

A UV LED with a peak wavelength of 375nm was used as a photon source. UV light from the UV LED is illuminated on the surface of the GaN APD via a UV-grade fiber. Simultaneously, the UV light was also illuminated on the Si photon counter (Hamamatsu

Single Pixel Photon Counter C11202-050, 50μm diameter) for monitoring the photon count. In this way, the photon count measurement is stable even if the number of photons emitting from the UV LED varies over time. For such an application, a bifurcated fiber is used. The bifurcated fiber (Thorlabs BFY600HS02) has two fiber cores in one end and breaks out into two ends with one core each. The UV light is illuminated on the one end with two cores. On the bifurcated end, one end core goes to the GaN APD, and the other core goes to the Si photon counter (if attenuation is required, an attenuator is installed (Figure 3-8) and the attenuation factor is considered when calculating the photon detection efficiency)

When the fiber is used for illuminating the surface of the GaN APD, the fiber setup should be able to move freely mechanically, to adjust the position where it is illuminating, but the testing system must also simultaneously trap the nitrogen gas inside the cage to avoid water condensation. To solve this problem, an x-y-z stage is used for adjusting the fiber position, and OHP films are used to allow for a movable fixture that will seal the chamber effectively (Figure 3-17). The fiber end is connected to the x-y-z stage via a fiber holder, and the x-y-z stage is attached to an aluminum lid with a rectangular hole wide enough to observe inside the aluminum cage. Then two sheets of large OHP films are prepared, with a rectangular hole wide enough to move the fiber freely. A small OHP film with a circular hole size of the fiber cross-section is also prepared. The small OHP film is sandwiched between two sheets of large OHP films, and the fiber goes through the hole of the small OHP film. When all the parts are assembled, it is possible to observe inside the cage to adjust the position of the fiber, and not disturbing the nitrogen gas inside the cage.

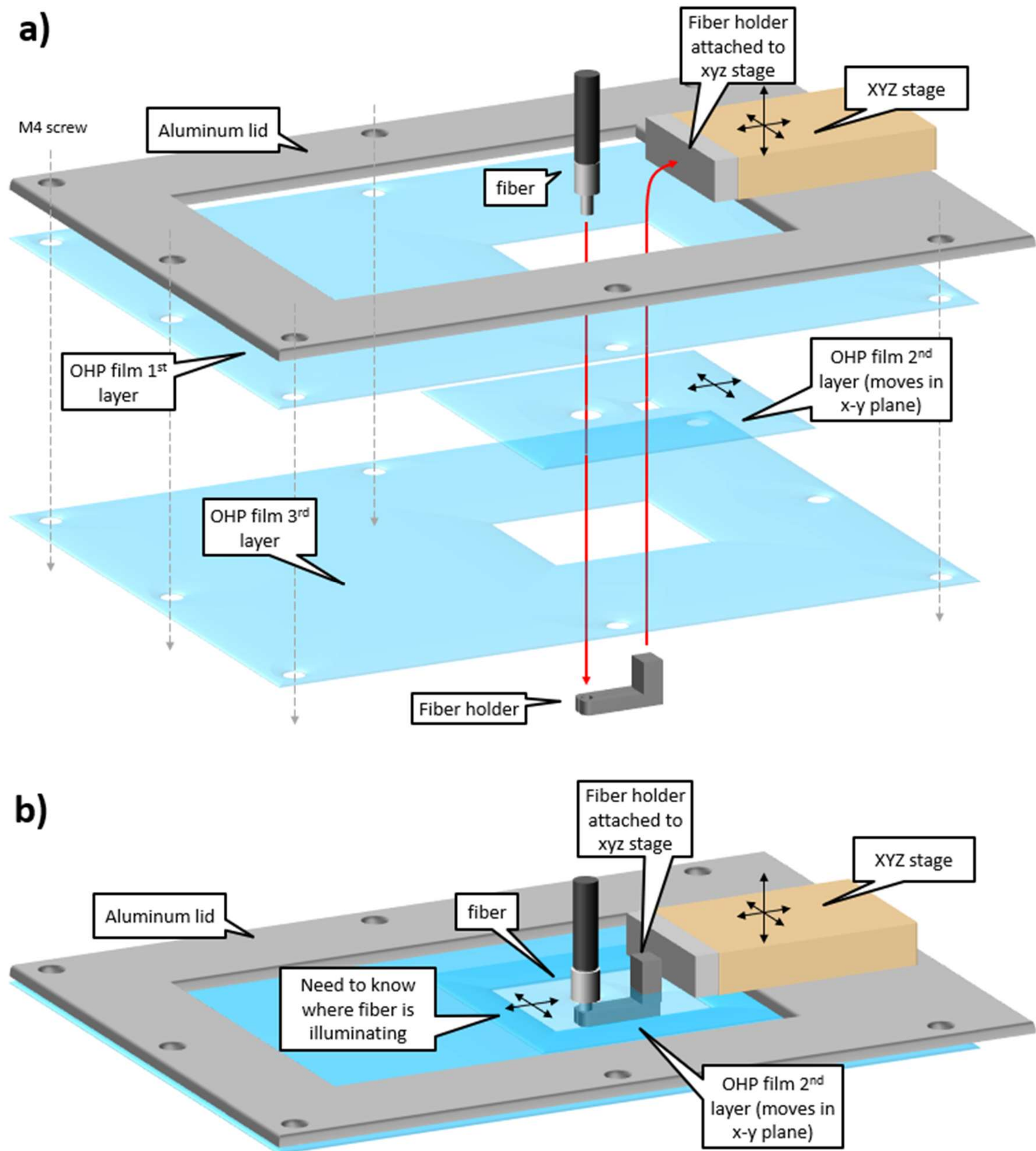


**Figure 3-17 A schematic diagram of fiber-aluminum lid complex structure a) before assembly and b) after the assembly. The fiber goes through the 2nd OHP film, which moves freely between two fixed OHP films with rectangular holes. Then the fiber is connected to the x-y-z stage. In this configuration, the nitrogen gas is trapped inside the cage with OHP films, and the fiber position can be adjusted.**

### *3.4.4 Software for dark count rate and photo detection efficiency calculation*

Once all the hardware systems including Geiger-mode-testing-circuit system, low-temperature control system, and UV-illumination system is complete, a software program was prepared for controlling all the equipment and calculating the DCR and the PDE. The program was written in C++ language, and the equipment (Oscilloscope, PID controller, DC supply, Si photon counter, and LED power) are connected to the computer via RS-232 serial communication.

The flow of the device testing algorithm (Figure 3-18) starts with sending the temperature set point of the TEC module. Next, the oscilloscope detects the onset of the pulse signal from the waveform generator. The DC bias is increased so that the sum of pulse amplitude and the DC bias is slightly below the breakdown voltage of the GaN APD, and the oscilloscope captures a baseline signal which is the signal before avalanching. Then the DC bias is increased so the total applied voltage is above the breakdown voltage, and the avalanche signal is captured without the light. The baseline signal is subtracted from the avalanche signal to get a pure avalanche signal. In this way, all the unwanted noise will be removed. At the computer, the time difference between the rise time of the pulse and the onset of the avalanche signal is calculated. This process is repeated over 10,000 events or more, and a histogram of how many avalanche events in certain time interval will be created. By fitting the slope of the histogram with the function proportional to $exp(-2 \cdot DCR \cdot \Delta t)$, the DCR is obtained. The DC bias is lowered so the total applied voltage is below the breakdown voltage.

Immediately after the DCR is measured, the DC bias is increased once again to reach breakdown voltage. This time, the UV LED is activated, and the Si photon counter is initialized to read an actual photon count simultaneously (multiplied by the optical attenuation factor). The avalanche signal is captured, the baseline is subtracted from the avalanche signal, the time difference is calculated, and a new histogram with the UV light is created. Finally, measuring the slope of the histogram will give a photon + dark count rate, and using the actual photon count from the Si photon counter, and the equation (28), the PDE is calculated.

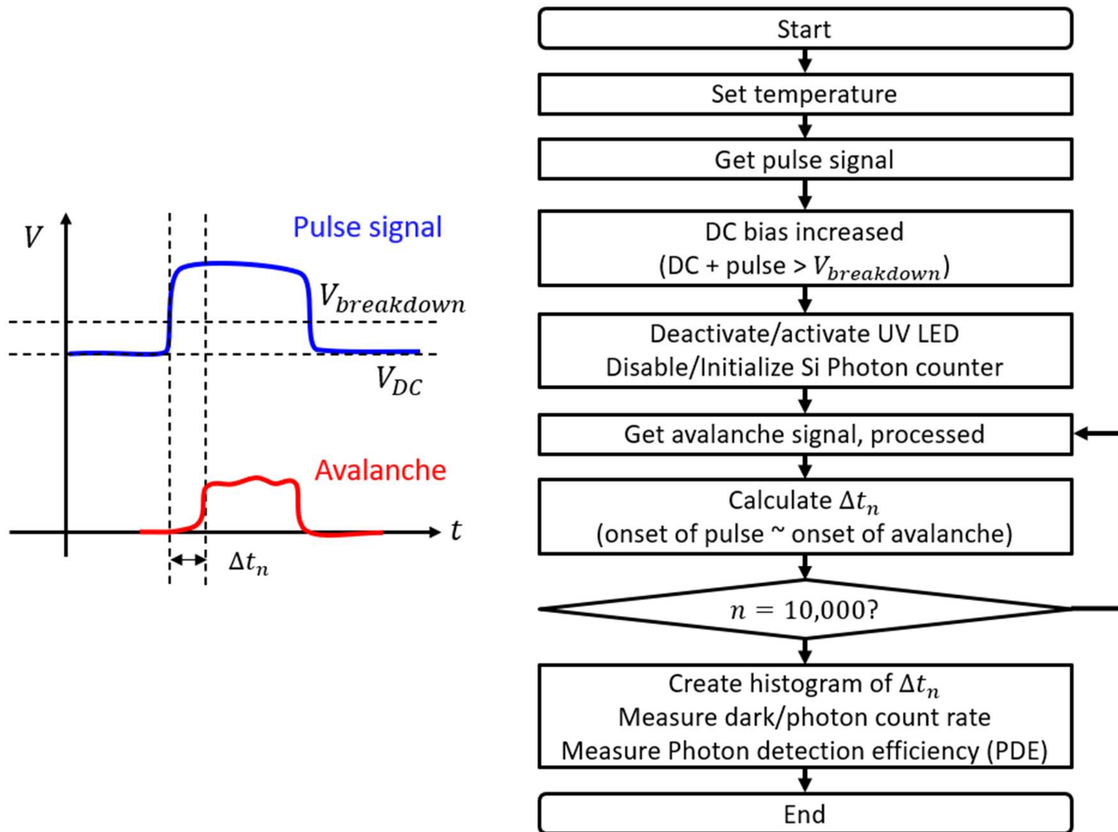


**Figure 3-18 The flow of algorithm for calculating the dark count rate and the photon detection efficiency is shown. The algorithm starts with setting the TEC module temperature, getting the pulse signal, increasing DC bias so that the total voltage is above the breakdown voltage of the GaN APD, deactivating/activating UV LED and Si photon counter (for dark count rate/photon count rate), getting the avalanche signal and calculating the time difference, and create the histogram. From the histogram the dark/photon count rate is calculated by measuring the slope, and the photon detection efficiency is obtained.**

## 3.5 Results and discussion

The theoretical modelling for various contributions to the dark count rate can be found in various thesis and articles [95, 96]. There are three mechanisms contributing to the DCR: thermal generation, trap-assisted tunneling, and band-to-band tunneling. These three

mechanisms are dependent on the temperature of the APD. The DCR due to the thermal generation can be expressed as a function of the temperature [95].

$$J_{therm}(T) \sim T^{11/2}\, exp\left(-\frac{E_g(T)}{kT}\right) \quad (45)$$

In the above expression, $k$ is the Boltzmann constant ($8.617 \times 10^{-5}$ $eV/K$), and $E_g\,(T)$ is the bandgap energy of the GaN material, which also depends on the temperature. The DCR due to the trap-assisted tunneling can be expressed as [95]

$$J_{TAT}(T,\mathcal{E}) \sim |\mathcal{E}|T^{\frac{1}{2}}\, exp\left(\frac{|q\hbar\mathcal{E}|^2}{24m^*(kT)^3} - \frac{E_g(T)}{2kT} - \frac{E_t - E_i}{kT}\right) \quad (46)$$

where $E_t$ is an average trap level within the bandgap, $E_i$ is intrinsic level of the GaN, $\mathcal{E}$ is the electric field in the junction, $m^*$ is the effective mass of the carriers, $q$ is the electrical charge ($1.609 \times 10^{-19}$ $C$), and $\hbar$ is the Planck constant ($6.582 \times 10^{-16}$ $eV/s$). The first and the third term inside the exponential function have weak dependence of the temperature compared to the second term. Lastly, the DCR due to the band-to-band tunneling can be written as [95]

$$J_{BTBT}(T,\mathcal{E}) \sim \mathcal{E}^{\sigma+1}\, exp\left(\frac{\pi^2\sqrt{m^*}E(T)_g^{3/2}}{\sqrt{2}qh\mathcal{E}}\right) \quad (47)$$

where σ is equal to 1 for a direct, and 3/2 for an indirect bandgap transition.

If above three DCR mechanisms are plotted in an Arrhenius plot (dark count rate vs. $1/kT$), the contribution from the thermally generated DCR has an activation energy of around the bandgap energy of the material ($\sim E_g$), the contribution from the trap-assisted tunneling

has half of the bandgap energy, ($\sim E_g/2$), and the band-to-band tunneling component has the weakest dependence at less than the half of the bandgap energy [97]. Also, the only contribution that does not depend on the electric field inside the intrinsic region is the thermally generated DCR. When the lattice gains energy (the temperature increases) the geometry for an electron momentum transfer is less favorable. This require more energy to free the electron, or higher applied electric field / voltage.

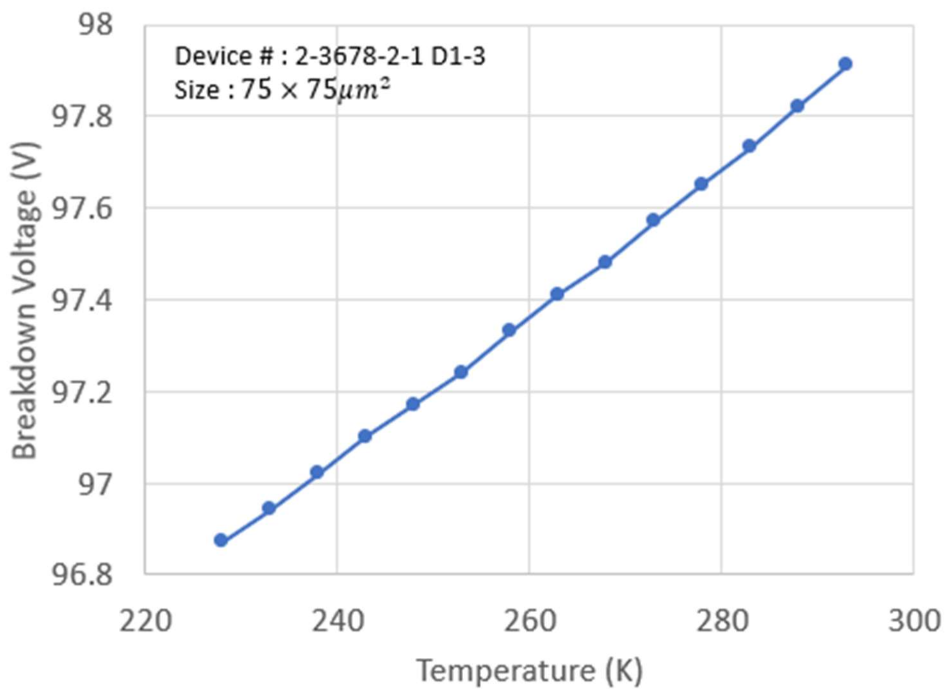


**Figure 3-19 Measured breakdown voltage as a function of temperature for the range from -45 to 20°C. The breakdown voltage is measured as the total DC + pulse voltage which gives the same probability of avalanching ($N_{avalanche}/N_{total}$). The temperature coefficient obtained is 0.0159 + 0.0034 V/K**

Before measuring the dark count rate and the photon detection efficiency, first the breakdown voltage of the GaN APD as a function of temperature is measured. The device under the test has the photoactive area of 75 × 75 μm$^2$. To measure the breakdown voltage, the total sum of DC bias and the pulse amplitude voltage is measured at which gives same

avalanche probability of 10% (which is 1,000 avalanche events out of total 10,000 trials). The measured temperature range is from 228 to 293K ($-45°C$ to $20°C$, with an increment step of 5°C). As observed in the Figure 3-19, the breakdown voltage is proportional to the temperature, monotonically varying from 96.87V to 97.91V when the temperature increases from -45°C to 20°C. By fitting the function with a straight line, positive temperature coefficient of $0.0159 \pm 0.0034\, V/K$ is obtained. The coefficient of temperature is similar with the previous measurement in our lab [98].

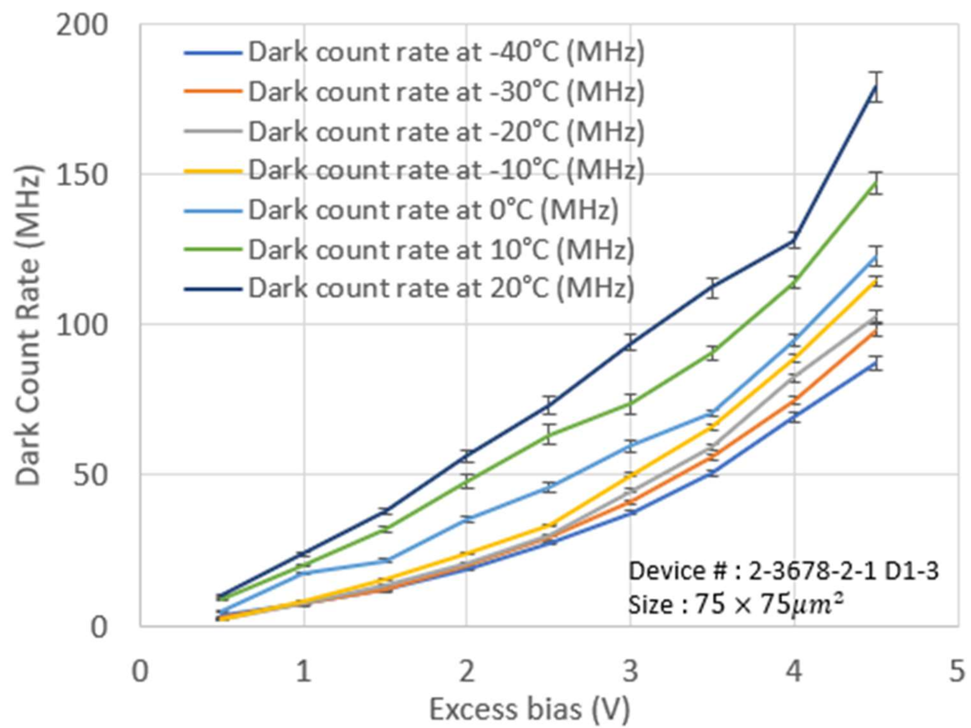


**Figure 3-20 The DCR as a function of excess bias at different temperature set points.**

The DCR as a function of excess bias at different temperature set points was measured and plotted (Figure 3-20). The excess bias is calculated from the breakdown voltage at different temperature set points. There is an exponential increase with increasing of the excess bias for each temperature set point, indicating that the contribution from tunneling is dominant instead of diffusion and generation recombination [99]

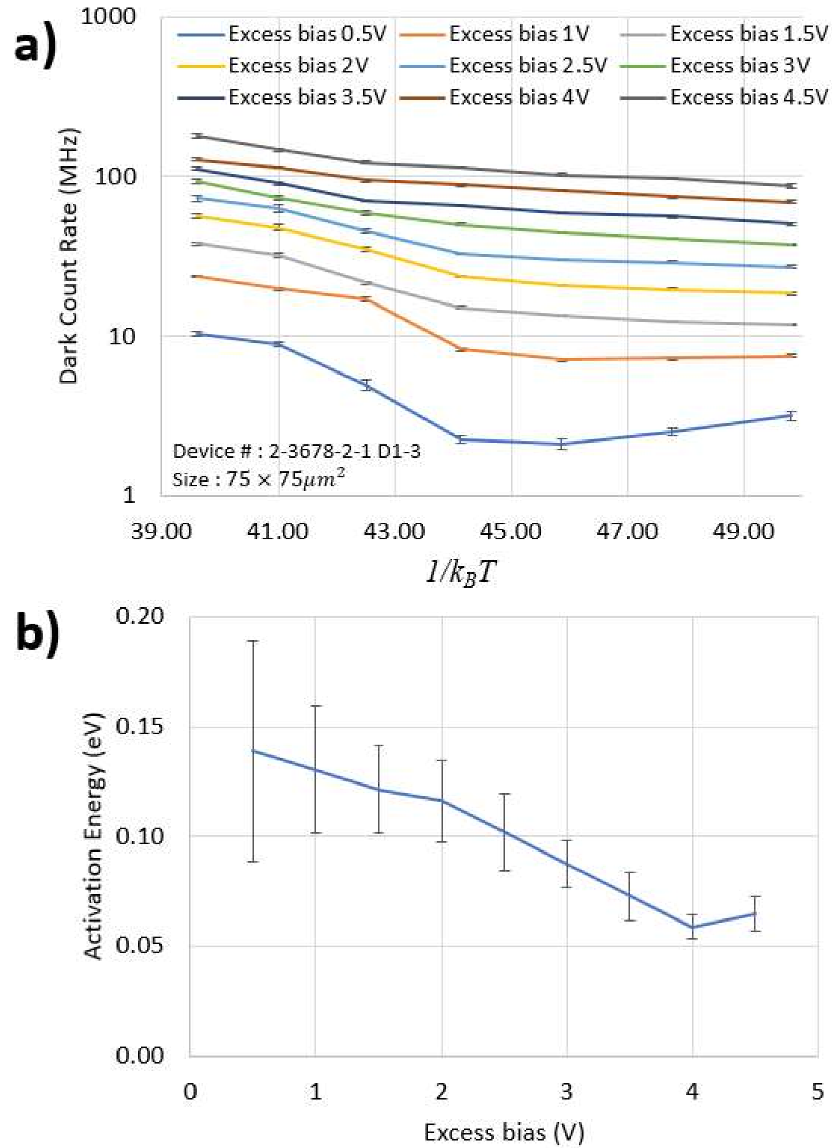


**Figure 3-21 a) The DCR as a function of reciprocal of the Boltzmann constant times the temperature at different excess bias voltages. b) The activation energy is obtained by fitting an Arrhenius equation.**

To analyze the dark-count mechanism of the GaN APD, the DCR is plotted as a function of temperature for different excess bias (i.e., an Arrhenius plot). Since the bandgap energy ($E_{g,GaN}$) of the GaN material is around 3.4 eV, one notices that the activation energies for the

entire excess bias range are much below the half of the GaN material bandgap energy ( $1.7eV$). This shows that in this temperature range from 20 to -40°C, the band-to-band tunneling (BTBT) is the dominant mechanism contributing to the dark count rate of the GaN APD.

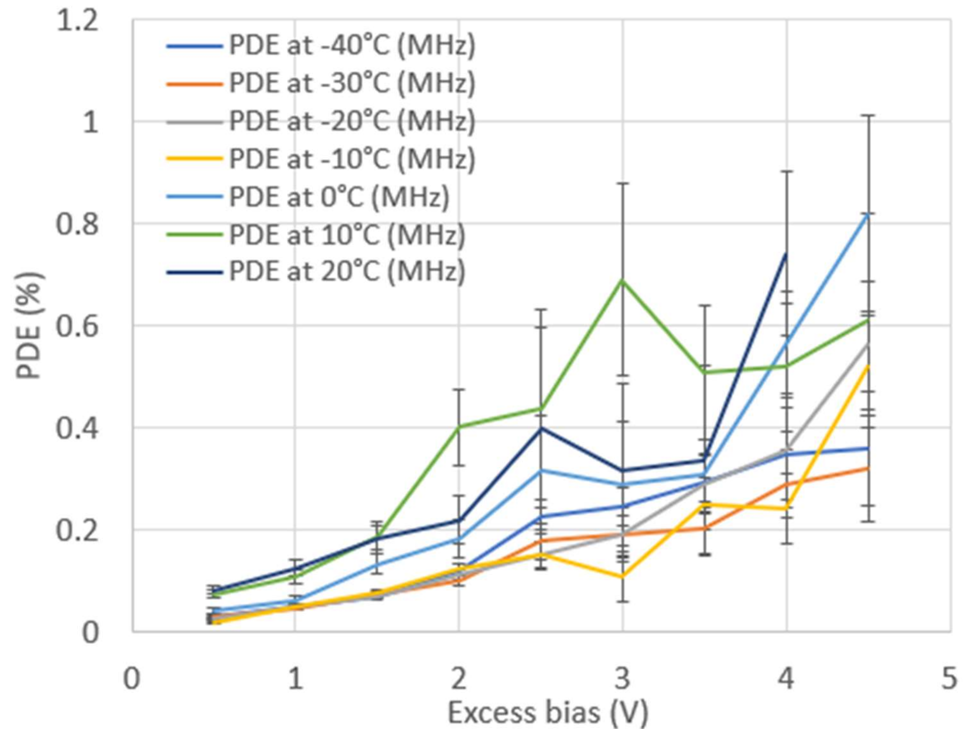


**Figure 3-22 The PDE of the GaN APD measured as a function of excess bias at different temperature set points. Notice that the error bars are so wide that other PDE curves are included in the error bars.**

The PDE of the GaN APD was measured as a function of excess bias at different temperature set points. It was observed that the PDE of the GaN APD increased as the excess bias increased. However, as is evident from the graph, the error bars of each PDE curve are so wide that these error bars include other PDE curves at different temperature set points. Thus the temperature has minor effect in increasing the PDE of the GaN APD.

### 3.6 Summary

In this project, we designed and constructed a temperature-controlled Geiger-mode APD measurement system using a TEC for device measurements at and below room temperature. The measurement system includes the gated quenching circuit with operational amplifiers isolating the APD from the unwanted electrical signal reflections. We have demonstrated the temperature dependence of the breakdown voltage of the GaN *p-i-n* APD in the range from -40 to 20ºC, and the temperature coefficient of the breakdown voltage was 0.0159 + 0.0034 V/K. For the first time in history, we have demonstrated the DCR as a function of the excess bias at different temperature set points, as well as the DCR as a function of temperature at different excess bias for GaN APDs. From the DCR vs. temperature plot in this range, we were able to discover that the dominant mechanism contributing to the dark-count rate of the APD is band-to-band tunneling, with an activation energy less than 0.15 eV. Lastly, we measured the PDE of the GaN APD as a function of excess bias at different temperature set points and found that the PDE increases as the excess bias increases but is independent of the temperature set points for this range. The main goals in this project were to analyze the dark-count mechanisms of the GaN APD, and search for methods to reduce the dark-count rate. For the aspect of improving the Geiger-mode measurement system, a way to improve the performance further is to measure the DCR and the PDE in a temperature range lower than -50ºC. For the aspect of improving the GaN APD device, it is suggested to use wider depletion region, to reduce the contribution from the band-to-band tunneling [75].

# CHAPTER 4. RESEARCH SUMMARY

There are two related research projects described in this work. One is the design, growth, fabrication, and characterization of DUV $Al_{0.6}Ga_{0.4}N$ *p-i-n* APDs, and the other is the development of low-temperature Geiger-mode measurements of GaN *p-i-n* APDs.

The $Al_xGa_{1-x}N$ material system has tunable direct bandgap energy from 3.4 to 6.02 eV, and $Al_xGa_{1-x}N$ photodetectors can operate in the solar-blind spectral region ($\lambda < 280$ nm) when $x > 0.45$. Particularly for the $Al_xGa_{1-x}N$ photodetectors with $x > 0.6$, the ratio of the hole to electron ionization coefficient is predicted to be less than 1, which reduces the excess noise factor. However, AlGaN photodetectors are often grown on foreign substrates, and large dislocation densities and lattice-mismatch-induced defects will exist owing to the lattice mismatch of the AlN/sapphire and AlGaN/sapphire interfaces and the mismatch in lattice parameters and the difference in thermal expansion coefficients will cause cracking of the material. Moreover, the activation efficiency of the Mg acceptor is low in AlGaN which causes low effective *p*-type Mg doping concentrations. Lastly, there has been difficulty in observing a distinctive breakdown behavior in the *I-V* characteristics of $Al_{0.6}Ga_{0.4}N$ APDs since to date, there are no clear avalanche breakdown voltages reported. In our DUV $Al_{0.6}Ga_{0.4}N$ *p-i-n* APDs project, the APDs were designed such a way to minimize strains from each layer by introducing several transition layers and step-grading layers. Two types of AlN/sapphire templates and a AlN bulk substrate with different dislocation densities were prepared. The layers of the AlGaN APD structure were grown with conditions which minimize the carbon impurity incorporation. The AlGaN APD structures were fabricated to minimize the etching damage, and to have ohmic *n*-type and *p*-type contacts. The *J-V* curves

of the fabricated $Al_xGa_{1-x}N$ APD devices showed dark current density vs. reverse bias characteristics with distinctive breakdown behavior in which there is an abrupt increase in the current around the reverse bias of -140V. The achieved leakage current density is the lowest, around $1 \times 10^{-8}$ A/cm$^2$, for the APDs having a diameter of 20 µm grown on the AlN bulk substrate. The optical gain of $1.63 \times 10^4$ was achieved at the wavelength of 250 nm and a reverse bias of -145 V. At zero bias, the photoresponse was 71.45 mA/W at a wavelength of 250 nm. Although the temperature coefficient of breakdown voltage was measured to be negative for AlGaN APDs fabricated using three substrates, it was observed that as the dislocation density of substrate decreased, the temperature coefficient was increasing toward a positive value.

The APD is a device which can be designed to detect single or multiple photons and is one of the important optoelectronic device applications for III-N materials. To detect a single photon, the APD must be operated in Geiger mode, and this requires a special type of bias circuit called quenching circuit. In Geiger-mode operation of the APD, the DCR and PDE are often used parameters to evaluate the device performance. There were several prior reports demonstrating Geiger-mode operation of GaN APDs, however there was no work reporting the Geiger-mode operation of the GaN APDs at low temperature and the analysis of the origin of dark-count mechanisms. In our studies of the low-temperature Geiger-mode operation of GaN APDs, we applied the principles of single-photon detection, and designed and fabricated the low-temperature Geiger-mode measurement system by integrating three hardware systems and one software program to control the equipment. The hardware systems consist of a device driver circuit system, a UV illumination system, and a low-temperature control system. In the driver circuit system, a quenching circuit was modified to include two operational amplifiers

for isolating the APD from the unwanted signal reflection. In the low-temperature control system, a thermoelectric cooler module was installed to control the temperature of the device in the range -40 °C < $T$ < 20 °C, in a nitrogen ambient. The GaN *p-i-n* APD device was previously fabricated at Georgia Tech. With the complete Geiger-mode APD testing system, we have demonstrated the temperature dependence of the breakdown voltage of GaN *p-i-n* APDs in the range from -40 to 20°C, and the temperature coefficient of the breakdown voltage was 0.0159 ± 0.0034V/K. The DCR as a function of different temperature set points at different excess bias was demonstrated for the first time in history to the best of our knowledge. From the DCR vs. temperature plot, it was possible to analyze that the dominant mechanism contributing to the dark-count rate of the GaN APD is band-to-band tunneling, judging from the fact that the activation energy of the DCR is less than the half of the bandgap energy. We also demonstrated the PDE of the APD as a function of excess bias at different temperature set points and found that the PDE is independent of the temperature set points.

# CHAPTER 5. FUTURE WORKS

In future works of the DUV AlGaN p-i-n APD project, electric field and optical simulation must be performed in the design part. Prior to electric field simulation, the doping property of a *p*-type $Al_{0.6}Ga_{0.4}N$ must be characterized first. Once the correct electric field simulation of the GaN APD is obtained, it is possible to fit Poole-Frenkel current equation to the function $\ln(J/E)$ vs. $\sqrt{E}$, [98, 100] ($J$ is current density), which is expressed as below.

$$J_{PF} = J_o E e^{-\frac{q\phi - \beta\sqrt{E}}{kT}} \tag{48}$$

In the above equation, $J_0$ and $\beta$ are constants, $E$ is electric field in the *i*-layer. From the fitting, the barrier height $\phi$ can be estimated, and it is in progress. In the optical simulation, transfer matrix method [101] should be used.

$$T = \frac{4\eta_0 Re(\eta_m)}{(\eta_0 B + C)(\eta_0 B + C)^*} \tag{49}$$

$$\begin{bmatrix} B \\ C \end{bmatrix} = \prod_{r=1}^{q} \begin{bmatrix} \cos\delta_r & i\sin\delta_r/\eta_r \\ i\eta_r \sin\delta_r & \cos\delta_r \end{bmatrix} \begin{bmatrix} 1 \\ \eta_m \end{bmatrix} \tag{50}$$

In the above equations, $\eta_r$ is the admittance of the $r^{th}$ material in the stack, which is equal to $(n - ik)\sqrt{\frac{\epsilon_0}{\mu_0}}$, and $\delta_r$ is equal to $\frac{2\pi N_r d_r \cos\theta_r}{\lambda}$. In the fabrication part, the AlGaN APD devices on AlN substrates using ion implantation with nitrogen ions is in progress for electrical isolation to further reduce sidewall leakage current sources. More study should be done for the relationship between dislocation density vs. temperature coefficient of breakdown voltage,

which require detailed transmission electron microscopy (TEM) analysis, and statistics of *I-V* curve on three wafers as well.

The future works of low-temperature Geiger-mode measurement of GaN APD can be divided into three parts: 1) device part, 2) measurement system part, and 3) analysis part. In the device part, since the major contribution of the dark-count rate of the GaN APD has been shown to be band-to-band tunneling, it is suggested to use wider depletion region. This will increase the reverse-bias voltage for achieving avalanche breakdown but should reduce the DCR. In the measurement system part, due to the hardware limitations (mainly the low-temperature system), the analysis of the Geiger-mode operation of the GaN APD could be done only down to a temperature of -40°C. It is possible that a better analysis of the Geiger-mode operation of these APDs could be done if the measurement temperature is lowered below -50°C. In the analysis part, more study on the activation energy and model for PDE is in progress. The activation energy can be modeled by equating the Arrhenius equation $\exp(E_a/kT)$ with equation (47). It was possible to model the decreasing behavior of the activation energy, but actual fitting is in progress. In the modelling of PDE, it is possible to fit the PDE vs. excess bias with equation [102]

$$PDE(V_{ex}) = PDE_{max}(1 - exp(-O \cdot V_{ex}/V_{br})) \quad (51)$$

$$P_d(V_{ex}) = 1 - exp(-O \cdot V_{ex}/V_{br}) \quad (52)$$

where $V_{ex}$ is excess bias, $V_{br}$ is breakdown voltage of GaN APD, $PDE_{max}$ is a maximum PDE of GaN APD, $P_d$ is breakdown probability, and $O$ is Otte number. The Otte number is a dimensionless parameter which depends on whether an electron or hole initiates a breakdown.

By fitting PDE vs. excess bias with above equation, the Otte number can be obtained and predict what excess bias will have breakdown probability around 90% [17]

# REFERENCES


[1] H. Morkoc, *Handbook of Nitride Semiconductors and Devices*. Wiley, 2008.

[2] A. R. Acharya, "Group III–nitride semiconductors: preeminent materials for modern electronic and optoelectronic applications," *Himalayan Physics,* vol. 5, pp. 22-26, 2014.

[3] *Modified from the image in Gallium nitride in Wikipedia, the Free Erncyclopedia (2021)*.

[4] L. Vegard, "Die konstitution der mischkristalle und die raumfüllung der atome," *Zeitschrift für Physik,* vol. 5, no. 1, pp. 17-26, 1921.

[5] S. Yoshida, S. Misawa, Y. Fujii, S. Takada, H. Hayakawa, S. Gonda, and A. Itoh, "Reactive molecular beam epitaxy of aluminium nitride," *Journal of Vacuum Science and Technology,* vol. 16, no. 4, pp. 990-993, 1979.

[6] J. Arthur and J. LePore, "GaAs, GaP, and GaAs x P 1− x Epitaxial Films Grown by Molecular Beam Deposition," *Journal of Vacuum Science and Technology,* vol. 6, no. 4, pp. 545-548, 1969.

[7] H. Manasevit and K. Hess, "The use of metalorganics in the preparation of semiconductor materials," *J. Electrochem. Soc,* vol. 126, no. 11, pp. 2031-2033, 1979.

[8] H. M. Manasevit, "Single-crystal gallium arsenide on insulating substrates," *Applied Physics Letters,* vol. 12, no. 4, pp. 156-159, 1968.

[9] R. Pelzel, "A comparison of MOVPE and MBE growth technologies for III-V epitaxial structures," in *CS MANTECH Conference*, 2013, pp. 105-108: Citeseer.

[10] M. Ludowise, "Metalorganic chemical vapor deposition of III-V semiconductors," *Journal of Applied Physics,* vol. 58, no. 8, pp. R31-R55, 1985.

[11] W. Haecker, O. Groezinger, and M. Pilkuhn, "Infrared photon counting by Ge avalanche diodes," *Applied Physics Letters,* vol. 19, no. 4, pp. 113-115, 1971.

[12] W. J. Kindt, "Geiger mode avalanche photodiode arrays: For spatially resolved single photon counting," *Ph. D. Thesis*, 1999.

[13] G. Morton, "Photon counting," *Applied Optics,* vol. 7, no. 1, pp. 1-10, 1968.

[14] W. Becker, *Advanced time-correlated single photon counting techniques*. Springer Science & Business Media, 2005.

[15] S. M. Sze, Y. Li, and K. K. Ng, *Physics of semiconductor devices*. John wiley & sons, 2021.

[16] S. Miller, *Optical fiber telecommunications*. Elsevier, 1979.

[17] N. Gisin, G. Ribordy, W. Tittel, and H. Zbinden, "Quantum cryptography," *Reviews of Modern Physics,* vol. 74, no. 1, pp. 145-195, 03/08/ 2002.

[18] A. L. Lacaita, P. A. Francese, S. D. Cova, and G. Riparmonti, "Single-photon optical-time-domain reflectometer at 1.3 μm with 5-cm resolution and high sensitivity," *Optics letters,* vol. 18, no. 13, pp. 1110-1112, 1993.

[19] V. Spanoudaki, A. Mann, A. Otte, I. Konorov, I. Torres-Espallardo, S. Paul, and S. Ziegler, "Use of single photon counting detector arrays in combined PET/MR: Characterization of LYSO-SiPM detector modules and comparison with a LSO-APD detector," *Journal of Instrumentation,* vol. 2, no. 12, p. P12002, 2007.

[20] K. Suhling, J. Siegel, D. Phillips, P. M. French, S. Lévêque-Fort, S. E. Webb, and D. M. Davis, "Imaging the environment of green fluorescent protein," *Biophysical journal,* vol. 83, no. 6, pp. 3589-3595, 2002.

[21] Z. Xu and B. M. Sadler, "Ultraviolet communications: potential and state-of-the-art," *IEEE Communications Magazine,* vol. 46, no. 5, pp. 67-73, 2008.

[22] R. Foord, R. Jones, C. Oliver, and E. Pike, "The use of photomultiplier tubes for photon counting," *Applied optics,* vol. 8, no. 10, pp. 1975-1989, 1969.

[23] *Photomultiplier Tubes - Basics and Applications*, 3rd ed. Hamamatsu Photonics, 2006.

[24] W. G. Oldham, R. R. Samuelson, and P. Antognetti, "Triggering phenomena in avalanche diodes," *IEEE Transactions on electron devices,* vol. 19, no. 9, pp. 1056-1060, 1972.

[25] *Available: https://www.hamamatsu.com/eu/en/product/optical-sensors/mppc/index.html*.

[26] R. Cheung, *Silicon carbide microelectromechanical systems for harsh environments*. World Scientific, 2006.

[27] F. Yan, Y. Luo, J. Zhao, and G. Olsen, "4H-SiC visible blind UV avalanche photodiode," *Electronics Letters,* vol. 35, no. 11, pp. 929-930, 1999.

[28] F. Yan, J. H. Zhao, and G. H. Olsen, "Demonstration of the first 4H-SiC avalanche photodiodes," *Solid-State Electronics,* vol. 44, no. 2, pp. 341-346, 2000.

[29] X. Bai, H.-D. Liu, D. C. McIntosh, and J. C. Campbell, "High-detectivity and high-single-photon-detection-efficiency 4H-SiC avalanche photodiodes," *IEEE Journal of quantum electronics,* vol. 45, no. 3, pp. 300-303, 2009.

[30] S. Yang, D. Zhou, X. Cai, W. Xu, H. Lu, D. Chen, F. Ren, R. Zhang, Y. Zheng, and R. Wang, "Analysis of dark count mechanisms of 4H-SiC ultraviolet avalanche photodiodes working in Geiger mode," *IEEE Transactions on Electron Devices,* vol. 64, no. 11, pp. 4532-4539, 2017.

[31] H. Dong, H. Zhang, L. Su, D. Zhou, W. Xu, F. Ren, D. Chen, R. Zhang, Y. Zheng, and H. Lu, "After-Pulse Characterizations of Geiger-Mode 4H-SiC Avalanche Photodiodes," *IEEE Photonics Technology Letters,* vol. 32, no. 12, pp. 706-709, 2020.

[32] J. Carrano, T. Li, P. Grudowski, C. Eiting, D. Lambert, J. Schaub, R. Dupuis, and J. Campbell, "Low dark current pin ultraviolet photodetectors fabricated on GaN grown by metal organic chemical vapour deposition," *Electronics Letters,* vol. 34, no. 7, pp. 692-694, 1998.

[33] J. Carrano, T. Li, D. Brown, P. Grudowski, C. Eiting, R. Dupuis, and J. Campbell, "High-speed pin ultraviolet photodetectors fabricated on GaN," *Electronics Letters,* vol. 34, no. 18, pp. 1779-1781, 1998.

[34] A. Osinsky, M. Shur, R. Gaska, and Q. Chen, "Avalanche breakdown and breakdown luminescence in p-/spl pi/-n GaN diodes," *Electronics Letters,* vol. 34, no. 7, pp. 691-692, 1998.

[35] K. McIntosh, R. Molnar, L. Mahoney, K. Molvar, N. Efremow Jr, and S. Verghese, "Ultraviolet photon counting with GaN avalanche photodiodes," *Applied Physics Letters,* vol. 76, no. 26, pp. 3938-3940, 2000.

[36] S. Verghese, K. McIntosh, R. J. Molnar, L. J. Mahoney, R. L. Aggarwal, M. W. Geis, K. M. Molvar, E. K. Duerr, and I. Melngailis, "GaN avalanche photodiodes operating in linear-gain mode and Geiger mode," *IEEE Transactions on Electron Devices,* vol. 48, no. 3, pp. 502-511, 2001.

[37] R. McClintock and M. Razeghi, "Ultraviolet avalanche photodiodes," in *Optical Sensing, Imaging, and Photon Counting: Nanostructured Devices and Applications*, 2015, vol. 9555, p. 95550B: International Society for Optics and Photonics.

[38] M.-H. Ji, J. Kim, T. Detchprohm, Y. Zhu, S.-C. Shen, and R. D. Dupuis, "pipin Separate Absorption and Multiplication Ultraviolet Avalanche Photodiodes," *IEEE Photonics Technology Letters,* vol. 30, no. 2, pp. 181-184, 2017.

[39] D. Ji, B. Ercan, G. Benson, A. Newaz, and S. Chowdhury, "60 A/W high voltage GaN avalanche photodiode demonstrating robust avalanche and high gain up to 525 K," *Applied Physics Letters,* vol. 116, no. 21, p. 211102, 2020.

[40] T. Tut, S. Butun, B. Butun, M. Gokkavas, H. Yu, and E. Ozbay, "Solar-blind Al x Ga 1− x N-based avalanche photodiodes," *Applied Physics Letters,* vol. 87, no. 22, p. 223502, 2005.

[41] Z. Shao, X. Yang, H. You, D. Chen, H. Lu, R. Zhang, Y. Zheng, and K. Dong, "Ionization-enhanced AlGaN heterostructure avalanche photodiodes," *IEEE Electron Device Letters,* vol. 38, no. 4, pp. 485-488, 2017.

[42] Q. Cai, W. Luo, R. Yuan, H. You, Q. Li, M. Li, D. Chen, H. Lu, R. Zhang, and Y. Zheng, "Back-illuminated AlGaN heterostructure solar-blind avalanche photodiodes with one-dimensional photonic crystal filter," *Optics Express,* vol. 28, no. 5, pp. 6027-6035, 2020.

[43] L. Hahn, F. Fuchs, L. Kirste, R. Driad, F. Rutz, T. Passow, K. Köhler, R. Rehm, and O. Ambacher, "Avalanche multiplication in AlGaN-based heterostructures for the ultraviolet spectral range," *Applied Physics Letters,* vol. 112, no. 15, p. 151102, 2018.

[44] P. Reddy, M. Hayden Breckenridge, Q. Guo, A. Klump, D. Khachariya, S. Pavlidis, W. Mecouch, S. Mita, B. Moody, and J. Tweedie, "High gain, large area, and solar blind avalanche photodiodes based on Al-rich AlGaN grown on AlN substrates," *Applied Physics Letters,* vol. 116, no. 8, p. 081101, 2020.

[45] L. Gautam, A. G. Jaud, J. Lee, G. J. Brown, and M. Razeghi, "Geiger-mode operation of AlGaN avalanche photodiodes at 255 nm," *IEEE Journal of Quantum Electronics,* vol. 57, no. 2, pp. 1-6, 2021.

[46] M. Moram and M. Vickers, "X-ray diffraction of III-nitrides," *Reports on progress in physics,* vol. 72, no. 3, p. 036502, 2009.

[47] G. Bauer and W. Richter, *Optical characterization of epitaxial semiconductor layers*. Springer Science & Business Media, 2012.

[48] P. Makuła, M. Pacia, and W. Macyk, "How to correctly determine the band gap energy of modified semiconductor photocatalysts based on UV–Vis spectra," ed: ACS Publications, 2018.

[49] M. Ji, "Growth, fabrication, and characterization of III-nitride semiconductors for high-performance ultraviolet avalanche photodiodes by metalorganic chemical vapor deposition," Georgia Institute of Technology, 2018.

[50] Y. Zhang, D. Yoo, J. B. Limb, J. H. Ryou, R. D. Dupuis, and S. C. Shen, "GaN ultraviolet avalanche photodiodes fabricated on free-standing bulk GaN substrates," *physica status solidi c,* vol. 5, no. 6, pp. 2290-2292, 2008.

[51] Y. Zhang, "Development of III-nitride bipolar devices: avalanche photodiodes, laser diodes, and double-heterojunction bipolar transistors," Georgia Institute of Technology, 2011.

[52] R. McIntyre, "Multiplication noise in uniform avalanche diodes," *IEEE Transactions on Electron Devices,* no. 1, pp. 164-168, 1966.

[53] I. H. Oğuzman, E. Bellotti, K. F. Brennan, J. Kolník, R. Wang, and P. P. Ruden, "Theory of hole initiated impact ionization in bulk zincblende and wurtzite GaN," *Journal of Applied Physics,* vol. 81, no. 12, pp. 7827-7834, 1997.

[54] L. Cao, J. Wang, G. Harden, H. Ye, R. Stillwell, A. J. Hoffman, and P. Fay, "Experimental characterization of impact ionization coefficients for electrons and holes in GaN grown on bulk GaN substrates," *Applied Physics Letters,* vol. 112, no. 26, p. 262103, 2018.

[55] T. Maeda, T. Narita, S. Yamada, T. Kachi, T. Kimoto, M. Horita, and J. Suda, "Impact ionization coefficients and critical electric field in GaN," *Journal of Applied Physics,* vol. 129, no. 18, p. 185702, 2021.

[56] X.-H. Li, Y. O. Wei, S. Wang, H. Xie, T.-T. Kao, M. M. Satter, S.-C. Shen, P. D. Yoder, T. Detchprohm, and R. D. Dupuis, "Temperature dependence of the crystalline quality of AlN layer grown on sapphire substrates by metalorganic chemical vapor deposition," *Journal of Crystal Growth,* vol. 414, pp. 76-80, 2015.

[57] K. Uesugi, Y. Hayashi, K. Shojiki, and H. Miyake, "Reduction of threading dislocation density and suppression of cracking in sputter-deposited AlN templates annealed at high temperatures," *Applied Physics Express,* vol. 12, no. 6, p. 065501, 2019.

[58] L. Meng, W. Guohong, L. Hongjian, L. Zhicong, Y. Ran, W. Bing, L. Panpan, L. Jing, Y. Xiaoyan, and W. Junxi, "Low threading dislocation density in GaN films grown on patterned sapphire substrates," *Journal of Semiconductors,* vol. 33, no. 11, p. 113002, 2012.

[59] Z. Bryan, I. Bryan, J. Xie, S. Mita, Z. Sitar, and R. Collazo, "High internal quantum efficiency in AlGaN multiple quantum wells grown on bulk AlN substrates," *Applied Physics Letters,* vol. 106, no. 14, p. 142107, 2015.

[60] P. Lu, R. Collazo, R. Dalmau, G. Durkaya, N. Dietz, and Z. Sitar, "Different optical absorption edges in AlN bulk crystals grown in m-and c-orientations," *Applied Physics Letters,* vol. 93, no. 13, p. 131922, 2008.

[61] J. L. Hudgins, "Wide and narrow bandgap semiconductors for power electronics: A new valuation," *Journal of Electronic materials,* vol. 32, no. 6, pp. 471-477, 2003.

[62] A. Nishikawa, K. Kumakura, and T. Makimoto, "High critical electric field exceeding 8 MV/cm measured using an AlGaN p–i–n vertical conducting diode on n-SiC substrate," *Japanese journal of applied physics,* vol. 46, no. 4S, p. 2316, 2007.

[63] J. Muth, J. D. Brown, M. Johnson, Z. Yu, R. Kolbas, J. Cook, and J. Schetzina, "Absorption coefficient and refractive index of GaN, AlN and AlGaN alloys," *Materials Research Society Internet Journal of Nitride Semiconductor Research,* vol. 4, no. S1, pp. 502-507, 1999.

[64] I. Wegrzecka, M. Wegrzecki, M. Grynglas, J. Bar, A. Uszynski, R. Grodecki, P. Grabiec, S. Krzeminski, and T. Budzynski, "Design and properties of silicon avalanche photodiodes," *Opto-Electronics Review,* vol. 12, no. 1, pp. 95-104, 2004.

[65] P. C. Joshi, M. Moriguchi, M. A. Crowder, S. R. Droes, J. S. Flores, A. T. Voutsas, and J. W. Hartzell, "Low temperature processing of SiO2 thin films by HD-PECVD technique for gate dielectric applications," in *Poly-Silicon Thin Film Transistor Technology and Applications in Displays and Other Novel Technology Areas*, 2003, vol. 5004, pp. 105-112: International Society for Optics and Photonics.

[66] P. Reddy, S. Washiyama, F. Kaess, R. Kirste, S. Mita, R. Collazo, and Z. Sitar, "Point defect reduction in MOCVD (Al) GaN by chemical potential control and a comprehensive model of C incorporation in GaN," *Journal of Applied Physics,* vol. 122, no. 24, p. 245702, 2017.

[67] J. R. Creighton, G. T. Wang, W. G. Breiland, and M. E. Coltrin, "Nature of the parasitic chemistry during AlGaInN OMVPE," *Journal of crystal growth,* vol. 261, no. 2-3, pp. 204-213, 2004.

[68] G. Huang, H. Yao, H.-C. Kuo, and S. Wang, "Effect of growth conditions on the Al composition and quality of AlGaN film," *Materials Science and Engineering: B,* vol. 136, no. 1, pp. 29-32, 2007.

[69] L. Tang, B. Tang, H. Zhang, and Y. Yuan, "Review of Research on AlGaN MOCVD Growth," *ECS Journal of Solid State Science and Technology,* vol. 9, no. 2, p. 024009, 2020.

[70] A. Tanide, S. Nakamura, A. Horikoshi, S. Takatsuji, M. Kohno, K. Kinose, S. Nadahara, K. Ishikawa, M. Sekine, and M. Hori, "Effects of BCl3 addition to Cl2 gas on etching characteristics of GaN at high temperature," *Journal of Vacuum Science & Technology B, Nanotechnology and Microelectronics: Materials, Processing, Measurement, and Phenomena,* vol. 37, no. 2, p. 021209, 2019.

[71] E. A. Douglas, C. A. Sanchez, R. J. Kaplar, A. A. Allerman, and A. G. Baca, "Inductively coupled BCl3/Cl2/Ar plasma etching of Al-rich AlGaN," *Journal of Vacuum Science & Technology A: Vacuum, Surfaces, and Films,* vol. 35, no. 2, p. 021305, 2017.

[72] C. Eddy and B. Molnar, "Plasma etch-induced conduction changes in gallium nitride," *Journal of electronic materials,* vol. 28, no. 3, pp. 314-318, 1999.

[73] J. H. Wang, S. Mohney, S. Wang, U. Chowdhury, and R. Dupuis, "Vanadium-based ohmic contacts to n-type Al 0.6 Ga 0.4 N," *Journal of electronic materials,* vol. 33, no. 5, pp. 418-421, 2004.

[74] H.-D. Liu, X. Guo, D. McIntosh, and J. C. Campbell, "Demonstration of ultraviolet 6H-SiC PIN avalanche photodiodes," *IEEE Photonics Technology Letters,* vol. 18, no. 23, pp. 2508-2510, 2006.

[75] M. S. Tyagi, "Zener and avalanche breakdown in silicon alloyed pn junctions—I: Analysis of reverse characteristics," *Solid-State Electronics,* vol. 11, no. 1, pp. 99-115, 1968.

[76] M.-H. Ji, J. Kim, T. Detchprohm, R. D. Dupuis, A. K. Sood, N. K. Dhar, and J. Lewis, "Uniform and Reliable GaNp-in Ultraviolet Avalanche Photodiode Arrays," *IEEE Photonics Technology Letters,* vol. 28, no. 19, pp. 2015-2018, 2016.

[77] S. Cova, M. Ghioni, A. Lacaita, C. Samori, and F. Zappa, "Avalanche photodiodes and quenching circuits for single-photon detection," *Applied optics,* vol. 35, no. 12, pp. 1956-1976, 1996.

[78] J. G. Rarity, T. E. Wall, K. D. Ridley, P. C. Owens, and P. R. Tapster, "Single-photon counting for the 1300–1600-nm range by use of Peltier-cooled and passively quenched InGaAs avalanche photodiodes," *Applied Optics,* vol. 39, no. 36, pp. 6746-6753, 2000.

[79] R. G. Brown, K. D. Ridley, and J. G. Rarity, "Characterization of silicon avalanche photodiodes for photon correlation measurements. 1: Passive quenching," *Applied Optics,* vol. 25, no. 22, pp. 4122-4126, 1986.

[80] S. Cova, A. Longoni, and A. Andreoni, "Towards picosecond resolution with single-photon avalanche diodes," *Review of Scientific Instruments,* vol. 52, no. 3, pp. 408-412, 1981.

[81] R. G. Brown, R. Jones, J. G. Rarity, and K. D. Ridley, "Characterization of silicon avalanche photodiodes for photon correlation measurements. 2: Active quenching," *Applied Optics,* vol. 26, no. 12, pp. 2383-2389, 1987.

[82] S. Cova, A. Longoni, and G. Ripamonti, "Active-quenching and gating circuits for single-photon avalanche diodes (SPADs)," *IEEE Transactions on nuclear science,* vol. 29, no. 1, pp. 599-601, 1982.

[83] P. Antognetti, S. Cova, and A. Longoni, "A study of the operation and performances of an avalanche diode as a single-photon detector," *Proceedings 2nd Ispra nuclear electronics symposium*, EUR-5370, 1975.

[84] A. Lacaita, S. Cova, C. Samori, and M. Ghioni, "Performance optimization of active quenching circuits for picosecond timing with single photon avalanche diodes," *Review of scientific instruments,* vol. 66, no. 8, pp. 4289-4295, 1995.

[85] D. Bonaccini, S. D. Cova, M. Ghioni, R. Gheser, S. Esposito, and G. Brusa-Zappellini, "Novel avalanche photodiode for adaptive optics," in *Adaptive Optics in Astronomy*, 1994, vol. 2201, pp. 650-657: International Society for Optics and Photonics.

[86] H. Dautet, P. Deschamps, B. Dion, A. D. MacGregor, D. MacSween, R. J. McIntyre, C. Trottier, and P. P. Webb, "Photon counting techniques with silicon avalanche photodiodes," *Applied optics,* vol. 32, no. 21, pp. 3894-3900, 1993.

[87] A. Lightstone and R. McIntyre, "Photon counting silicon avalanche photodiodes for photon correlation spectroscopy," *Photon Correlation Techniques and Applications,* vol. 1, pp. 183-191, 1988.

[88] B. Levine and C. Bethea, "Single photon detection at 1.3 μm using a gated avalanche photodiode," *Applied Physics Letters,* vol. 44, no. 5, pp. 553-555, 1984.

[89] G. Ribordy, J.-D. Gautier, H. Zbinden, and N. Gisin, "Performance of InGaAs/InP avalanche photodiodes as gated-mode photon counters," *Applied Optics,* vol. 37, no. 12, pp. 2272-2277, 1998.

[90] G. F. Knoll, *Radiation detection and measurement*. John Wiley & Sons, 2010.

[91] G. Simons and N. Johnson, "On the convergence of binomial to Poisson distributions," *The Annals of Mathematical Statistics,* vol. 42, no. 5, pp. 1735-1736, 1971.

[92] C. Piemonte, A. Ferri, A. Gola, A. Picciotto, T. Pro, N. Serra, A. Tarolli, and N. Zorzi, "Development of an automatic procedure for the characterization of silicon photomultipliers," in *2012 IEEE Nuclear Science Symposium and Medical Imaging Conference Record (NSS/MIC)*, 2012, pp. 428-432: IEEE.

[93] B. Razavi, *Fundamentals of microelectronics*. John Wiley & Sons, 2021.

[94] A. V. Oppenheim, A. S. Willsky, S. H. Nawab, and G. M. Hernández, *Signals & systems*. Pearson Educación, 1997.

[95] W. J. Kindt, "Geiger mode avalanche photodiode arrays: For spatially resolved single photon counting," *Ph. D. Thesis,* p. 471, 1999.

[96] G. Hurkx, "On the modelling of tunnelling currents in reverse-biased pn junctions," *Solid-State Electronics,* vol. 32, no. 8, pp. 665-668, 1989.

[97] S. Maimon and G. Wicks, "n B n detector, an infrared detector with reduced dark current and higher operating temperature," *Applied Physics Letters,* vol. 89, no. 15, p. 151109, 2006.

[98] M. Cho, Z. Xu, M. Bakhtiary-Noodeh, H. Jeong, C.-W. Tsou, T. Detchprohm, R. D. Dupuis, and S.-C. Shen, "Effective Leakage Current Reduction in GaN Ultraviolet Avalanche Photodiodes With an Ion-Implantation Isolation Method," *IEEE Transactions on Electron Devices,* vol. 68, no. 6, pp. 2759-2763, 2021.

[99] A. Vilà, J. Trenado, A. Arbat, A. Comerma, D. Gascon, L. Garrido, and A. Dieguez, "Characterization and simulation of avalanche photodiodes for next-generation colliders," *Sensors and Actuators A: Physical,* vol. 172, no. 1, pp. 181-188, 2011.

[100] J. Frenkel, "On pre-breakdown phenomena in insulators and electronic semi-conductors," *Physical Review,* vol. 54, no. 8, p. 647, 1938.

[101] M. Born and E. Wolf, *Principles of optics: electromagnetic theory of propagation, interference and diffraction of light*. Elsevier, 2013.

[102] A. N. Otte, T. Nguyen, and J. Stansbury, "Locating the avalanche structure and the origin of breakdown generating charge carriers in silicon photomultipliers by using the bias dependent breakdown probability," *Nuclear Instruments and Methods in Physics Research Section A: Accelerators, Spectrometers, Detectors and Associated Equipment,* vol. 916, pp. 283-289, 2019.